CZECH TECHNICAL UNIVERSITY IN PRAGUE

Faculty of Nuclear Sciences and Physical Engineering

DISSERTATION

Development of a Scintillation Spectrometer of Photons in Laser-Generated Pulsed-Radiation Fields

Prague 2024 Vojtěch Stránský

Bibliografický záznam

Autor:	Ing. Vojtěch Stránský České vysoké učení technické v Praze, Fakulta jaderná a fyzikálně inženýrská, Katedra dozimetrie a aplikace ionizujícího záření
Název práce:	Vývoj scintilačního spektrometru fotonů pro laserem generovaná pulzní radiační pole
Studijní program:	Aplikace přírodních věd
Studijní obor:	Jaderné inženýrství
Školitel:	prof. Ing. Tomáš Trojek, Ph.D. České vysoké učení technické v Praze, Fakulta jaderná a fyzikálně inženýrská, Katedra dozimetrie a aplikace ionizujícího záření
Školitel specialista:	Roberto Versaci, Ph.D. The Extreme Light Infrastructure ERIC, ELI Beamlines Facility
Akademický rok:	2023/2024
Počet stran:	94
Klíčová slova:	laserem generované záření, pulzní záření, spektrometrie fotonů, scintilační spektrometr, ELI Beamlines

Bibliographic entry

Author:	Ing. Vojtěch Stránský Czech Technical University in Prague, Faculty of Nuclear Sciences and Physical Engineering, Department of Dosimetry and Application of Ionizing Radiation
Title of Dissertation:	Development of a Scintillation Spectrometer of Photons in Laser-Generated Pulsed-Radiation Fields
Degree Programme:	Application of Natural Sciences
Field of Study:	Nuclear Engineering
Supervisor:	prof. Ing. Tomáš Trojek, Ph.D. Czech Technical University in Prague, Faculty of Nuclear Sciences and Physical Engineering, Department of Dosimetry and Application of Ionizing Radiation
Supervisor specialist:	Roberto Versaci, Ph.D. The Extreme Light Infrastructure ERIC, ELI Beamlines Facility
Academic Year:	2023/2024
Number of Pages:	94
Keywords:	laser-generated radiation, pulsed radiation. photon spectrometry, scintillation spectrometer, ELI Beamlines

Abstrakt

Laserem generované fotonové záření představuje díky svým unikátním vlastnostem slibný nástroj pro mnoho oborů. Nicméně spektrometrie takového záření je náročná, neboť takové záření je vytvářeno v pulzech. Vzhledem k tomu, že běžné metody fotonové spektrometrie nejsou pro tento typ záření vhodné, je nezbytné vyvinout nový detektor. Tato disertační práce popisuje návrh takového spektrometru fotonů v laserem generovaných polích pulzního záření. Součástí práce je kalibrace a validace tohoto spektrometru pomocí konvenčních zdrojů a také experimentální výsledky získané na zařízení ELIMAIA v ELI Beamlines. Z výsledků je patrné, že vyvinutý detektor je vhodný pro fotonovou spektrometrii v pulzních polích záření.

Abstract

Laser-generated photonic radiation represents a promising tool in numerous scientific fields, because of its unique properties. However, spectrometry of such radiation is challenging due to its pulsed nature. As common methods for photon spectrometry cannot be used, there is a need for a novel detector. This dissertation describes the design of such spectrometer of photons in laser-generated pulsed-radiation fields. Moreover, calibration and validation of this spectrometer using conventional sources is presented as well as experimental results from experiment at ELI Beamlines ELIMAIA beamline. The results prove that the developed detector can be used for photon spectrometry in pulsed-radiation fields.

Acknowledgement

I would like to thank the following people who made this dissertation possible:

- My supervisor prof. Tomáš Trojek, Ph.D. for his dedicated support and guidance;
- My supervisor specialist Roberto Versaci, Ph.D. for valuable advice and support throughout the spectrometer development;
- The Safety manager of ELI Beamlines Ing. Veronika Olšovcová Ph.D. for her support and encouragement with writing this thesis;
- My coworker Ing. Valeria Istokskaia, Ph.D. for all the time spent together on this project and all the invaluable contributions to the development of the spectrometer;
- Other team members for all their valuable work – Daniele Margarone Ph.D., Lorenzo Giuffrida Ph.D., Anna Cimmino Ph.D. and Benoit Lefebvre Ph.D.;
- My parents, I simply couldn't have done this without you;
- And finally, my wife Anna Magdaléna and my daughters Eleonora and Elvíra for providing all the necessary energy.

Vojtěch Stránský

Contents

Introduction

Recent developments in femtosecond laser technology have enabled the production of ultra-short ionising radiation pulses through laser interaction with matter [1, 2]. Depending on the laser pulse properties and the target material characteristics, such interaction can lead to generation of X-rays and γ-rays (and other particles) in a form of ultrashort pulses, that find applications in numerous scientific fields [3]. Additionally, the laser-driven sources can be deemed point-like, given the small (few μm) focal spot on the target. As of the time of writing this thesis, no conventional ionising radiation source has been able to produce ultra-short X-ray pulses with comparable properties [4].

These unique characteristics of laser-generated X-ray and γ radiation make it a promising tool in various applications. In research, it can be used to investigate the properties of materials in very short time scales [5]. The ultra-short duration of the pulses allows for the observation of ultra-fast phenomena, such as the dynamics of chemical reactions [6]. Laser-generated radiation can also be employed for high-resolution imaging, potentially even in medicine.

Because of these possible applications and since the generated photonic radiation can provide insights into laser-matter interactions, it is essential to characterise the generated radiation on a shot-by-shot basis. However, this task is challenging, as standard methods for X-ray spectrometry, that rely on single-photon counting, prove to be extremely difficult or even impossible to be applied in high-flux pulsed radiation fields [7].

Several diagnostics for pulsed photonic radiation are available, however, these are generally limited to integral dosimetric quantities (e.g. ambient dose equivalent). Only a few of these diagnostics are able to provide spectral information. These diagnostics typically exploit passive detectors, such as radiochromic films [8]. However, in high-repetition rate environments, these methods provide only an average spectral information, not a characterisation of each shot. Furthermore, the preparation and readout of these systems require a substantial effort and can be time-consuming.

In order to be able to obtain real-time spectral information for each individual shot, an active detector is required. The active system described in this thesis exploits the principle of a segmented electromagnetic calorimeter used in the field of high energy physics [9]. A segmented calorimeter is a set of stacked scintillating layers, enabling measurement of the energy deposited at different depths in the material. In the context of high-energy physics, electromagnetic calorimeters are used to determine the energy of a high-energy particle, in pulsed fields, it can be used to characterise the spectrum.

The spectrometer of high-energy high-flux photonic pulses was designed and fine-tuned using the FLUKA Monte Carlo code [10, 11]. The spectrometer comprises scintillator prisms of different sizes, a holder, an optical readout system, and an unfolding software. Using simulated response matrices, the detector is able to determine components of the impinging radiation, allowing to reconstruct the spectrum of impinging radiation. The spectrometer was tested in several radiation environments, calibrated and its function was validated.

The spectrometer was developed in collaboration between the Safety team (Radiation Protection and Monte Carlo group) and the ELIMAIA team of the Extreme Light Infrastructure, European Research Infrastructure Consortium (ELI ERIC) [12, 13], mainly to be applied at the ELI Beamlines facility. The author of this thesis has developed the principle of function of the spectrometer, significantly contributed to both the hardware and software design of the spectrometer, as well as to its calibration and validation using conventional sources of ionising radiation. The author had minor contributions to the experiments in laser-generated ionising radiation environments. Results of the design, calibration, validation, and other experiments have been published in multiple articles [14, 15, 16, 17]. The spectrometer was patented [18], the author of this thesis is listed as the first inventor.

Chapter 1

Extreme Light Infrastructure

The spectrometer developed in the frame of this thesis was designed to be used mainly within the experimental areas of the Extreme Light Infrastructure, European Research Infrastructure Consortium (ELI ERIC), namely the ELI Beamlines facility [19]. Thus, in order to describe the design considerations of the spectrometer, it is first necessary to describe in detail the environment, in which the spectrometer would be deployed and the context of the whole project.

ELI represents the world's most advanced civilian high-power laser infrastructure, focusing on application of high-power, high-intensity, and ultra-short pulsed laser systems. One of the application of these laser systems is generation of ultra-short pulses of high-energy ionising radiation.

In order to produce high-energy ionising radiation using a laser pulse, it is necessary to achieve ultra-high laser intensities on a target material. Given that, a large-scale laser system is needed. Operation of such large-scale cutting edge laser systems requires a dedicated facility with extensive auxiliary systems, such as vacuum distribution, vibration suppression and cleanrooms. The ELI Beamlines facility, located in Dolní Břežany, Czech Republic, houses all the required technologies.

1.1 ELI Beamlines

ELI Beamlines is one of the facilities that form The Extreme Light Infrastructure. This particular facility is dedicated to producing pulsed ionising radiation beams for user applications [20]. The layout of ELI Beamlines is shown in Fig. 1.1. The Laser Building of ELI Beamlines hosts four large-scale laser systems on its ground floor, each laser system being installed in a separate laser hall. Auxiliary systems, such as power supply and cooling, are installed in the halls of the first floor. The laser beams are transported into the experimental halls located below the ground level using a beam transport system, that allows directing individual laser beams into six experimental halls. Both the laser halls and the experimental halls are equipped with vibration suppression systems and clean rooms, minimising disruption of the laser beams. Also, given the need of transporting the high energy laser pulses in vacuum a central vacuum system is used to ensure the vacuum quality within the laser beam transport system [12].

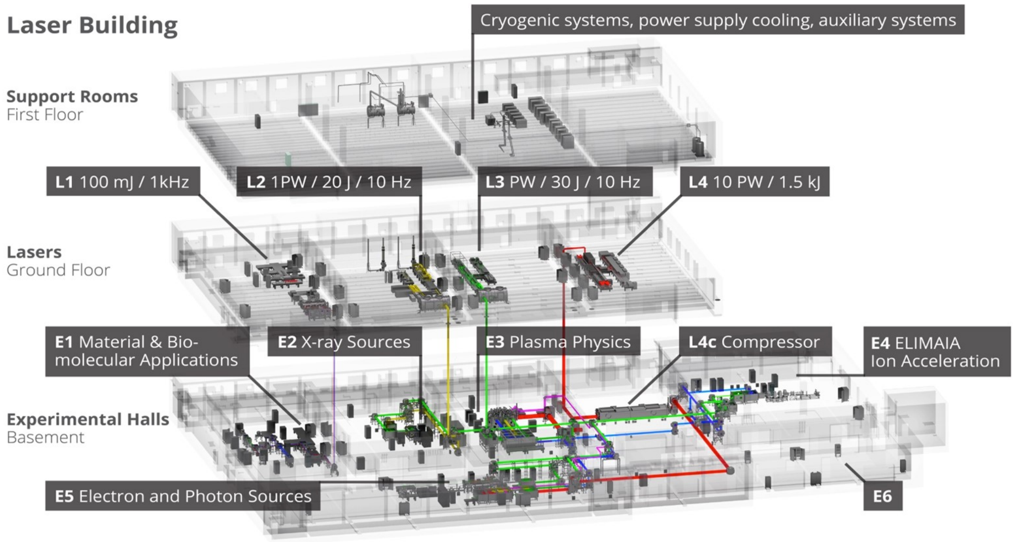

Fig. 1.1: Overview of the ELI Beamlines facility. Large scale laser systems, beam distribution and individual beamlines are highlighted. [21]

1.2 Laser systems

In addition to many small-scale lasers, ELI Beamlines hosts four large-scale systems that facilitate the operation of individual beamlines. Each of these laser systems provides different parameters, allowing variable laser beam parameters at the experimental stations. [22]

These laser systems rely on the technology of optical parametric chirped pulsed amplification (OPCPA) [23] that allows pulse compression so intense, that the peak laser pulse power can reach extremely high values, that would be impossible to achieve using continuous lasers. Such unprecedented laser pulse peak power enables reaching extremely high laser intensities at the target material. The parameters of individual laser systems are described in the following sections.

1.2.1 L1 Allegra

The L1 Allegra laser system has been developed internally by an ELI Beamlines team [24]. The goal of this laser is to deliver ultra-short laser pulses (20 fs) with a high frequency of 1 kHz. This laser system exploits seven precisely synchronised Yb:YAG amplifiers placed within the three main components: the front end, the booster, and the main amplifier. The beam of the L1 Allegra laser system is transported into the E1 Experimental hall located directly below the L1 laser hall where the Allegra is installed. Unlike other laser systems, the L1 laser systems was designed to be directed only into one experimental hall, the E1 [25].

1.2.2 L2 Duha

The L2 Duha laser system was designed to provide high-intensity laser pulses of 100 TW at high repetition rate (50 Hz) for experiments, that do not require the peak power in the PW range [26]. Another feature of this laser system is that it is capable of providing a wide range of wavelengths, hence the name Duha (rainbow). Unlike the L1 laser system, the L2 can be directed into multiple experimental halls [27].

1.2.3 L3 HAPLS

The L3 HAPLS laser system was designed to reach the PW level of laser pulse power, moreover, unlike similar PW-class laser systems that are able to deliver only tens of shots per day, it can operate at a high repetition rate of 10 Hz. This laser system was designed and built in collaboration between ELI Beamlines and the Lawrence Livermore National Laboratory. The system exploits Nd-doped glass amplifiers, that are pumped using high power diode arrays [28]. The L3 laser beam can be directed into any of the experimental halls with the exception of E1.

1.2.4 L4 Aton

The L4 Aton laser system is the most powerful laser system installed at ELI Beamlines, reaching unprecedented peak laser pulse power of 10 PW [22]. It exploits a chain of amplifiers based on different principles (including OPCPA) and various compressors for each of the operation regime. In the 10 PW operation regime, the full chain is used and a dedicated large-scale compressor placed in a separate hall in the basement level (L4c). Once compressed, the laser beam can be diverted into E3, E4, or E5 experimental halls.

1.2.5 Summary of laser systems

In summary, ELI Beamlines houses four main laser systems, each having different parameters in order to enable experiments with different requirements. Characteristics of pulses of individual laser systems at target are summarised in Tab. 1.1. Using these laser systems, it is possible to achieve extreme laser pulse intensities on targets up to the level of 10^{24} W/cm^2. Interaction of such laser pulses with matter enables production of ionising radiation within individual beamlines, that are described in the following section.

Laser system	L1 Allegra	L2 Duha	L3 HAPLS	L4 Aton
Pulse energy [J]	0.1	2	30	2000
Pulse duration [fs]	20	25	30	130
Repetition rate [Hz]	1000	50	10	0.02

Tab. 1.1: Overview of ELI Beamlines laser system's beam parameters at target.

1.3 Beamlines

Individual beamlines and experimental stations are placed at the basement level of ELI Beamlines. As each beamline serves a different purpose, each is designed and configured to achieve required beam properties [12]. While some of the beamlines are exploited for generating ionising radiation, ionising radiation is present at all beamlines, as all the beamlines rely on the laser-plasma interaction, during which the ionising radiation is produced inherently. Naturally, beamlines that produce beams of high-energy radiation also produce secondary radiation while interacting with other materials present inside the experimental halls. In the following sections the beamlines producing ionising radiation (> 5 keV) are described.

1.3.1 Plasma X-ray Sources

A set of plasma X-ray sources placed inside the E1 experimental hall exploit both the L1 Allegra laser system and small-scale lasers to produce pulsed X-ray beams of tens of keV at 1 kHz frequency. These lasers are focused on solid or liquid targets of different materials (metals, e.g. copper as seen in Fig. 1.2, or water [29]) in order to produce a spectrum that is desired for a particular experiment. Given the relatively low laser intensity, the produced X-ray radiation is mostly the characteristic radiation of target materials [30]. Using different materials, it is possible to achieve for example 8 keV when using Cu target or 77 keV when using Bi target. The length of X-ray pulse typically reaches hundreds of femtoseconds, enabling high-resolution X-ray imaging that is essential for material research [31].

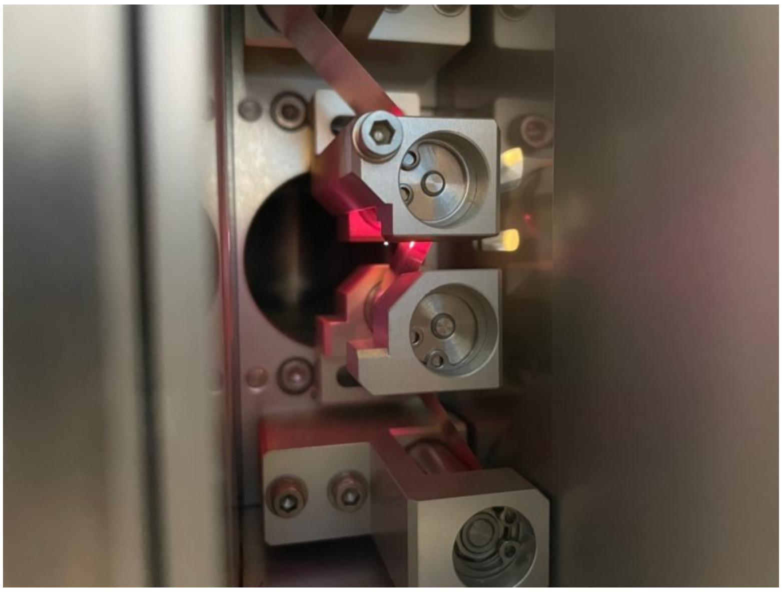

Fig. 1.2: Example of a PXS target station, in this case the laser beam is focused on the copper tape. [19]

1.3.2 Betatron/Compton

The Betatron/Compton beamline is located inside the E2 experimental hall. This beamline is dedicated to high energy X-ray generation, exploiting the PW class L3 laser system. A laser pulse with a gas target, producing high-energy electrons (up to 2 GeV). These electrons are accelerated by plasma wakefield and then wiggled, resulting in a production of betatron radiation (see Fig. 1.3) in the energy range of 1 keV – 100 keV. There is also an option to switch to other operational regime of the beamline, during which a second laser is focused onto the electron beam (see Fig. 1.4). This allows production of high energy X-rays exploiting the inverse Compton scattering. The energy range of X-ray radiation produced in this regime is estimated at 100 keV – 5 MeV [32].

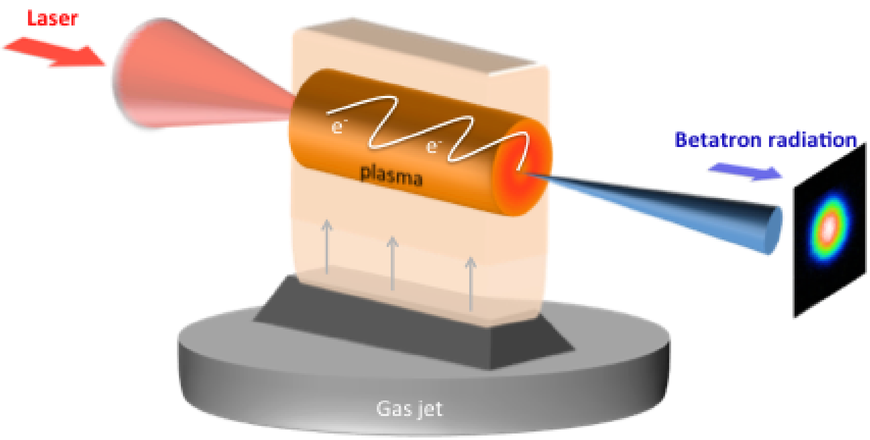

Fig. 1.3: Betatron/Compton beamline in the Betatron configuration. [19]

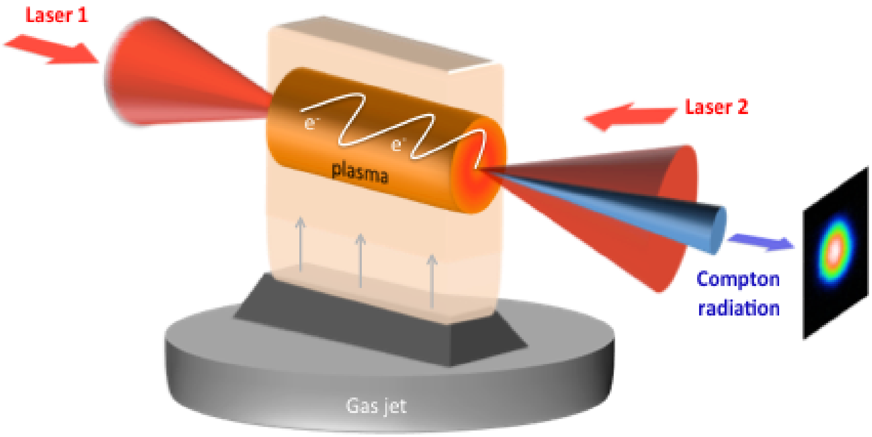

Fig. 1.4: Betatron/Compton beamline in the Compton configuration. Notice the second laser beam used to produce an electron beam. [19]

1.3.3 Plasma Physics Platform

The Plasma Physics Platform, located within the E3 experimental hall, is a beamline not primarily dedicated to ionising radiation production, but to research of the laser-plasma interaction and high energy density and plasma physics. It allows for simultaneous use of multiple synchronised lasers systems (including the most powerful L4 Aton laser system [33]) and thus creating extreme conditions on the target.

This platform can be also set up into two modes, that are dedicated for generating ionising radiation. The short-focal length setup that is used for generating X-ray and ion radiation, and the long-focal length setup, that is used for electron acceleration. The expected energy range of generated X-ray is in the units of keV to units of MeV region, while the electrons can be accelerated up to 1.5 GeV.

The main component of the Plasma Physics Platform is the experimental vacuum chamber, one of the largest vacuum chambers constructed for civilian research purposes. This vacuum chamber is approximately 3.5 meters high, with a radius of approximately 2.5 meters [19]. The internal volume of the chamber can be seen in Fig. 1.5. Similarly as in other beamlines, the target is placed within the vacuum chamber to allow the laser beam propagation to the target.

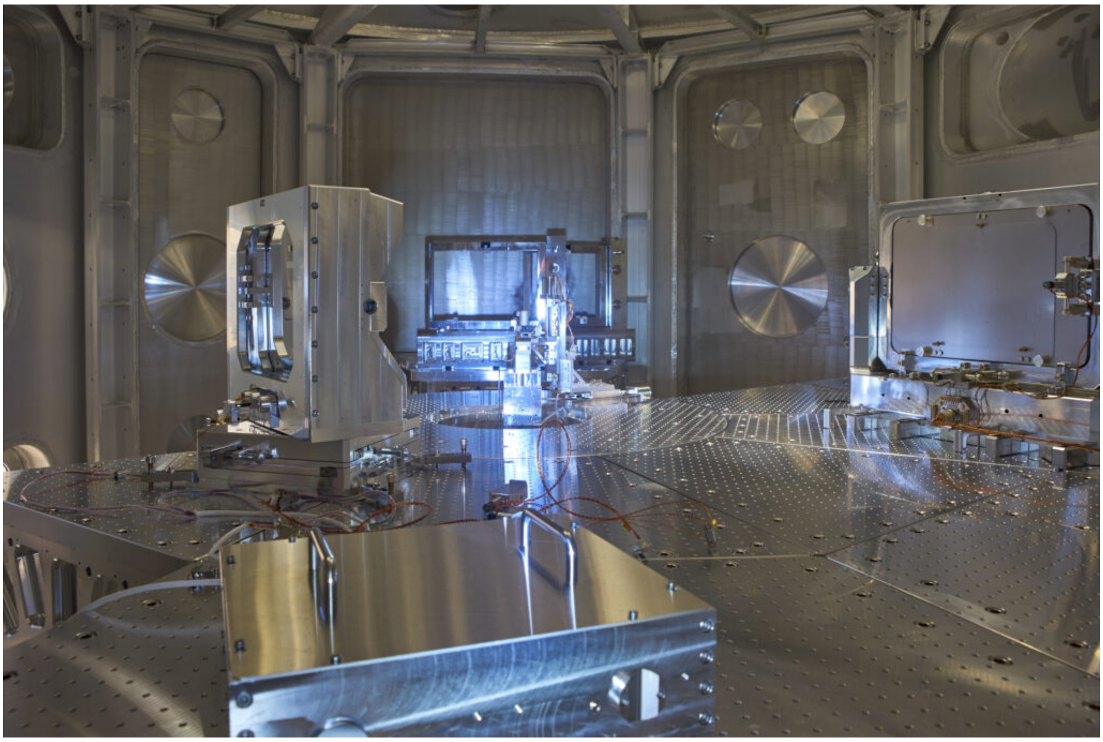

Fig. 1.5: The experimental setup inside the P3 vacuum chamber. [19]

1.3.4 ELIMAIA

The ELIMAIA beamline, located in the E4 experimental hall (see Fig. 1.6), is primarily used to produce ion beams by means of the L3 and L4 laser systems. It consists of a chain of experimental chambers where the beam is created, followed by an electromagnetic chicane that allows selection of desired beam energy and finally the beam is focused at the dosimetric station to allow various user experiments. [34]

The ions are accelerated thanks to the Target Normal Sheath Acceleration mechanism (TNSA) [35]. The electrons inside the target material are accelerated using the laser-plasma interaction, creating a strong electric field that accelerates ions of the target material. Given the nature of this mechanism, these ions are not monoenergetic, and thus the electromagnetic chicane is needed to select a desired part of the spectrum, other ions are absorbed within the electromagnetic chicane walls.

Ions transported to the dosimetric station can be used for various research, e.g. laser-driven hadrotherapy, fusion research, laser-triggered nuclear reactions, non-destructive testing (activation analysis) and others. The maximum energy of generated ions is expected to be in the range of hundreds of MeV/u [12].

Fig. 1.6: The ELIMAIA beamline within the E4 experimental hall of ELI Beamlines. [36]

1.3.5 LUIS

Similarly as the Betatron/Compton, the Laser Undulator Illuminating Source (LUIS), placed inside the E5 experimental hall, exploits the electron acceleration in order to produce pulsed X-ray radiation. Electrons in this beamline are accelerated by laser-plasma interaction in a gas target, allowing them to reach energies up to units of GeV. In case of LUIS, the X-ray generation is performed by means of undulation. It is envisioned that in future this beamline would be upgraded to a laser-driven free electron laser with intensity up to 10^{29} photons per shot [37].

1.3.6 ELBA

The E5 experimental hall houses also another beamline, the ELBA. This beamline serves as a laser-driven electron accelerator, exploiting the L3 HAPLS and L4 Aton laser systems. The laser pulses are focused on a gas target, accelerating electrons by means of Laser Wake Field Acceleration (LWFA) to energies up to tens of GeV. [38] The beamline is dedicated to optimising the electron acceleration technology not only for user research, achieving high beam stability at high electron energy and at high repetition rate [39]. Both LUIS and ELBA beamlines are seen in Fig. 1.7.

Fig. 1.7: The E5 experimental hall with LUIS beamline (left) and ELBA beamline (right). Notice the large number of technologies present within the experimental hall. [19]

1.3.7 TERESA

The TERESA target area was built in the L2 laser hall mainly for testing and development of target delivery systems and laser-plasma diagnostics [40], until the other beamlines would be commissioned. Within the TERESA target area, it is possible to produce ion and electron radiation as well as X-ray pulsed radiation. Ionising radiation pulses are produced at the frequency of 10 Hz, since TERESA uses the L3 laser system. TERESA consists of four interconnected vacuum chambers, as seen in Fig. 1.8.

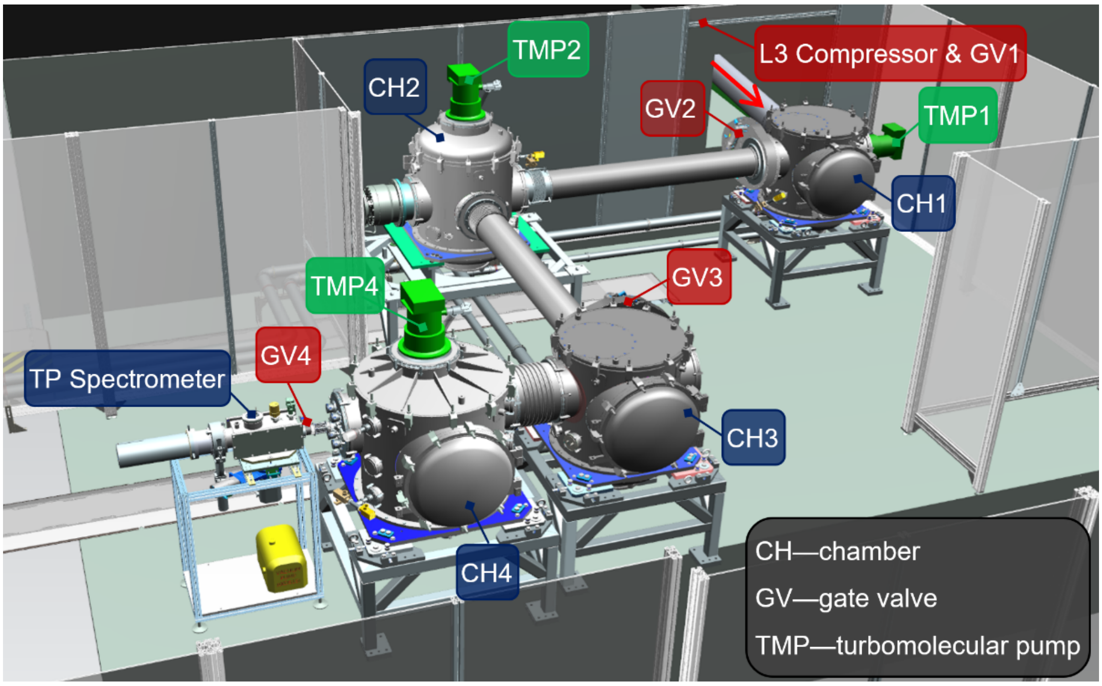

Fig. 1.8: Drawing of the TERESA target area within the L2 laser hall. Notice the L3 HAPLS laser beam coming from the neighbouring L3 laser hall. [40]

While TERESA does not represent a large-scale beamline for user research, this target area was available in the early stages of the spectrometer development, allowing to test various components in the environment of a laser research facility and to expose them to low-intensity laser-generated radiation. More information on implications of this environment for the spectrometer design are outlined in the next section.

1.4 Considerations for spectrometer design

While each beamline is dedicated for specific scientific needs and production of different ionising radiation beams, X-ray radiation is created at all mentioned beamlines, either intentionally or as a side effect. X-ray radiation is generated both within the laser-generated plasma and as a result of electromagnetic cascades caused by interactions of the primary beam with other materials present in the halls (e.g optics within the vacuum chambers, beamline components, shielding materials, and other technologies).

The X-rays generated during the laser-plasma interaction are essential to be characterised, as they provide insight into the laser-plasma interaction itself, allowing monitoring of the laser-plasma interaction. Moreover, as at some of the beamlines the generated X-rays are used directly for user research, it is needed to monitor quality of the X-ray beam. Therefore, spectrometry of X-rays is beneficial for all the above-mentioned beamlines at ELI Beamlines.

However, given the pulsed nature of generated X-ray radiation, no commercially available detector is able to perform spectrometry of individual X-ray pulses. Therefore, a collaboration was set between the ELI Beamlines Safety and ELIMAIA teams to develop and test a novel spectrometer of pulsed X-ray radiation. The Safety Team having experts on radiation protection provided expertise on X-ray detectors, conventional X-ray sources, and Monte Carlo simulations. The ELIMAIA team provided expertise on laser-plasma interaction, generation of X-ray radiation using laser pulses, and the TERESA and ELIMAIA beamlines for testing.

The properties of laser-generated X-ray radiation and their implications on the spectrometer design are described in detail in the following chapter.

Chapter 2

Laser-generated X-ray radiation

Laser-generated X-ray and γ radiation has gained significant attention in various scientific, medical, and industrial fields due to its pulsed nature. The production of such radiation is performed by focusing a femtosecond laser pulse on a suitable target, leading to the creation of highly intense and ultra-short (few femtosecond [41]) photonic pulses. The details of the processes leading to generating photonic ionising radiation are discussed in this chapter.

As already stated, a significant objective of research in the field of laser-generated X-ray radiation is to characterise individual X-ray pulses, specifically, to measure their spectrum. However, spectrometry of pulsed X-ray radiation presents greater challenges than that of continuous X-ray beams. As of today, experimental results of spectra are scarce, and in some cases, only simulation results are available. These results together with possible methods of pulsed X-ray spectrometry are also discussed in this chapter.

2.1 X-ray production by laser pulses

Laser-generated X-ray radiation originates from the motion of free electrons that are generated inside the plasma created during the interaction of the laser pulse with the target material. These electrons can produce X-rays through several mechanisms, including characteristic radiation, bremsstrahlung, and inverse Compton scattering [42]. To gain a comprehensive understanding of the characteristics of laser-generated X-ray radiation, it is necessary to investigate the various ionisation and acceleration processes induced by the laser pulse.

An ultra-short laser pulse can be treated as an electromagnetic wave. In order to characterise the effects of interaction of this wave with a target material, it is useful to consider the **laser intensity**, denoted by I and typically measured in units of $\mathrm{W/cm^2}$ [43]. The behaviour of the laser exhibits significant variations at distinct intensity levels, rendering intensity one of the pivotal parameter in ascertaining the outcome of the laser-target interaction [3]. Following sections provide brief insight into the interactions between the laser pulse and the target material at different laser intensity levels.

2.1.1 Ionisation and electron acceleration by laser pulses

The processes that precede generation of photonic ionising radiation during laser-target interaction are the ionisation and subsequent acceleration of electrons of the target material. The individual processes of ionisation and acceleration are described in the following sections.

Multiphoton and Field Ionisation

At the laser intensity level of approximately 10^{10} W/cm^2, it becomes energetically possible for outer-shell electron to become free by a simultaneous absorption of multiple photons of the laser pulse. This phenomenon is referred to as **multiphoton ionisation**. With increasing laser intensity, the electric field of the laser pulse becomes stronger, enabling distortion of the atomic Coulomb barrier. This allows electrons to become free by means of quantum tunnelling.

As the laser intensity increases even more, the Coulomb barrier deformation becomes so pronounced, that electrons are directly freed and accelerated by the electric field of the laser pulse (see Fig. 2.1). This process is known as the **field ionisation**. As the laser intensity increases, this process becomes capable of freeing electrons from even the innermost atomic shells. Field ionisation becomes the dominant process at intensities of approximately 10^{14} W/cm^2. [44]

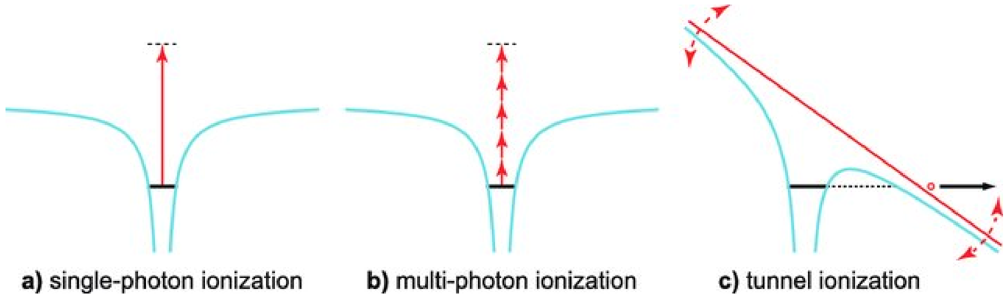

Fig. 2.1: Comparison of ionisation processes: a) single-photon ionisation, b) multiphoton ionisation, and c) field ionisation. [44]

Collisional Heating

As the laser intensity increases to $10^{14} - 10^{17}$ W/cm^2, the energy of free electrons becomes high enough to induce further ionisation within the target material, leading to a significant increase in the number of free electrons. The density of free electrons and ions becomes so high that a collective behaviour of plasma must be considered. This process is generally referred to as **collisional heating** or inverse bremsstrahlung (as it involves energy transfer from photons to electrons) [45].

Collective absorption

Once the laser intensity surpasses the threshold of 10^{17} W/cm^2, the collective absorption processes become evident. Plasma oscillations are created by electric forces, whose frequency ω_p can be calculated as

$$\omega_P = \sqrt{n_e \cdot e/\varepsilon_0 \cdot m_e} = 5.7 \cdot 10^4 \sqrt{n_e(\mathrm{cm}^{-3})}\,\mathrm{Hz}, \qquad (2.1)$$

where n_e is the plasma density, e the electron charge, ε_0 the vacuum permittivity and m_e the electron mass. The frequency ω_p is therefore dependant only on the plasma density. A laser-generated plasma is not uniform, the highest density is located in the centre of the plasma and decreases exponentially with increasing distance from the centre. Therefore, it is possible to find a wide range of ω_P inside a laser-generated plasma. This also means that at some locations inside the plasma, the plasma frequency ω_P is equal to the one of the laser pulse ω_L, allowing a resonant transmission of energy [3].

This resonance enables generation of so-called superheated (or hot) electrons, having temperature much higher than the one of the plasma. This phenomenon, called **collective resonance absorption** or resonance heating, thus leads to a bi-Maxwellian electron spectrum (low temperature from collisional heating, high-temperature from collective absorption), as seen in Fig. 2.2 [46].

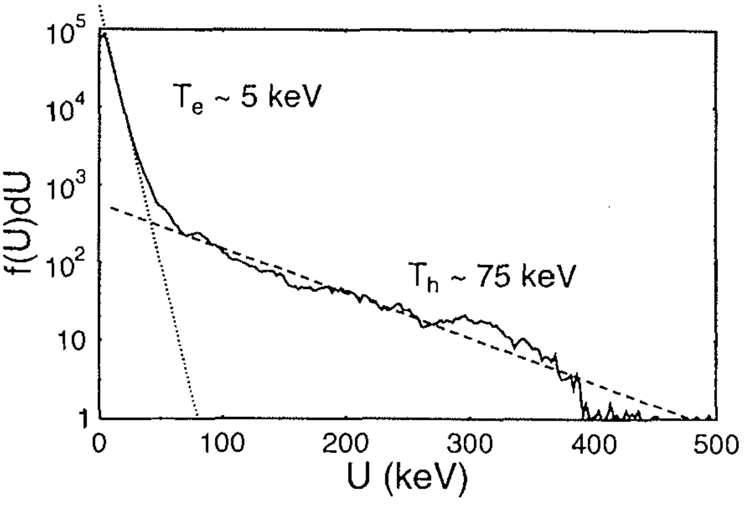

Fig. 2.2: A typical electron spectrum with two Maxwellian components, U is the electron energy, $f(U)\mathrm{d}u$ represent the relative number of electrons. T_e is the temperature of "cold" electrons, T_h is the temperature of "hot" electrons. Result of a PIC simulation, laser intensity $I = 5 \cdot 10^{16}$ W/cm^2 [46].

Relativistic acceleration

At the laser intensity of approximately $3 \cdot 10^{18}\,\mathrm{W/cm^2}$ the magnetic component of the Lorentz force becomes significant, as it causes electrons to accelerate in the direction of the laser pulse, thus generating a population of hot electrons [3]. Energy of such electrons follows a Maxwellian distribution, the temperature can be estimated using scaling laws, such as

$$T \approx m_e c^2 \left[\left(1 + \frac{I \cdot \lambda^2}{1.37 \cdot 10^{18}\,\mathrm{W} \cdot \mathrm{cm}^{-2} \cdot \mu\mathrm{m}^2} \right)^{1/2} - 1 \right], \tag{2.2}$$

where m_e is the electron mass, I the laser pulse intensity and λ the laser pulse wavelength [46]. It should be noted that other scaling laws exist and can be used depending on the experimental conditions [47, 48].

2.1.2 Characteristic radiation and bremsstrahlung

The free electrons generated by aforementioned processes generate X-ray radiation through mechanisms similar to those exploited in conventional sources of ionising radiation, such as X-ray tubes or linear accelerators. At low laser intensities, the dominant process is the **characteristic radiation** emission produced during electron recombination or relaxation. This process results in a production of low energy X-rays with discrete energies [49].

With increasing laser intensity, **bremsstrahlung** production becomes the dominant mechanism. The accelerated electrons emit bremsstrahlung as they undergo momentum changes during interactions with the plasma, the target material (particularly high-Z materials), and other materials in proximity. In contrast to characteristic radiation, bremsstrahlung spectrum exhibits a continuous distribution, following a Maxwellian shape [49]. An overview of these processes is shown in Fig. 2.3.

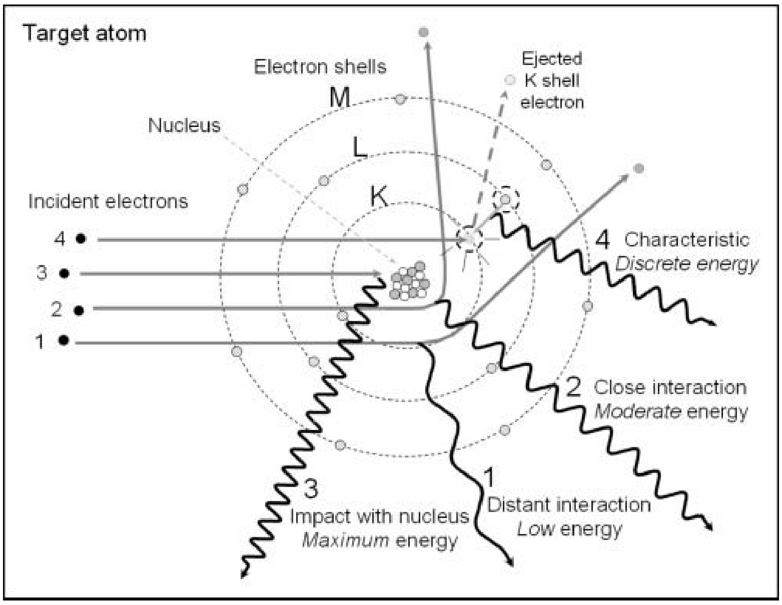

Fig. 2.3: Overview of X-ray generation processes during electron interactions, 1–3: bremsstrahlung production, 4: characteristic radiation production [50].

2.1.3 Inverse Compton scattering

Cutting edge laser systems have capability to achieve ultra-high intensities, surpassing the intensity of 10^{20} W/cm^2. These extreme conditions enable **inverse** (or non-linear) **Compton scattering**, a process that generates highly energetic X-ray and γ radiation [51]. During this phenomenon a high-energy electron interacts with a low-energy photon from a laser pulse, resulting in the production of a high-energy photon and a low-energy electron (see Fig. 2.4). The energy is thus transferred from an electron to a photon (as opposed to standard Compton scattering, where the energy is transferred from a photon to an electron).

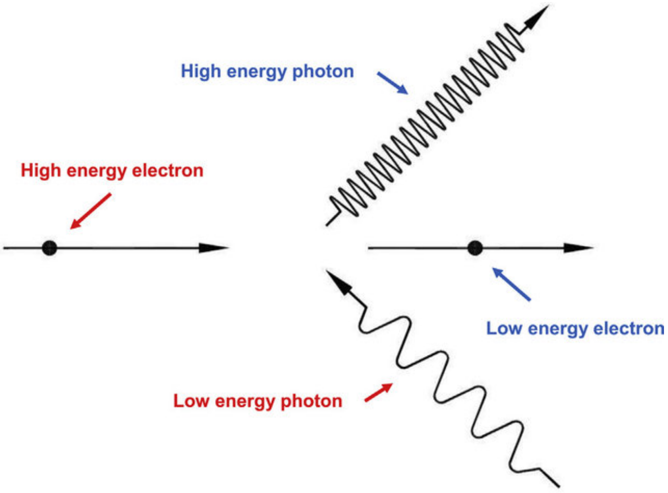

Fig. 2.4: Diagram of inverse Compton scattering. Energy of a high energy electron is transferred to a low energy photon. [52]

2.2 Properties of laser-generated X-ray radiation

The individual processes described in the previous sections can generate various distributions of X-ray radiation, both in the energetic and spatial domain. As detailed reliable experimental data are scarce, simulation results are shown when the experimental results are not available.

2.2.1 Energetic distribution

When achieving the laser intensity within interval $10^{14} - 10^{17}\,\mathrm{W/cm^2}$, multiple experiments have confirmed production of X-rays [49, 53, 54]. A typical cumulative spectrum shows a Maxwellian shape with characteristic lines as shown in Fig. 2.5. It should be noted that the cumulative spectrum can only be measured in high-repetition rate and stable environments, as to measure the spectrum, only one X-ray photon must be detected per shot. However, if these requirements are met, a standard detector can be used to acquire the cumulative spectrum.

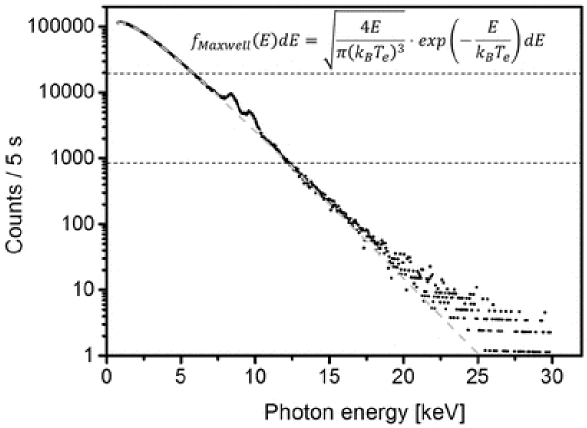

Fig. 2.5: A measured X-ray spectrum for $2.6 \cdot 10^{14}\,\mathrm{W/cm^2}$ laser pulses focused on a tungsten target. [49]

At higher laser intensities, the collective absorption process gives rise to the generation of a population of hot electrons, thereby inducing a change in the X-ray spectrum shape. The presence of these hot electrons contributes to the emergence of a more energetic bremsstrahlung component [55], consequently resulting in a bi-Maxwellian shape of the X-ray spectrum as seen in Fig. 2.6. It should also be noted that the number of hot electrons is significantly lower than the number of cold ones.

As the inverse Compton scattering process emerges at ultra-high laser intensities, another population of high-energy photons is generated. Both inverse Compton scattering and bremsstrahlung processes create a Maxwellian spectrum of X-rays [51]. Maxwellian temperatures of these distributions can be different for the two processes (see Fig. 2.7), the combined photonic spectrum at high laser intensities can have a bi-Maxwellian or even a tri-Maxweliian shape [57].

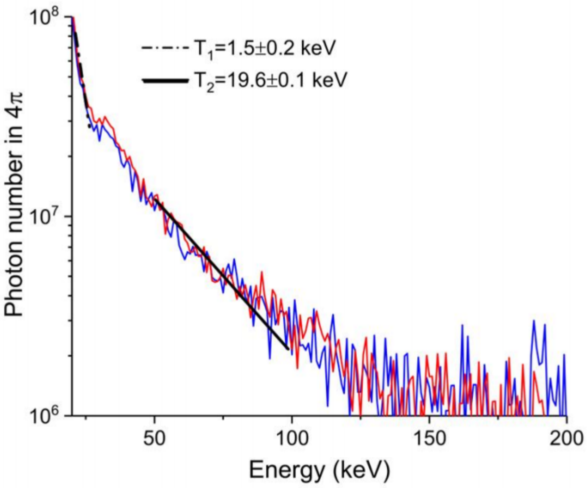

Fig. 2.6: Measured X-ray bi-Maxwellian spectrum for laser of intensity $I \approx 10^{18}$ W/cm^2 focused on a titanium target (using the Timepix detector). [56]

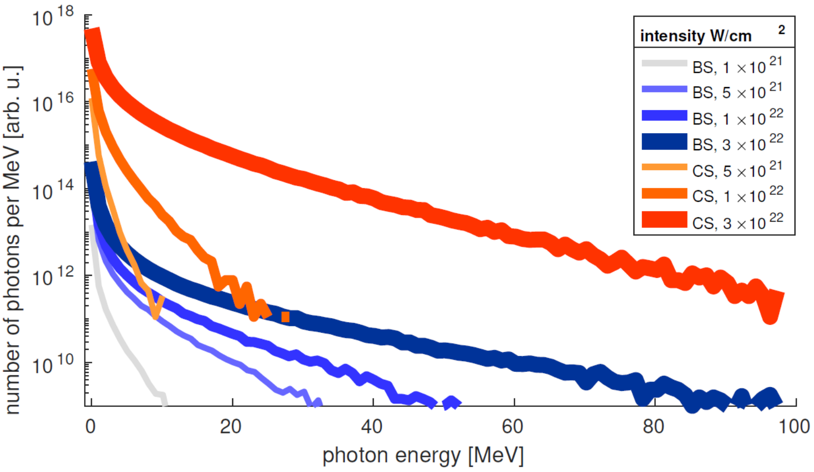

Fig. 2.7: Simulated spectra for bremsstrahlung (BS) and inverse Compton scattering (CS) for different laser intensities on target. [57]

2.2.2 Angular distribution

As for the angular distribution of the generated radiation, simulations show a difference between bremsstrahlung and inverse Compton scattering. The distribution of bremsstrahlung is dependant on the target thickness, since the target material can cause significant shielding [51]. For thin targets, the angular distribution is approximately isotropic, see Fig. 2.8. The inverse Compton scattering instead generates more directional radiation, the photons are more distributed in the forward direction, at a sharp angle to the laser pulse [57], see Fig. 2.9.

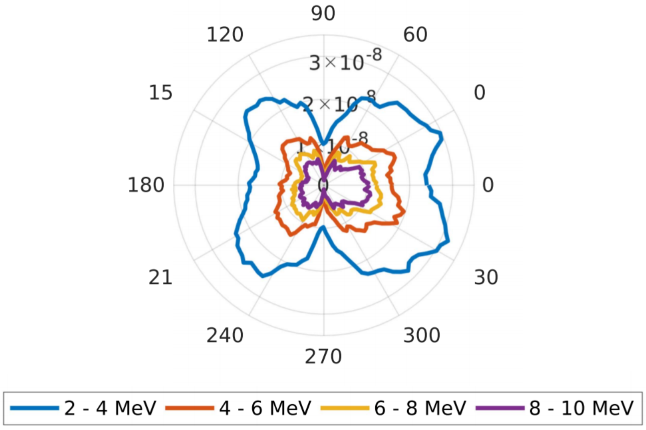

Fig. 2.8: Simulation of bremsstrahlung angular distribution from a 5 μm aluminium target. [57]

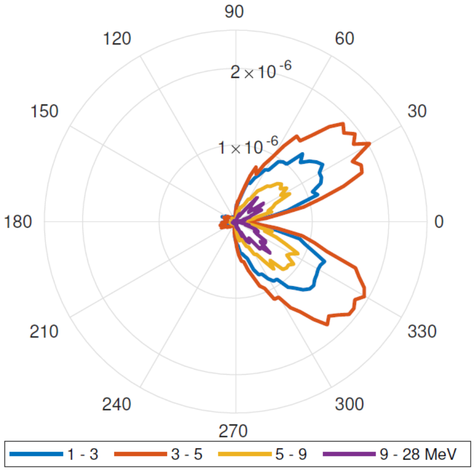

Fig. 2.9: Simulated angular distribution of photons created by inverse Compton scattering by a 10^{22} W/cm^2 laser pulse on a 3 μm aluminium target. [51]

2.2.3 Summary of laser-generated X-ray properties

In summary, the spectrum of X-ray radiation generated by a high-intensity laser pulse has a multi-Maxwellian shape, while the angular distribution of components generated by different processes can vary. The temperature and the maximum energy of X-ray radiation is linked to the laser intensity on the target, the ionisation process and the prevalent X-ray generation processes. An overview of prevalent processes and approximate expected maximal X-ray energies is shown in Tab. 2.1. It is important to highlight that this is a very simplified overview, as the energy of X-rays is influenced by various factors, including the properties of the target material, the wavelength of the laser and numerous other variables.

I[W/cm^2]	$> 10^{10}$	$> 10^{14}$	$> 10^{17}$	$> 3 \times 10^{18}$	$> 10^{21}$
Dominant process	Multiphoton and field ionisation	Collisional heating	Collective absorption	Relativistic acceleration	Inverse Compton scattering
Max E	1 keV	10 keV	100 keV	1-10 MeV	100 MeV

Tab. 2.1: Estimates of maximal X-ray photon energies at different laser intensity levels, based on information from [3].

2.3 Pulsed X-ray spectrometry

Spectrometry of X-ray radiation is a well-established field, there are many detectors on the market that enable precise measurements of the spectrum with a very good resolution. Most of these methods rely on the single photon counting, a precise measurement of energy deposited by individual photons inside the detector active medium [58]. However, while this method works well for conventional sources of X-ray radiation, it is almost impossible to be used for spectrometry of laser-generated X-rays.

The reason is the time-profile of the laser-generated X-ray pulse, that follows the time scale of the laser pulse. This can result in X-ray pulses as short as tens of fs. At this time scale it becomes extremely complicated (even impossible) to distinguish individual X-ray photons, since all processes that are used for measurements of energy deposition require much more time. Unfortunately, the speed of these processes cannot be improved, since even light does travel only 3 µm during 10 fs.

Consequently, if multiple X-ray photons interact within the active medium of the detector, the deposited energy is summed up and it is impossible to determine the original energies of individual photons. In high-flux environments as the experimental areas of ELI Beamlines are, this approach can thus be only used to estimate the beam intensity or dosimetric quantities, e.g. the ambient dose equivalent rate. However, in order to measure the spectrum generated by each laser shot, other methods that single-photon counting need to be exploited.

2.3.1 Single-photon counting adaptation

Before other possible techniques are discussed, it is necessary to note that it is possible to use the single-photon counting method for laser-generated X-ray spectrometry under the condition that is assured that no more than 1 photon interacts in the detector per shot. This can be achieved either by means of increasing the distance between the detector and the source, by decreasing the size of the detector medium or by collimation.

Secondly, as previously stated, this method can be used only at high-repetition rate (such as 1 kHz) lasers that produce (approximately) the same X-ray spectrum per each shot, since only 1 photon is counted per laser shot. Using this method, the spectra shown in Fig. 2.5 and 2.6 have been acquired. The example of an experimental setup is shown in Fig. 2.10.

In case of high-power large-scale laser systems, the conditions mentioned above are not fulfilled. Most of the large-scale systems do not achieve high repetition rates (e.g. the L4 Aton is able to shoot approximately once per minute [22]) and there are large shot-to-shot fluctuations. A theoretical solution to this problem would be to apply a large array of detectors that would enable to fulfil the condition of only 1 photon interaction per shot. However, such array would need to be very large and thus would be in real life impractical. This, therefore, raises a need for adopting a different method.

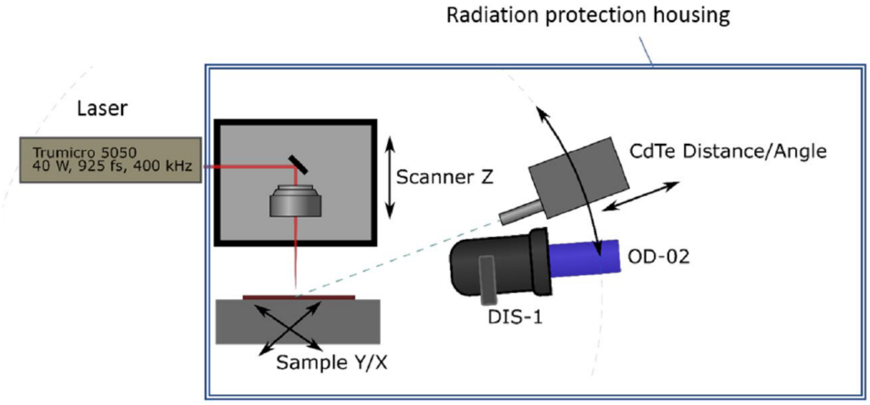

Fig. 2.10: An example of an experimental setup for X-ray spectrometry using single-photon counting method with a semiconductor CdTe detector. The detector together with its collimator is aligned with the laser-target interaction point, it is possible to move the detector along this line to ensure that only up to photon per shot interacts with the detector. [49]

2.3.2 X-ray diffraction method

One of the possible options for pulsed X-ray spectrometry is exploitation of the X-ray diffraction on crystal. Using a pixalated X-ray detector, it is possible to scan X-rays that have been reflected from the crystal with the angle that satisfies the Bragg law. Since the angle depends on the X-ray energy, it is possible to use this setup for X-ray spectrometry. Such detectors are called "Johann-type spectrometers". While the energetic resolution of such spectrometers is very good (up to 1 eV), the energy range where they operate is extremely narrow (approximately between 5 keV – 20 keV) [59]. These methods can thus be used only for this very narrow part of the X-ray spectrum.

2.3.3 Compton scattering method

While the spectrometry of pulsed X-ray radiation is challenging, the spectrometry of pulsed electrons can be done using standard methods that exploit the deflection of electron trajectory using a magnetic field. The detection of electrons can be performed by both active and passive spatially sensitive detectors (e.g, pixalated detector, image plates…). One option is therefore to convert the energy of an X-ray photon to kinetic energy of an electron by means of interaction with matter, more specifically by Compton scattering.

Experimental setup of one such device is shown in Fig. 2.11. This spectrometer allows estimation of the maximum energy of X-ray radiation, the Maxwellian temperature and the photon flux. The energy range of this specific device is 4 – 20 MeV, the energy resolution is 20 – 30 % [60]. While the principle of this device seems promising, it greatly suffers from low sensitivity, since the converter needs to be both very thin and also created from a low Z material. Moreover, this particular setup uses image plates, limiting its usage only to low repetition rate environments.

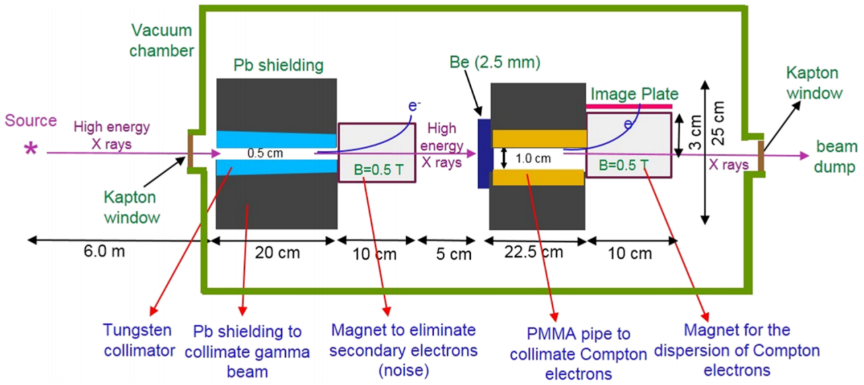

Fig. 2.11: A diagram of an experimental X-ray spectrometer, that uses Be converter and magnetic deflection of electrons in order to estimate energy of X-ray radiation. [60]

Another option of exploiting Compton scattering is tracking individual electrons using a pixelated detector, such as Timepix. The energy of individual X-ray photons can be determined by the estimation of generated electron energy and angle with respect to the photon beam, see Fig. 2.12. Experiments carried out have shown that such device is able to perform X-ray spectrometry in the region of 200 to 550 keV with a resolution of 20% [61].

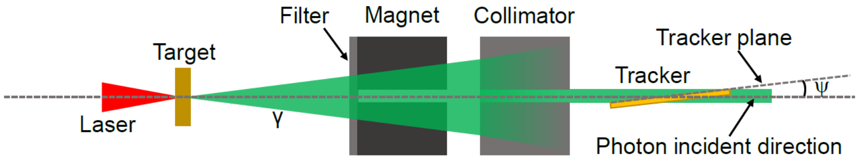

Fig. 2.12: A diagram of an experimental X-ray spectrometer, that uses electron tracking by a pixelated detector. [61]

2.3.4 Methods based on dose-depth profile

There are multiple designs of stack spectrometers that use passive detectors (such as radiochromic films, TLDs or OSLs separated by absorbers) to determine dose-depth profile in order to determine the spectrum of pulsed X-ray radiation. While in some cases the absorber is made from a single material, for low energy X-rays it is convenient to use multiple materials with different K-edges [62]. One such experimental device is shown in Fig. 2.13.

The stack spectrometers have much higher sensitivity than the devices that exploit Compton scattering. They can also be used at low-repetition rate laser-driven radiation sources for a shot-by-shot analysis. However, preparation and evaluation of these detectors is time-consuming and an online readout is not possible. Moreover, at high-repetition rate laser systems it is practically impossible to gain shot-by-shot data since it would be necessary to exchange the stack with a high frequency.

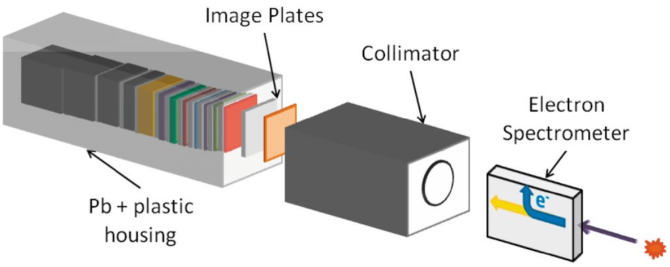

Fig. 2.13: A passive stack spectrometer experimental, multiple absorber materials are used. [62]

The problems of the passive stack spectrometers can be overcome by using active X-ray detectors instead of passive ones. Such stacks are routinely used in the field of high-energy physics in order to determine particle energy by fully absorbing its electromagnetic shower, hence the name "electromagnetic calorimeter". Design of these calorimeters can vary according to the experimental needs. They can have one or many layers and none or many different absorbers, the active medium can be a gas, a scintillator, or a semiconductor. One such calorimeter with semiconductor active detectors and polyethylene absorbers will be used to monitor energy of a γ-beam in ELI Nuclear Physics [63].

For the laser-driven experiments there is a tendency to prefer scintillators for the active medium, since both gas and semiconductor detectors could be influenced by electromagnetic pulses (EMPs) that are created during the laser-plasma interaction. The magnitude of these EMPs can be extreme, at ELI Beamlines it is expected that they can reach values up to 250 kV/m. Therefore, even when scintillators are used, it is necessary to shield any electronic readout from the influence of EMP. One option of EMP protection is a remote optical readout – an EMP shielded camera. An example of a camera readout from a calorimeter is shown in Fig. 2.14. In this case, the calorimeter is made of alternating layers of EJ-208 and bismuth germanium oxide (BGO) scintillators, without any absorber. The camera used for readout is Andor Neo (CMOS type).

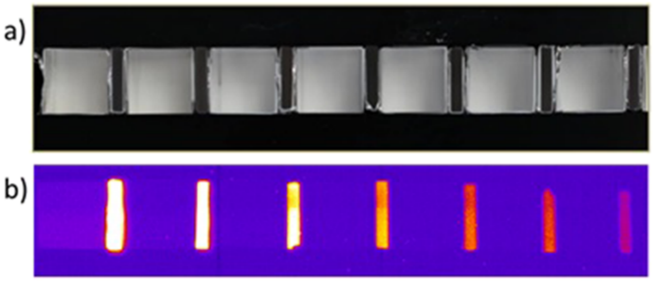

Fig. 2.14: a) picture of the calorimeter taken by the Andor Neo CMOS camera, b) camera image of scintillation light generated by a laser generated X-ray pulse [64].

While EMP represents a challenge for electronic readouts, it is possible to mitigate its effects by shielding the whole spectrometer using conductive materials (e.g. copper tape). Prototype of such calorimeter with electronic readout, was also previously developed and tested, this setup was using EJ-200 and PWO scintillators [65].

2.3.5 Method of choice for the developed spectrometer

Given the X-ray radiation parameters at ELI Beamlines (high energy and flux), the only feasible method from the options mentioned above is the one based on dose-depth profile. Also, as each laser shot can produce a different X-ray spectrum, it is necessary to be able to characterise X-ray radiation on a shot-by-shot basis. Given the high repetition rate of the ELI Beamlines laser systems, it is necessary to use active layers, as it would be impossible to exchange passive detectors within the calorimeter setup. The conceptual spectrometer design that considers all these requirements is discussed in the next chapter.

Chapter 3

Spectrometer conceptual design

The aim of this work is to develop a photon spectrometer to be installed in the ELI Beamlines experimental halls. Given the operational environment and the properties of the pulsed X-ray radiation described in the previous chapters, the requirements on the spectrometer are:

Radiation type:	photons
Energy range:	approximately 100 keV – 100 MeV
Resolution capability:	at least 2 Maxwellian temperatures (typically different by at least one order of magnitude)
Radiation fields:	ultra-short pulsed radiation fields
Operational regime:	real-time, data acquired and evaluated on a shot-by-shot basis at least with a 10 Hz frequency
EMP resistance:	up to 250 kV/m

Considering these requirements on the spectrometer, a segmented active calorimeter consisting of stacked scintillators read out using a camera was chosen as a suitable option from the methods described in the previous chapter. This type of spectrometer requires following components to be designed:

1. the scintillators (materials, dimensions…),
2. the holder for the scintillators,
3. the optical readout,
4. the optical shielding,
5. and the evaluation software.

However, before the individual components are designed, it is first necessary to describe the principle of function of the developed spectrometer.

3.1 Principle of function

In order to design the individual components, it is necessary to understand the driving principles of the developed spectrometer function. There are three main steps in performing spectrometry with this system:

1. the experiment – measurement of the scintillation light during irradiation and subsequent dose-depth curve evaluation,
2. the simulations – performing a set of Monte Carlo simulations in order to generate the response matrix,
3. the spectrum unfolding – evaluation by means of comparing the measured dose-depth curve with the response matrix and estimating spectrum parameters (e.g. energy).

3.1.1 Experiment

Prior to the irradiation, the calorimeter (i.e. scintillator stack) is aligned with the radiation source to ensure that the radiation beam gradually passes through individual scintillators. Also, a camera is aligned with the calorimeter to ensure that all the scintillators are within its field of view and in focus. During the irradiation, the radiation beam generates scintillation light inside the scintillators. The scintillation light is collected by the camera in a form of an image, that is subsequently processed and evaluated in order to obtain the dose-depth curve – the amount of scintillation light collected from individual scintillators, that is proportional to the energy deposited by the radiation beam (see Fig. 3.1).

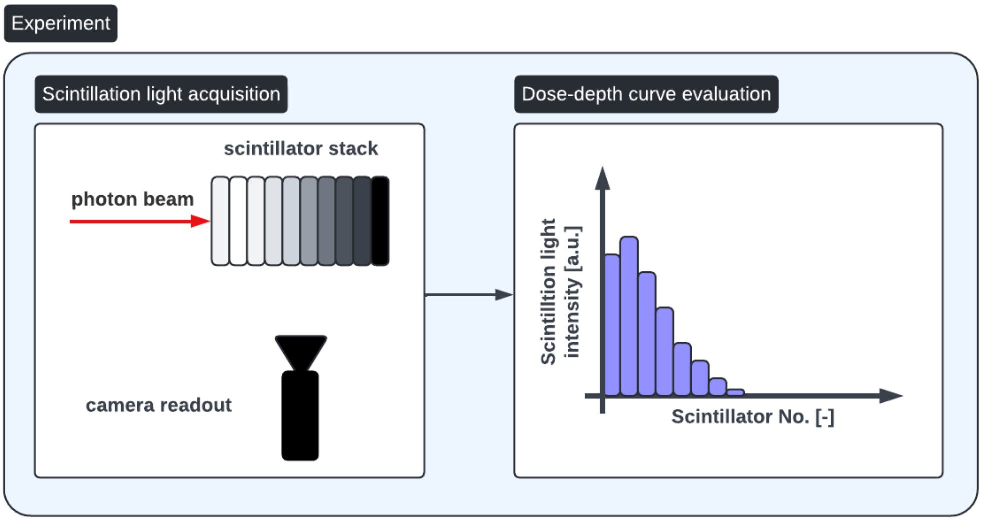

Fig. 3.1: Concept of dose-depth curve measurement using the scintillator stack. The different amount of scintillation light collected from individual scintillators is indicated by different shades of grey.

3.1.2 Simulations

The second necessary step is performing a set of Monte Carlo simulations in order to determine the dose-depth curve shape for a selected parameter (or a set of parameters of the beam), e.g. the photon beam energy. While it is possible to directly evaluate the number of emitted scintillation photons from a scintillator using simulations, it is sufficient to evaluate the deposited energy in the scintillators instead. This is because the number of scintillation photons is proportional to the deposited energy. The set of all evaluated dose-depth curves form the response matrix (see Fig. 3.2).

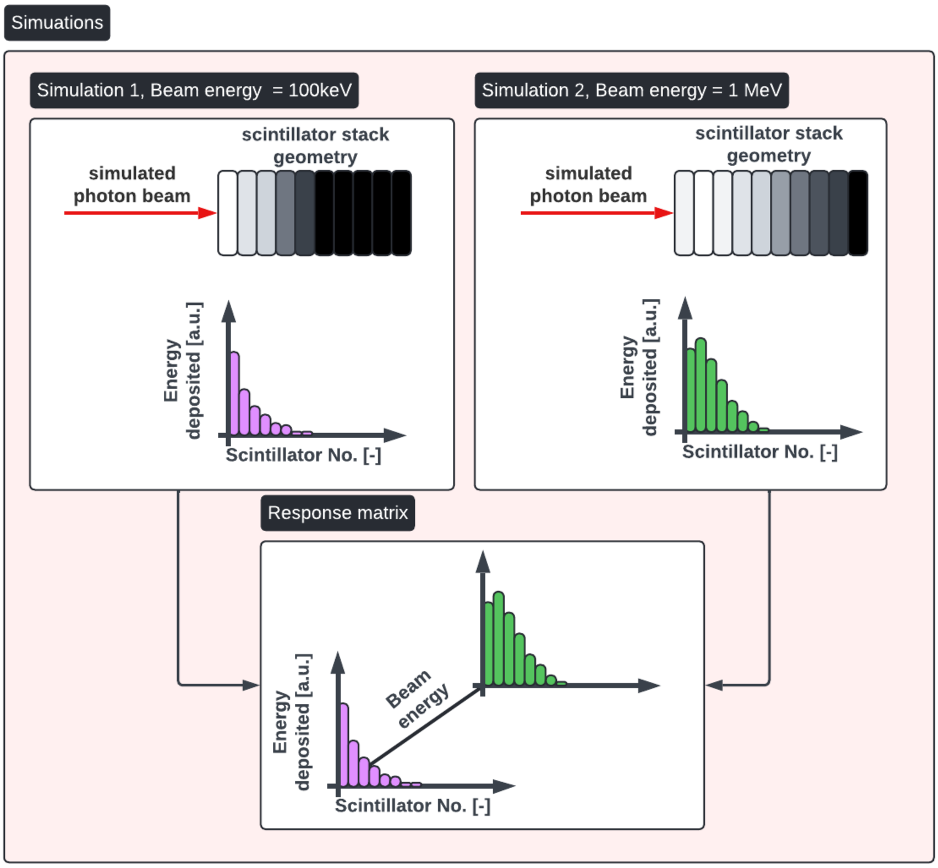

Fig. 3.2: Concept of response matrix generation using a set of simulations with different beam energy, in this case 100 keV and 1 MeV. The different energy deposited (that is proportional to the amount of scintillation light) in individual scintillators is indicated by different shades of grey. The dose depth-curves are combined into the response matrix as indicated in the bottom part of the figure (in this case only two dose-depth curves are displayed, in practice there are multiple dose-depth curves present).

3.1.3 Spectrum unfolding

With the experimental dose-depth curve acquired and the response matrix calculated, it is now possible to compare the measured curve with the simulated ones. The parameters (e.g. beam energy) of the simulated dose-depth curve that differs the least from the measured one are then considered as the result of the spectrometry (see Fig. 3.3). This process is typically called the spectrum unfolding.

It is also possible to compare a linear combination of multiple simulated dose-depth curves with the measured one, which is necessary if the radiation beam used in the experiment consists of multiple components. In that case the result would be a set of parameters. However, it should be noted this method does not allow a measurement of an arbitrary continuous spectrum as it is only possible to search for a limited set of parameters.

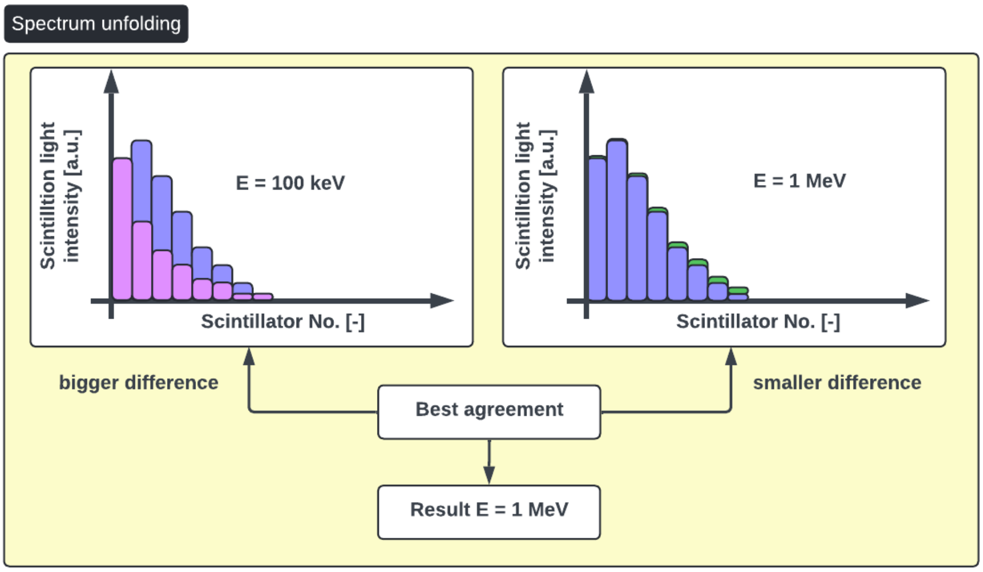

Fig. 3.3: Concept of the spectrum unfolding, the measured dose-depth curve (blue) is compared to the simulated ones (purple and green). The simulated curve that differs least from the measured one is used to determine the parameters of the beam (in this case the beam energy).

3.2 Conceptual hardware design

The primary spectrometer components are the scintillators and a real-time scintillation light detector. A set of scintillators produces scintillation light when exposed to an X-ray beam, this light is collected by a light detector. This setup is surrounded by an optical shielding, in order to prevent ambient light from reaching the optical detector. The data collected by this optical detector is then evaluated by a connected PC. The diagram of hardware conceptual design is shown in Fig. 3.4.

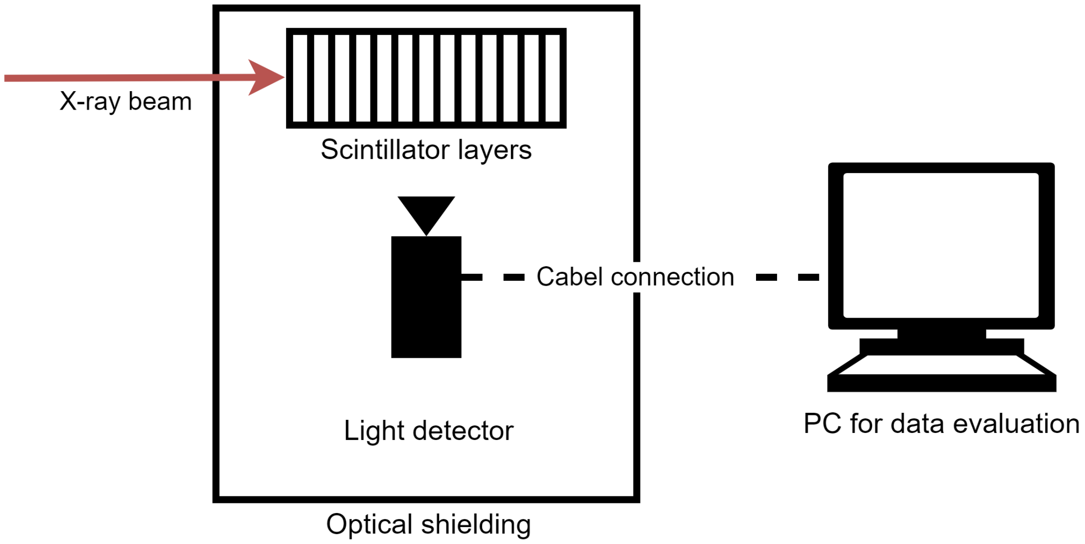

Fig. 3.4: Diagram describing the concept of the spectrometer hardware design.

3.2.1 Scintillator shape and dimensions

Given the need of an easy optical readout, a suitable shape of individual scintillators is a prism. The front faces of scintillators were chosen to be identical, because of the spatial constraints in experimental areas, the dimensions were designed to be 2 cm × 2 cm. The overall length of the spectrometer should not exceed 20 cm, also due to spatial constraints. The number of scintillators and their individual thicknesses are subject to studies that are described below.

3.2.2 Scintillating materials

As the required working energy range is wide, it is beneficial to assemble the spectrometer using two scintillating materials with different density, a low-density scintillator in the front part and a high-density scintillator in the back part. For the low-density part, the choice fell on the EJ-200 [66], a commercially available plastic scintillator. This material provides sufficiently high light yield of 10 000 photons/MeV at a wavelength of 425 nm, which is well-suited for standard optical detectors.

Two materials have been considered for the high density scintillator. The first one considered is PWO ($PbWO_4$), as its density is the highest among scintillating materials ($\rho = 8.28\,\mathrm{g/cm^3}$) and therefore is a common material for calorimetry in high energy physics. The drawbacks of PWO are its low light yield of 15–25 photoelectrons/MeV and its high cost (caused by its limited production).

Keeping the requirement on the high density and the cost containment, the material of choice became the BGO. While its density is slightly lower than the one of PWO ($\rho = 7.13\,\mathrm{g/cm^3}$), its light yield is much higher (8 200 photons/MeV). Given the fact that BGO is a material commonly used in industry, its price is also much lower than the one of PWO. Key parameters of chosen materials are summarised in Tab. 3.1. A diagram of the conceptual design of the calorimeter setup with its dimensions and materials is shown in Fig. 3.5.

Material	ρ [g/cm^3]	LY [photons/MeV]	λ [nm]	t [ns]	ϵ [cm]
EJ-200	1.03	10 000	425	2	14.4
BGO	7.13	8 200	480	300	2.1

Tab. 3.1: Key parameters of scintillating materials chosen for the construction of calorimeter. ρ is the density, LY is the light yield, λ is the wavelength of maximum emission, t is the decay time, and ϵ is the photon attenuation length at 1 MeV. [67]

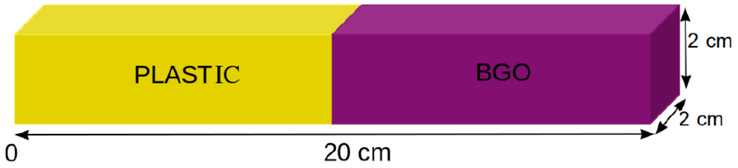

Fig. 3.5: Conceptual design of the calorimeter setup. First part is made of plastic scintillator, the EJ-200, second part of the BGO scintillator.

3.2.3 Optical readout

Numerous optical readouts can be used for collecting scintillation light, including photomultiplier tubes (PMTs), silicon photomulipliers (SiPMs), and photodiodes. As the aim of the spectrometer is to work in high-flux pulsed fields, it is also possible to use less sensitive optical detectors, such as charge-coupled device (CCD) or complementary metal-oxide-semiconductor (CMOS) cameras.

The main challenge regarding the optical readout is the presence of extreme EMPs within the experimental halls, as EMPs can influence the signal of the sensitive electronics. For example, as PMTs require a stable electric field to operate and are therefore extremely sensitive to EMPs [68]. Therefore, any sensitive electronics including the cables and power supply need to be properly shielded from EMPs.

As the development team did not have extensive expertise with PMTs, SiPMs, nor photodiodes at the time of development, but was more experienced with camera readout, a camera (CCD or CMOS) was chosen as a readout method for the spectrometer prototype. Also a significant advantage of the CMOS technology is relatively resistant to EMPs [69] compared to other more sensitive electronics. The use of a camera is in this case beneficial for several additional reasons, as a camera is:

1. easy to use and to read out using a standard PC,
2. commercially available,
3. highly customisable (lenses, filters).

However, as a camera chip is sensitive to ionising radiation, it is necessary to shield the camera from stray radiation during the experiment.

3.3 Conceptual software design

As stated in the previous section, the designed spectrometer requires a pre-calculated response matrix and a method for evaluating data. Therefore, the two key elements of the software part of the spectrometer are:

- the response matrix generation using Monte Carlo simulations and
- the unfolding algorithm for data evaluation.

3.3.1 Response matrix generation

The response matrix for a given scintillator configuration can be calculated by means of Monte Carlo simulation, a commonly used method that exploits numerical simulations of a set of particle trajectories and their interactions with objects present in the simulation geometry. A statistical analysis of the set of simulations allows estimating various quantities, including the deposited energy.

For the purposes of this thesis the FLUKA Monte Carlo code [10, 11] was chosen for the calculations as it allows simulation of energy deposition calculation by photonic radiation needed for the response matrix generation. Additionally, members of the development team are members of the FLUKA Collaboration and have extensive expertise with this tool.

FLUKA

FLUKA represents a sophisticated general purpose computational tool for simulating the interaction of particles with matter. FLUKA is distributed by CERN and thanks to its good reputation and reliability is a globally recognised tool for various radiation calculations.

FLUKA enables simulating various physical processes including electromagnetic and hadronic interactions, as well as transport phenomena such as energy deposition and particle transport. This software prioritises the integration and enhancement of contemporary physical models, employing microscopic models whenever feasible and ensuring consistency, conservation laws, and validation against experimental data. FLUKA features advanced capabilities for handling complex use-cases, including tracking of optical photons generated during an energy deposition within a scintillator.

Flair

FLUKA simulations can be prepared, run, and analysed using Flair, a graphical user interface for FLUKA [70]. Flair provides a graphical tool to build and inspect complex geometries, an interface to run FLUKA simulations various tools for plotting the results of the simulation.

Scoring

FLUKA allows calculating various quantities by means of statistical processing of individual simulations – the calculation of such quantity is called ”scoring” in FLUKA. The scoring used for the response matrix calculation is the energy deposited in the scintillators, as the energy deposited is proportional to the amount of generated scintillation photons. While it is possible to simulate directly the generated scintillation photons with FLUKA, it is more efficient to use energy deposition scoring for response matrix generation, as simulating the scintillation requires substantially more computing power.

Example of a 2D projection of energy deposition created in Flair is shown in Fig. 3.6. The response matrix can be created using a 1D energy deposition scoring along the calorimeter axes using a fine binning of 1 mm. Such dense binning enables usage of post-processing methods to further study the performance of a given calorimeter segmentation, that will be discussed in the next chapter.

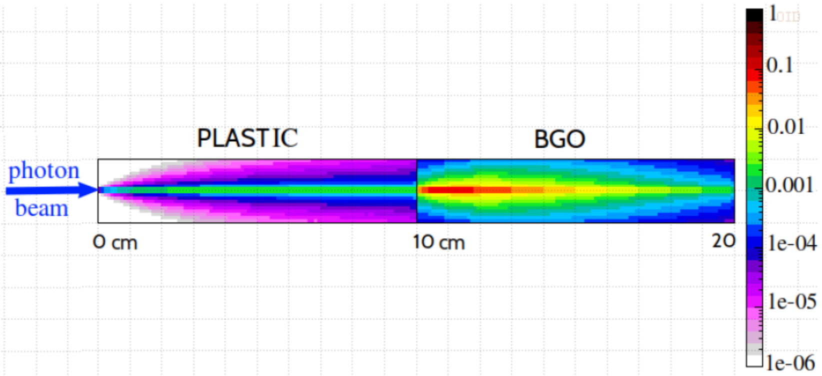

Fig. 3.6: Example of 2D energy deposition inside the calorimeter from a pencil-like photon beam with a Maxwellian distribution. The quantity plotted is the energy deposition density in GeV/cm^3 per primary.

3.3.2 Unfolding algorithm

In order to get the spectrum parameters, it is needed to evaluate the calorimeter dose-depth curve, i.e. signal $\vec{S}$ (S_i = energy deposited in the i-th scintillator) by the unfolding algorithm. Considering the calorimeter being simultaneously exposed to N_1 photons with a Maxwellian distribution of a temperature T_1 and N_2 photons of temperature T_2, the signal in scintillator i can be expressed as

$$S_i = N_1 \cdot f(i, T_1) + N_2 \cdot f(i, T_2), \tag{3.1}$$

where f is the interpolation function of the response matrix. The purpose of the unfolding algorithm is to determine N_1, T_1, N_2 and T_2 using only the signal $\vec{S}$ and the response matrix interpolation function f. Let $\overline{N_1}, \overline{T_1}, \overline{N_2}$ and $\overline{T_2}$ be guessed parameters that form a guessed signal

$$\overline{S_i} = \overline{N_1} \cdot f(i, \overline{T_1}) + \overline{N_2} \cdot f(i, \overline{T_2}). \tag{3.2}$$

Then let χ^2 function to be defined as

$$\chi^2(\overline{N_1}, \overline{T_1}, \overline{N_2}, \overline{T_2}) = \sum_{i=1}^{n} (S_i - \overline{S_i})^2, \tag{3.3}$$

thus expressing the difference between the acquired signal $\vec{S}$ and a guessed signal $\overline{\vec{S}}$. The principle of the unfolding is then the minimisation of χ^2 function, since

$$(N_1 = \overline{N_1} \wedge T_1 = \overline{T_1} \wedge N_2 = \overline{N_2} \wedge T_2 = \overline{T_2}) \iff \chi^2 = 0. \tag{3.4}$$

This minimisation can be done using various algorithms, the algorithm developed in the early stages of this spectrometer development is shown in Fig. 3.7. The first step of this algorithm is a grid search, during which the χ^2 function is calculated for all combinations of a pre-selected set of parameters $\overline{N_1}, \overline{T_1}, \overline{N_2}$ and $\overline{T_2}$. The combination that gives a minimum value of χ^2 is then saved for the second step, in which a fine χ^2 minimisation is done using the the gradient descent method, an iterative method where the next iteration of parameters is determined using the direction of the highest descent of the χ^2 function and a step size α. Once the following iteration does not significantly reduce the χ^2 function, the parameter set is considered as the final one.

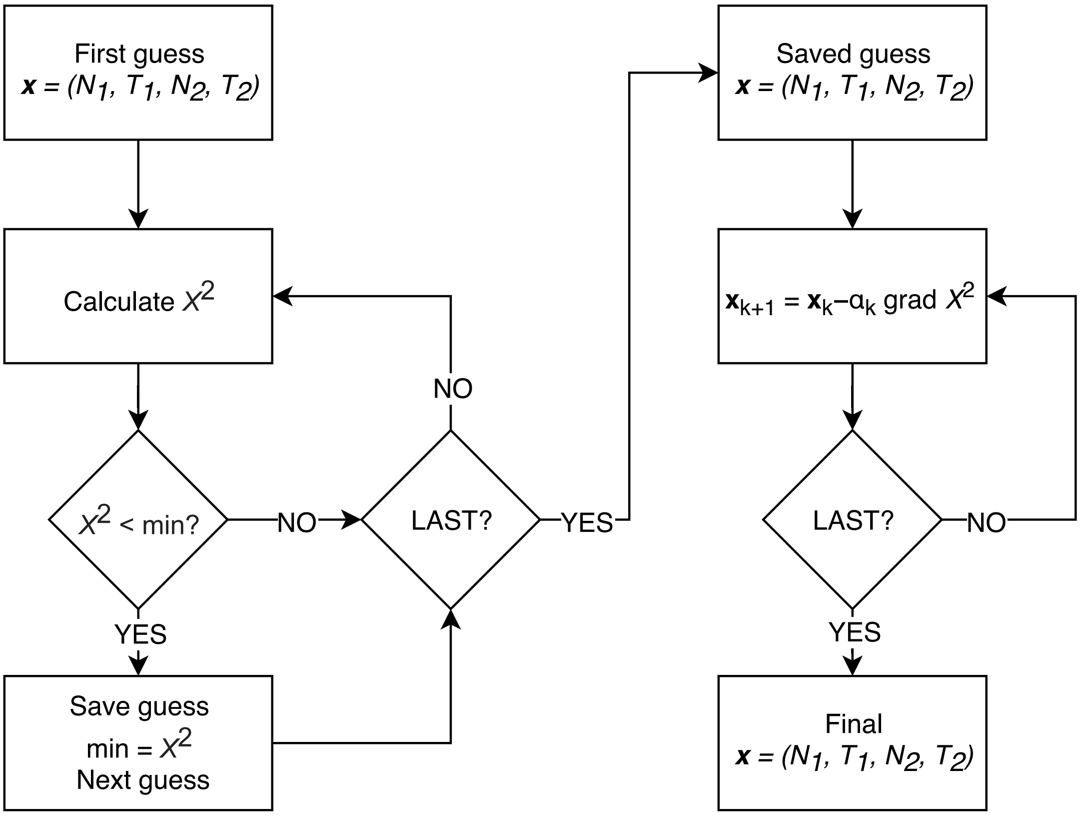

Fig. 3.7: Diagram of an unfolding algorithm that uses grid search as the first step and gradient descent as the second step.

3.4 Conceptual design summary

Summarising the principle of spectrometer function, the conceptual hardware and software design, these are the main conclusions of the spectrometer function and components:

- the designed spectrometer will consist of scintillating prisms of EJ-200 and BGO,
- the transverse dimensions of these prisms will be 2 cm × 2 cm, the third dimension is to be decided within the study described in the next chapter,
- the readout will be performed by a CCD or CMOS camera,
- response matrix will be calculated by FLUKA Monte Carlo code using energy deposition scoring
- parameters of the spectrum will be evaluated using an unfolding algorithm based on minimising the difference between measured and simulated dose-depth curves.

Regarding the designed spectrometer capabilities, it should be noted that it is not able to measure an arbitrary continuous spectrum, but rather several parameters of the assumed spectrum (e.g. Maxwellian temperature). The next steps of the individual spectrometer components design are described in the following chapter.

Chapter 4

Spectrometer hardware design

Following the conceptual design, it is necessary to design, build, and fine-tune the hardware part of the spectrometer. While for the purposes of this thesis the hardware and software designs are decoupled, it should be noted that throughout the spectrometer development, the software and hardware part were designed simultaneously, one influencing the design of the other. The first step of the designing process was the segmentation – the number and thicknesses of individual scintillators.

4.1 Segmentation

As mentioned in the previous chapter, all scintillators share the dimensions of the their front face (in the plane parallel to beam direction). However, the thickness of individual scintillators in the direction of the beam and the overall length are subject to optimisation. In order to decide appropriate scintillator thicknesses and overall length for usage at ELI Beamlines, a through study was conducted, consisting of following steps:

1. A simplified FLUKA simulation geometry was prepared for given lengths of the EJ-200 part and the BGO part. For the simulation purposes the EJ-200 part was one geometrical body and the BGO part was the second geometrical body, these were not divided at this stage into smaller scintillators (see Fig. 3.6).
2. A set of simulations was performed, scoring the energy deposited in 1 mm bins along the beam axis for variable beam energy (Maxwellian temperature), essentially calculating the dose-depth curves as if the calorimeter was composed of 1 mm thick scintillators.
3. In post-processing, adjacent scoring bins were grouped, summing energy deposited in these, in order to evaluate the dose-depth curve for variable scintillator thicknesses. This method allows for an efficient study of various scintillator thicknesses, as there is no need to rerun the Monte Carlo simulations for a different combination of scintillator thicknesses.

4. Evaluated dose-depth curves were combined into a response matrix.
5. Performance of different configurations (defined by EJ-200 part and BGO part lengths and the grouping of scored deposited energy bins) was evaluated based upon the precision of determining the parameters of a test beam consisting of multiple components using the respective response matrix.

These steps are described in detail in the following sections.

4.1.1 Simulation settings

The simulation geometry was set as in Fig. 3.5, the length of the EJ-200 and BGO part was varied for several simulations. The primary particle was set to be a photon, the beam spectrum was set as Maxwellian with temperature ranging from 50 keV to 40 MeV (simulations were performed for each 50 keV up to 1 MeV and for each 1 MeV in the range between 1 MeV and 40 MeV). The beam was set for simplicity as a pencil beam (point source, no divergence).

The physics default were set as PRECISIOn [71] in order to allow a detailed simulation of electromagnetic interactions. Additionally, the particle transport thresholds for electromagnetic particles (photons, electrons, and positrons) were lowered from default 100 keV to 1 keV in the EJ-200 part, in order to make the dose-depth calculation more precise in this low-density material. Also, the photonuclear reactions were activated to enable their simulation at high beam energies. The deposited energy was scored using USRBIN [72] scoring, these results were processed into a response matrix for a given geometry. The response matrix of the preliminary configuration of 10 cm of EJ-200 and 10 cm of BGO is shown for illustration purposes in Fig. 4.1. It can be seen that with increasing temperature the shape of the dose-depth curve changes, the maximum deposition moves further along the beam axis.

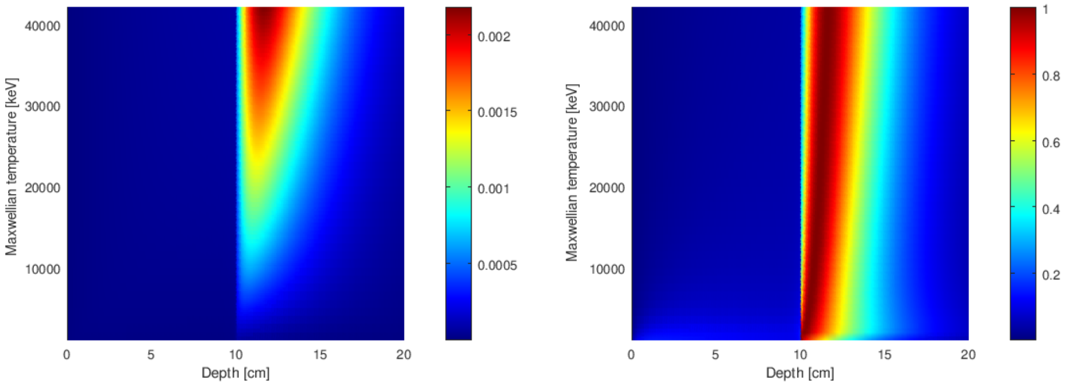

Fig. 4.1: Calculated response matrix for the configuration of 10 cm EJ-200 part and 10 cm BGO part with a 1 mm binning. The left plot colour axis shows energy deposition density in GeV/cm^3 per primary. In the right plot the energy deposition is normalised so that the maximum energy deposition along the calorimeter axis is equal to 1. Given the scale, the energy deposited in the EJ-200 part is not visible.

4.1.2 Performance evaluation

In order to evaluate the performance of a given geometrical configuration (using the respective response matrix), it is necessary to define a test beam on which the evaluation would be performed. As the spectrometer is designed for use at ELI Beamlines, this test beam was set according to expectations on the radiation produced at this facility, more specifically according to the cold and hot electron temperatures estimated by scaling laws for the parameters of the L3 HAPLS laser (maximum intensity $I = 10^{22}\,\mathrm{W/cm^2}$).

The test beam thus consists of two Maxwellian components that differ by more than one order of magnitude. Given these considerations, the low-temperature component was set to be approximately 200 keV and the high-energy one approximately 20 MeV. Also, in order to further test the capabilities of the unfolding algorithm, the temperatures were set not to be directly in the set of Maxwellian temperatures used for creating the response matrix. This is because if the components would be present directly in the response matrix, there would be a perfect agreement with these, causing a possible skew in the performance evaluation. Therefore, the low-temperature component was set to be $T_1 = 210\,\mathrm{keV}$, and the high-temperature one of $T_2 = 21.1\,\mathrm{MeV}$.

Additionally a noise component proportional to the square root of the energy deposited was added in order to simulate the noise present in the experiment. The amplitude of the components was chosen to be different from each other in order to test the ability of the algorithm to determine both amplitudes. Also, these values was chosen outside of the numbers that would be directly set during the grid search part of the unfolding algorithm, therefore values of 5.1 and 1.1 were used.

In conclusion, the test signal (dose-depth curve produced by the test beam) was calculated using FLUKA simulations with given Maxwellian temperatures and further processed to set the given amplitudes and the artificial noise as

$$\begin{aligned} S_i = 5.1 \cdot f(i, T_1 = 210\,\mathrm{keV}) + 1.1 \cdot f(i, T_2 = 21.1\,\mathrm{MeV}) + \\ + \sqrt{5.1 \cdot f(i, T_1 = 210\,\mathrm{keV}) + 1.1 \cdot f(i, T_2 = 21.1\,\mathrm{MeV})} \cdot \\ \cdot \mathrm{randg}(\mu = 0, \sigma = 10^{-3})), \end{aligned} \tag{4.1}$$

where f is the response function, i is the ordinal number of the scintillator within the scintillator stack and randg is a random number from a Gaussian distribution. This dose-depth curve thus simulates a measured signal to be analysed by the unfolding algorithm.

For the purposes of the designing process, the first version of the unfolding algorithm was developed according to diagram in Fig. 3.7. The performance of a given segmentation was evaluated by means of the relative error of determining each parameter of the test beam

$$\delta_x = \frac{|x - \overline{x}|}{x}, \tag{4.2}$$

where x is the parameter of the test beam (amplitudes and temperatures) and $\overline{x}$ is the parameter obtained by the unfolding algorithm.

4.1.3 Uniform segmentation

The first tests for segmentation calculation have considered the simpler solution, a uniform segmentation, where all the scintillators are of the same length. Firstly, the calculations were performed on the simple calorimeter with a 10 cm EJ-200 part and a 10 cm BGO part. The scoring was grouped in order to simulate a uniform thickness of all scintillators (2 mm, 4 mm, 10 mm, and 20 mm). Then, the test signal was evaluated using the respective response matrix and the unfolding algorithm, resulting in a set of evaluated parameters of the test beam. The relative errors of evaluating these parameters for different scintillator thicknesses are shown in Tab. 4.1.

Thickness of scintillators	δ_{N1}	δ_{T1}	δ_{T2}	δ_{N2}
2 mm	8%	15%	3%	3%
4 mm	17%	15%	3%	3%
10 mm	38%	38%	3%	4%
20 mm	60%	75%	8%	8%

Tab. 4.1: Relative errors of evaluated test beam parameters (N_1, T_1, N_2 and T_2) using response matrices obtained from a calorimeter with a 10 cm EJ-200 part and, 10 cm BGO part and a given thickness of scintillators.

The results show that with increasing scintillator thickness the relative error increases. This might suggest, that a very fine segmentation is required, however, the results also show there is no major relative error decrease when using a 2 mm segmentation compared to the 4 mm one. It should also be noted, that with decreasing thickness, manipulation with BGO crystals becomes more difficult due to their fragility. Therefore a reasonable compromise between the resolution and practicality is needed. In case of a calorimeter with a 10 cm EJ-200 part and a 10 cm BGO part and a uniform segmentation, this would lead to a choice of $\sim$ 4 mm thick scintillators.

The following study focused on determining the geometrical configuration of the calorimeter in terms of length of the EJ-200 and the BGO part, while keeping the segmentation uniform. By varying the length of the two parts, the lowest relative errors of evaluated parameters were achieved using a length of the EJ-200 part of 6 cm and the length of the BGO part of 14 cm, results of evaluation for this configuration are summarised in Tab. 4.2.

Segment thickness	δ_{N1}	δ_{T1}	δ_{T2}	δ_{N2}
2 mm	8.5%	9.7%	3.3%	3.0%
4 mm	9.2%	10.0%	3.2%	2.9%
10 mm	15.6%	14.1%	3.9%	3.6%
20 mm	12.8%	23.1%	3.5%	3.3%

Tab. 4.2: Relative errors of evaluated test beam parameters (N_1, T_1, N_2 and T_2) using response matrices obtained from a calorimeter with a 6 cm EJ-200 part and, 14 cm BGO part and a given thickness of scintillators.

4.1.4 Non-uniform segmentation

The profile of the response matrix shows (see Fig. 4.1) that the maximum of dose deposition is located in the very first centimetres of the BGO part. As the changes of the dose-depth curve are significant here, a more dense segmentation in this location (while keeping less dense segmentation in other parts) could improve the estimation of test beam parameters. Such more complicated, non-uniform segmentation was thus subject to further studies, also the overall calorimeter length was varied in order to see the effect of such changes.

An overview of parameter estimation relative errors of various non-uniform segmentations is shown in Tab. 4.3. These configurations consisted of different segmentation both in the EJ-200 part and the BGO part with a denser segmentation in the frontal part and a less dense segmentation in the rear part.

1	2	3	4	5	6	7	8	9	10	11	12	13	14	15	16	17	18	19	20	21	22	δ_{N1}	δ_{T1}	δ_{N2}	δ_{T2}
5	5	10	10	20	4	4	4	4	4	10	10	10	10	10	20	20	20	20	20			7.9%	21.6%	5.2%	7.0%
10	10	10	10	10	4	4	4	4	4	6	7	7	10	20	80							7.8%	21.8%	5.1%	6.9%
10	10	10	10	10	4	4	4	4	4	6	7	7	10	20	20	20	20	20				7.2%	20.7%	5.1%	6.9%
10	10	10	10	10	10	4	4	4	4	4	6	7	7	10	20	70						8.2%	14.0%	2.6%	2.3%
10	10	10	10	10	10	4	4	4	4	4	6	7	7	10	20	35	35					7.3%	13.6%	2.8%	2.5%
10	10	10	10	10	10	5	5	5	5	5	5	5	5	10	10	10	10	10	25	25		10.2%	13.5%	3.3%	3.1%
10	10	10	10	10	10	5	5	5	5	5	5	5	5	20	20	20	20	20				9.7%	12.2%	3.1%	2.9%
10	10	10	10	10	10	5	5	5	5	5	5	5	5	10	10	10	10	10	50			9.5%	10.3%	3.1%	2.8%
10	20	40	5	5	5	5	10	10	10	20	20	20	20									12,6%	13,0%	3,1%	3,0%
10	10	10	10	10	10	10	5	5	5	5	5	5	10	10	10	10	10	10	10	10	10	9.9%	11.4%	2.7%	2.5%

Tab. 4.3: An overview of 10 selected non-uniform segmentation calculations. Values in blue show the length of a EJ-200 segment (in millimetres), while the values in green show the length of a BGO segment.

This study has shown that a non-uniform segmentation leads to a slightly better performance of the spectrometer, therefore, the calorimeter would consist of scintillators of different thicknesses. Given the variety of experiments in which the spectrometer is supposed to be used and no configuration having significantly better performance than the other ones, it is beneficial to keep the segmentation variable.

Given these conclusions, it was decided to have multiple scintillators of different thicknesses (5 mm, 10 mm, 25 mm, 50 mm) manufactured and the segmentation could be changed regarding to the experimental needs. An example of a configuration with non-uniform segmentation is shown in Fig. 4.2. Once this step was completed, the next logical step was the design of the holder of the scintillators, that is described in the next section.

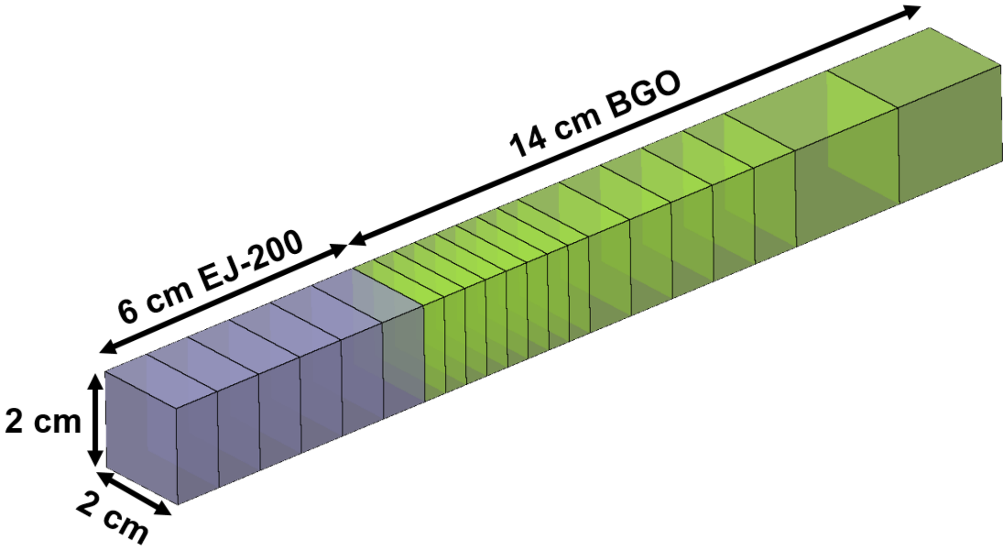

Fig. 4.2: An example of non-uniform segmentation design Flair [70] geometry. It consists of two scintillator types, the EJ-200 (purple) and the BGO (green).

4.2 Scintillator holder

A dedicated scintillator holder is required to hold the scintillator stack in place, to align it with the radiation beam and keep it aligned during the experiment. The holder should also allow simple manipulation and should not significantly influence the radiation field. The design of individual holder prototypes is described in the following sections.

4.2.1 Provisional holder

The first experiments were performed using a simple provisional metallic holder with plastic plates as seen in Fig. 4.3. This holder did not apply any force on the scintillators and was therefore unable to keep the scintillators properly aligned when exposed even to slight vibrations. Also, manipulation of the whole setup was rather complicated as well as its alignment, given that no force was present to keep the stack together.

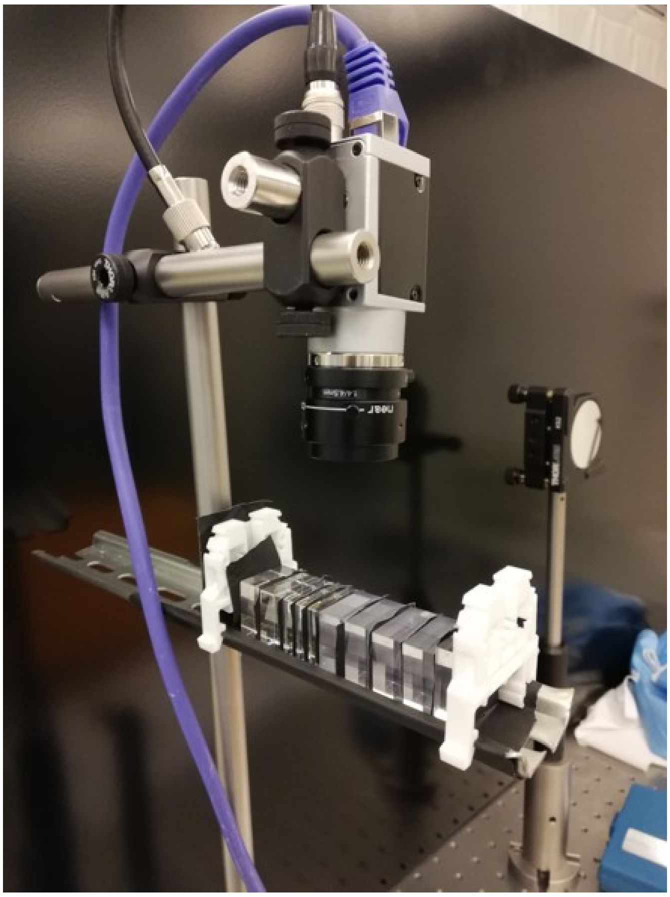

Fig. 4.3: Provisional version of the holder consisting of a metallic bar and plastic plates. This holder required the camera to be placed above the scintillators. A black fabric is placed between the scintillators to prevent scintillation light crossing between the scintillators.

4.2.2 Polystyrene holder

For following tests the scintillators were placed inside an expanded polystyrene holder (see Fig. 4.4) that was able to keep the scintillators aligned during the experiment. This holder was practical for experiments outside ELI Beamlines, as the expanded polystyrene provided protection of scintillators during their transport. Also, being very light and compact, it allowed simple manipulation during the experimental setup. However, as expanded polystyrene is not cleanroom compatible, this holder could not be used at laser-plasma experiments and was thus used only at experiments with conventional radiation sources.

Fig. 4.4: Second version of the holder consisting of an expanded polystyrene block. This holder enables the camera to be placed from side. However, this solution is not cleanroom compatible and thus was never used at laser-plasma experiments.

4.2.3 Aluminium holder

For the purposes of the laser-plasma experiments at ELI Beamlines a sophisticated aluminium holder was designed in collaboration with the engineering team of ELI Beamlines. Given the requirement on the cleanroom compatibility, aluminium was chosen as its material. The other benefits of choosing aluminium were its relatively low density, allowing easy manipulation. Also, given the low proton number of aluminium, the holder would not get extensively activated by high-energy radiation during experiments like stainless steel would. A sketch of the holder is shown in Fig. 4.5.

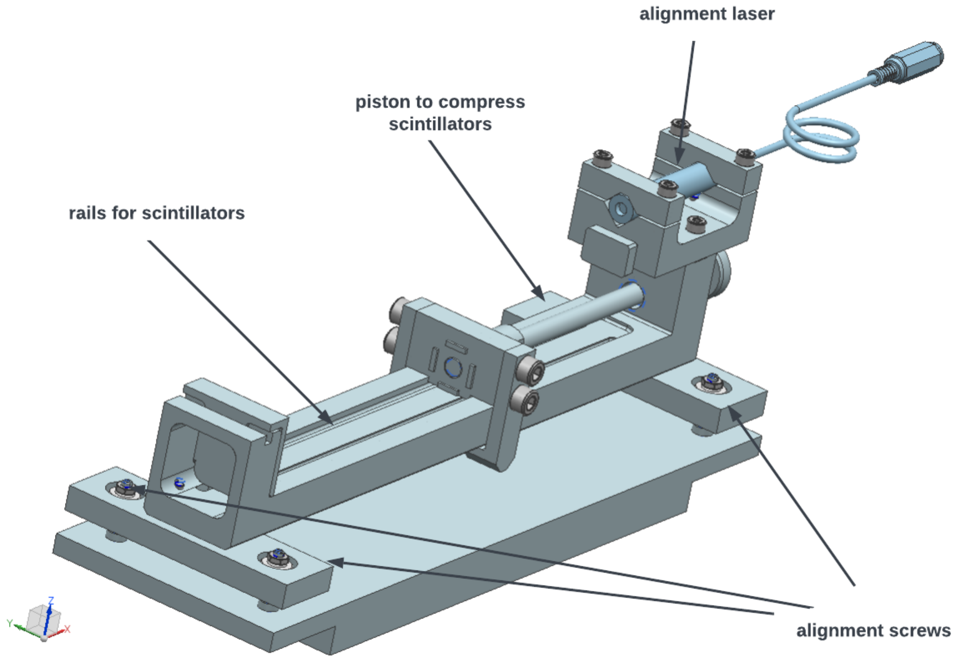

Fig. 4.5: Sketch of the aluminium scintillator holder design. Scintillators would be placed in the rails of the central part and compressed by the piston. The laser system at the top of the holder is dedicated to keeping the calorimeter aligned.

This holder was designed to be placed on top of an optical breadboard and secured with clams. Afterwards, central part would be aimed at the source of radiation using a alignment laser beam and positioning screws. Then, the laser alignment system would be placed at the top part to monitor the stability of alignment. Scintillators would be placed into the rails and be compressed by the piston. Nevertheless, this design was eventually abandoned, due to advances in 3D printing technology and a 3D printed holder being produced.

4.2.4 3D printed holder

Thanks to the advances in 3D printing technology it was possible to design and produce a 3D printed holder using a Prusa i3 MK3S 3D printer and a polyactic acid (PLA) filament. This holder proved to be reliable in alignment, mechanically resistant and cleanroom compatible. Alignment of this setup was performed using a crossline laser. It should also be noted, that production of multiple of these holders and their modification is very simple and cost-effective.

Fig. 4.6: Photo of the 3D printed calorimeter holder. Scintillators are placed in prepared slots, they are separated by a 1 mm PLA layer. The circular holes in the holder are used to attach the holder to other components (rods).

4.3 Readout

As the readout is to be done with a camera, there are several intertwined factors that need to be taken into account during the readout fine-tuning. The amount of optical photons emitted by a scintillator is relatively low, which poses a requirement on the quantum efficiency of the camera. Also, it must be possible to place the camera relatively close to the scintillators in order to maximise light collection efficiency, while at the same time it must be far enough to have all the scintillators within its field of view and to see the scintillators under a similar angle to ensure a uniform response across its field of view.

The low amount of scintillation light thus poses a requirement on the sensitivity of the camera. Generally, while more sensitive cameras produce better images, they are significantly larger and more expensive (due to the size of the CCD or CMOS chip and/or the cooling equipment). The same principle applies to camera lenses: the larger the lens aperture, the better the light collection, the higher the dimensions and the cost. Therefore, to find the most suitable solution, multiple cameras and lenses that were available were tested during this study.

4.3.1 Camera selection

The cameras tested were the Baser acA, Manta G-235B, and Andor Zyla 4.2. The testing process is described in the next sections.

Basler camera test

The first tests of the calorimeter readout were performed using a Basler acA industrial camera. The camera was tested with a 8 keV Cu X-ray tube with a photon flux of 10^8 photons per second. The whole experimental setup was enclosed within the X-ray hutch of the E1 experimental hall at ELI Beamlines (see Fig. 4.7). The X-ray hutch itself provided the optical shielding of ambient light for this experiment The goal of this experiment was to determine, whether an already available in-house camera is sufficient for the tests and readout. Unfortunately, this camera proved to be not sensitive enough to be used for the readout as can be seen in Fig. 4.8. Therefore, a more sensitive camera was needed.

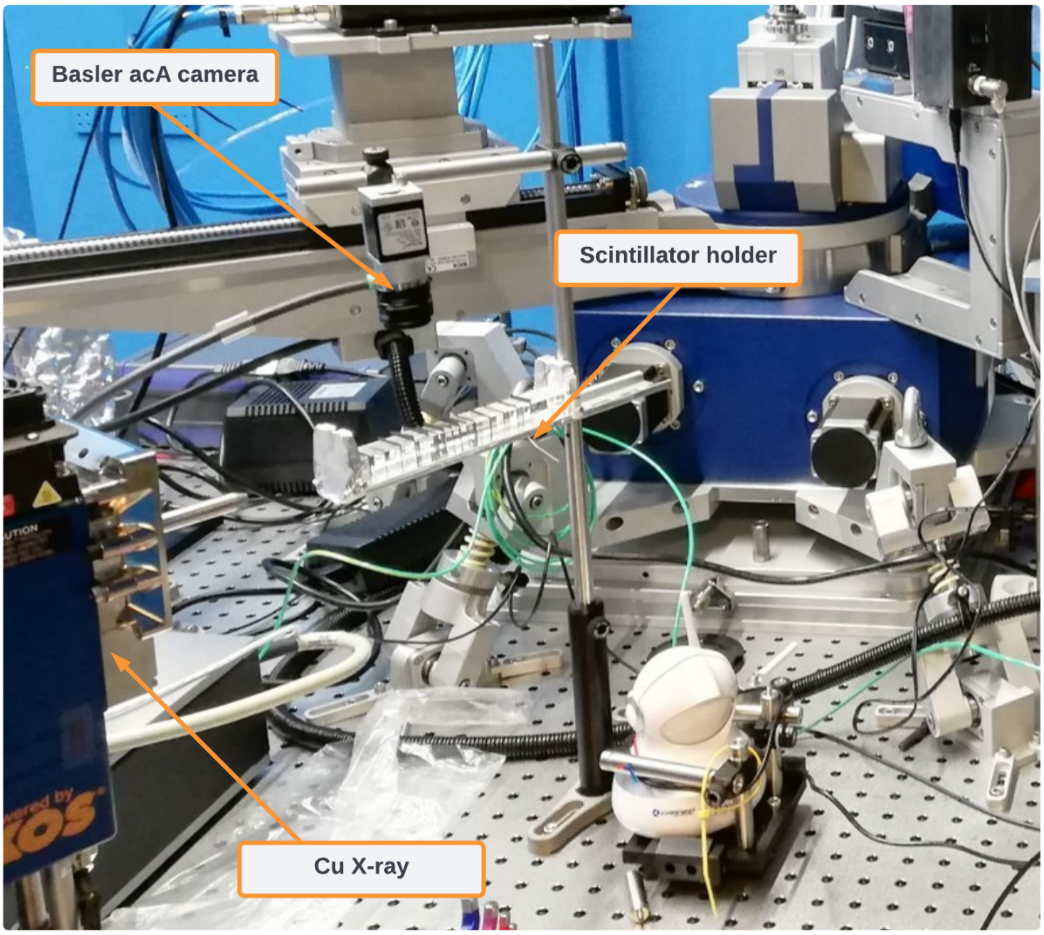

Fig. 4.7: Experimental setup of the calorimeter using a simple holder, Basler camera as readout and X-ray tube as a radiation source. Notice the camera is placed above the calorimeter.

Fig. 4.8: Images taken by the Basler acA camera prior to the irradiation and during the irradiation. The gain of the camera and the exposure time is set to maximum. The faint glow of the first plastic scintillator is seen in the right picture within the yellow circle. It is evident that this camera does not have sufficient quantum efficiency to be used for the spectrometer.

Manta and Andor camera test

The second experiment was performed using more sensitive cameras and a much stronger radiation source, the high energy bremsstrahlung beam produced by electrons accelerated at the conventional accelerator Mikrotron MT25 [73]. For this experiment, the scintillators were placed inside the expanded polystyrene holder. The calorimeter was aligned using a laser cross, the whole setup was shielded from scattered radiation using lead bricks and plates (see Fig. 4.9). The cameras used in this experiment were:

- Manta G-235B
  - resolution: 1936 × 1216
  - sensor: Sony IMX174, CMOS type
  - pixel size: 5.86 μm × 5.86 μm
  - lens parameters: focal length = 8.5 mm, aperture = f/1.3 mm
  - quantum efficiency: 60% at 425 nm, 70% at 480 nm [74]
- Andor Zyla 4.2
  - resolution 2048 × 2048
  - sensor: CMOS type
  - pixel size 6.5 μm × 6.5 μm
  - lens parameters: focal length = 16 mm, aperture = f/1.4 mm
  - approximate quantum efficiency: 50% at 425 nm, 70% at 480 nm [75]

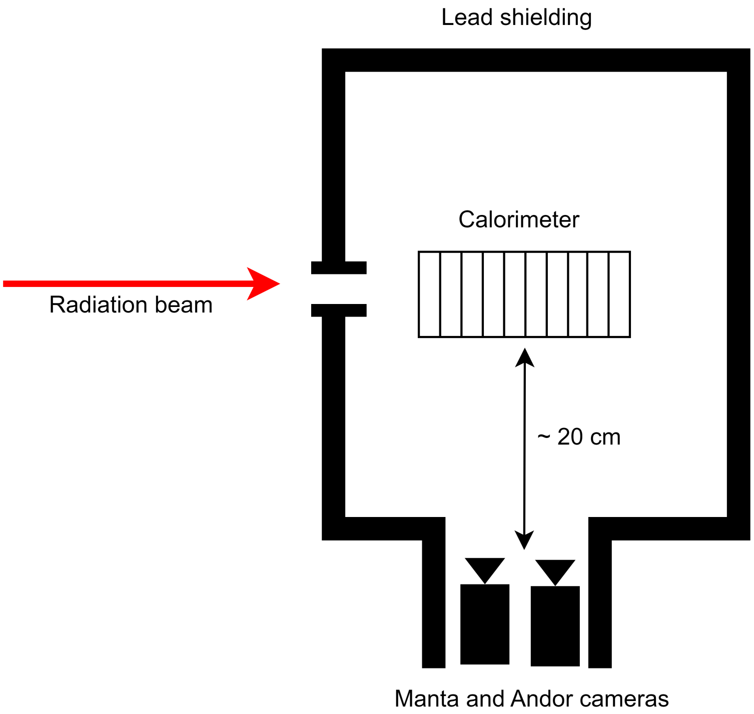

Fig. 4.9: Diagram of the experimental configuration during the Mikrotron experiment. Tested cameras were placed side by side, the distance between the cameras and the calorimeter was approximately 20 cm. The experimental setup was placed within a lead shielding bunker. The experimental area was dark, eliminating a need for optical shielding.

An image taken prior to the experiment with the Manta G-235B camera is shown in Fig. 4.10. An example of an image taken during irradiation (in this case with electron beam energy set to 23 MeV and with the use a photon converter) is shown in Fig. 4.11.

Both cameras were thoroughly tested, the quality of images acquired by these cameras was comparable. The choice thus fell on the more compact, simpler, and more affordable Manta G-235B camera. This experiment also verified the need for a proper ionising radiation shielding of the camera, as ionising radiation can cause noise while interacting with the CMOS chip.

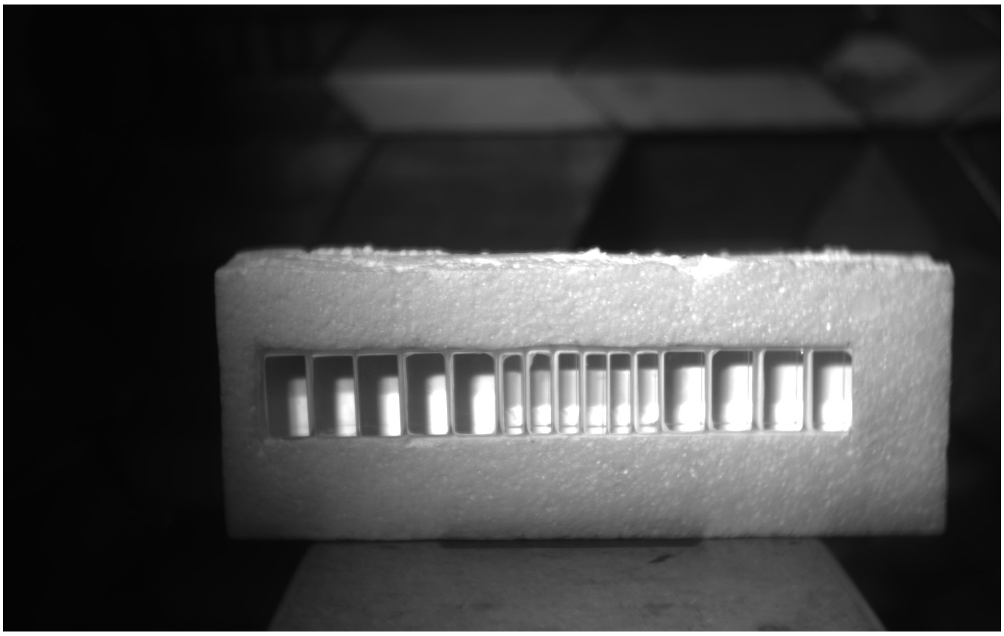

Fig. 4.10: Image taken by the Manta G-235B prior to the irradiation. Notice the use of the expanded polystyrene holder.

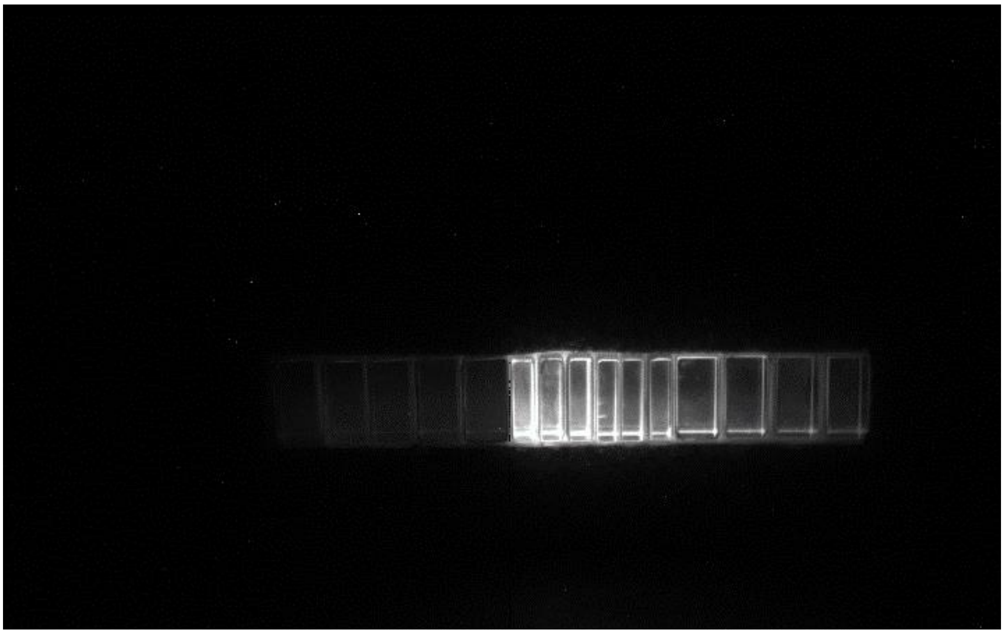

Fig. 4.11: Image taken by the Manta G-235B camera during the irradiation. The radiation beam is coming from the left, the plastic scintillators glow less than BGO scintillators due to high γ beam energy.

4.3.2 Camera to calorimeter distance

The distance between the camera and the calorimeter is subject to adjustment, as it significantly influences the spatial requirements of the whole system. The impact of increasing the distance between the camera and the scintillator was tested using a Cs-137 radioactive source (E = 661.7 keV, A = 37 MBq) and the Manta G-235B camera, focusing on the dependence of the pixel value (pv), that is proportional to the amount of light collected by a pixel, on the increasing distance. The radioactive source was moved alongside a single scintillator towards the camera. Every scintillator type (material and thickness wise) was placed at several distances and a signal was acquired by the camera.

The results have shown, that the pv does not change significantly with increasing distance (as seen in Fig. 4.12). Nevertheless, the number of pixels that collect light of the scintillation decreases with increasing distance, as the scintillator in the picture gets smaller with increasing distance. This effect subsequently causes higher uncertainty of the average pv, given the lower number of illuminated pixels. Long distances between the camera and the scintillators would also require an impractically large optical shielding from other light sources in the experimental setup, which would be difficult in laser-plasma experiments.

While a smaller distance between the camera and the scintallators would enable a compact optical shielding, it would also cause a parallax effect. The parallax effect would substantially complicate the readout of scintillators at the edge of the camera view, away from the centre of the taken image. These considerations have led to a compromise between the effects mentioned above, when the suitable distance was found to be approximately 20 cm - 22 cm. At this distance, when the centre of the calorimeter is aligned to the centre of the field of the camera view, the maximum angle by which the far scintillators are seen is 17 degrees. At this angle the parallax effect does not pose a significant issue as will be discussed in following sections and shown in Fig. 6.2.

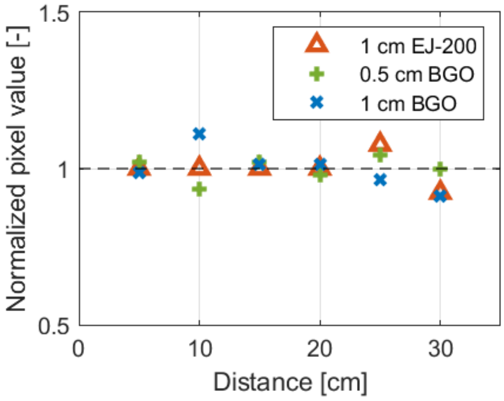

Fig. 4.12: Dependence of the average pixel value (normalised to the mean pixel value for each scintillator type) on the distance between the camera and the scintillator. No significant dependence can be seen. The errorbars are not visible, as the error of the mean is low given the large number of averaged pixel values.

4.4 Reflector and optical shielding

During the experiments dedicated to the camera selection, two issues have been identified:

- Substantial amount of scintillation light was not collected by the camera because no reflector was used. The low amount of light represents a problem as it increases noise within the collected signal.
- Black fabric was used during the first experiments to separate the scintillators (see Figs. 4.3 and 4.7), however, it was proven that it was not perfectly light-tight (using a laser beam) and thus enabled scintillation light to cross from one scintillator to another. This also represents a problem, as it affects the shape of the measured dose-depth curve.

4.4.1 Reflector

Given the low amount of scintillation light and limited quantum efficiency of the CMOS chips, it is essential to maximise the amount of collected optical photons in order to reduce the noise. One option to achieve this is to cover the scintillators with a reflector, keeping one side uncovered to enable the readout. The choice fell on the polytetrafluoroethylene (PTFE) tape, as it is simple to apply by wrapping, its reflectivity is relatively high, it is commercially available and cost-effective. The appropriate amount of PTFE to be applied on the scintillators was a subject to a dedicated experiment, where the dependence of the pixel value on the number of applied PTFE layers was studied using a Cs-137 source. The results showed that it is possible to substantially increase the amount of collected optical photons by applying the PTFE reflector, as seen in Fig. 4.13.

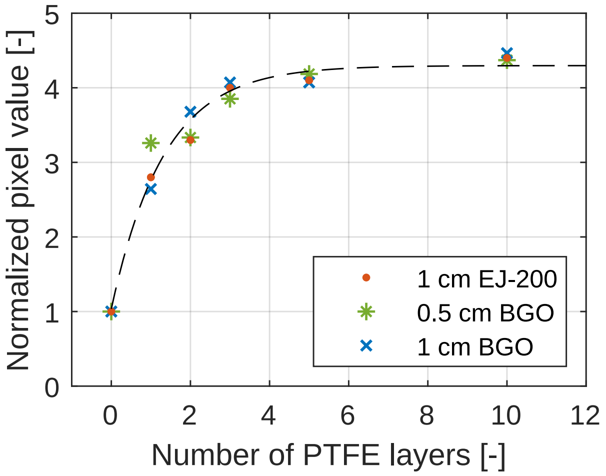

Fig. 4.13: Dependence of the normalised pixel value on the PTFE wrapping thickness. One PTFE layer is 0.09 mm thick.

In this figure, the very sharp increase in normalised pv can be observed in the region of low number of PTFE layers. A thin PTFE layer could thus cause issues, as a small difference in wrapping of individual scintillators would cause a different reflector thickness and would therefore lead to a significantly different light output. On the contrary, a large number of reflector layers would cause blockage of space while not significantly enhancing the light output (compared to e.g. one of 5 PTFE layers). Given these considerations, the appropriate number of reflector layers was determined to be 5, which is approximately 0.5 mm thick.

4.4.2 Optical barrier and shielding

As previously stated, the black fabric used in the first experiments was insufficient to prevent light crossing from one scintillator to another. While application of the reflector managed to reduce the amount of light crossing, it was still not able to completely reflect nor absorb all the light, so a fraction of the scintillation was able to pass through it.

Therefore, an optical barrier was integrated into the 3D printed holder (as seen in Fig. 4.6), using PLA layers of 1 mm. Such layer thickness completely prevented the light from passing from one scintillator to another, while also aided in keeping the scintillators at the correct position. Given the low density of PLA ($1.2 - 1.4$ g/cm^3), the presence of these barriers does not substantially influence the dose-depth curve. Nevertheless, both separators and reflector were subsequently included to the FLUKA geometry for further simulations and response matrix generation.

For the optical shielding of the full setup, a black aluminium foil (thickness 50 μm was used. This proved sufficient for a majority of experiments, as it was possible to switch off lights inside the laboratories and it was only needed to shield light from LEDs of other instruments. However, for further experiments at ELI Beamlines, a dedicated 3D printed optical shielding was created.

4.5 Hardware design summary

Following the considerations mentioned above, a prototype was produced with following parameters:

- Segmentation: 5 EJ-200 (1 cm), 6 BGO (5 mm), 4 BGO (10 mm) scintillators
- Holder: 3D printed PLA, attachable to other components
- Camera: Manta G-235B (by Allied Vision)
- Lens: focal length = 8.5 mm, aperture = f/1.3 mm
- Reflector: 0.5 mm PTFE
- Optical barrier: PLA 1 mm
- Optical shielding: black aluminium foil 50 50 μm

Picture of the prototype is shown in Fig. 4.14.

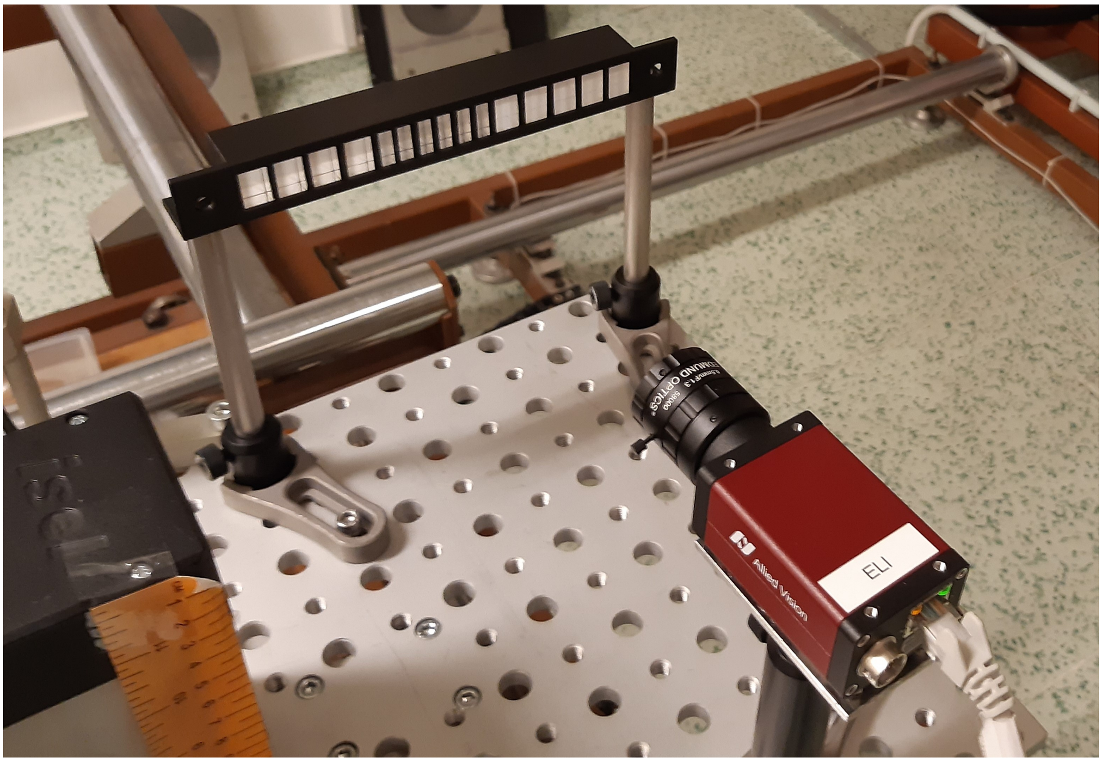

Fig. 4.14: Assembled prototype on an optical breadboard, consisting of 15 scintillators covered in PTFE, 3D printed PLA holder, and Allied Vision Manta G-235B camera connected to the PC for data taking. The optical shielding of the full setup is not installed.

Chapter 5

Spectrometer software design

The software part consists of the fine-tuned simulations for the final hardware configuration, the control software for the camera, and the data evaluation consisting of image processing and the unfolding.

5.1 Response matrix generation

One of the key elements of the spectrometer design is the response matrix. When the hardware prototype was completed, it was possible to prepare a detailed simulation geometry and calculate the response matrix by means of performing a large set of simulations for different beam energies. Moreover, the post-processing of simulation results was refined for subsequent use in the unfolding method.

5.1.1 FLUKA simulations

The FLUKA geometry of the calorimeter prototype is shown in Fig. 5.1. Simulations were run for a sequence of Maxwellian temperatures (as in the segmentation study) and monochromatic energies (5 keV to 1500 keV with a step of 5 keV up to 100 keV, 50 keV between 100 keV and 1000 keV, and 100 keV between 1000 keV and 1500 keV). As in previous simulations the transport thresholds were set to 1 keV in EJ-200 to allow for a more precise calculation of energy deposition and the simulation of photonuclear reactions was enabled.

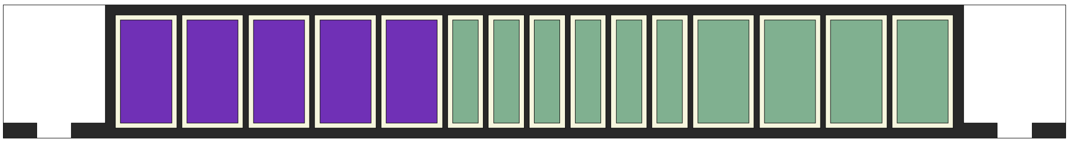

Fig. 5.1: FLUKA geometry of the calorimeter, a 2D cut at the middle of the calorimeter. EJ-200 scintillators are shown in purple, BGO scintillators in green, PLA in black, and PTFE in yellow.

Unlike in the segmentation study, in this case the scored quantity was the energy deposition in individual scintillators (as the scintillator size is already set and there is no need of grouping adjacent bins). There was also a difference in the beam size, that was int this case set to 2 cm × 2 cm, in order to better represent the situation when the radiation source is located sufficiently far from the calorimeter and the radiation beam impinges on the full frontal scintillator (with no collimation). This beam size setting is beneficial for general use of the spectrometer, however, it is possible to recalculate the response matrix for given experimental conditions (beam size, divergence, distance from the source) in order improve the accuracy of the spectrometry.

Simulations were defined and launched using a custom script that allowed parallel execution. A custom script was also used to process results of this set of simulations. Further simulation results processing into a response matrix was performed using a Matlab script.

5.1.2 Simulations results processing

Simulation results were normalised to GeV/cm^3 and further processed into the response matrix. For the following calculations it was also necessary to create a response function, an interpolation of the response matrix using the Matlab `interp2` function [76]. The `interp2` function is defined as

$$V_q = \mathrm{interp2}(X, Y, V, X_q, Y_q, \mathrm{method}) \tag{5.1}$$

where X and Y represent coordinates of points in value matrix V. In this case $X = 1, 2, , \dots, 15$ represents the ordinal numbers of scintillators, Y represents the temperature/energy vector corresponding to the response matrix and V is the response matrix. X_q and Y_q represents the query coordinates (ordinal number of scintillators and temperature/energy for which the interpolation should be calculated). The `spline` method, that exploits piecewise polynomials for interpolation, was used. This function was then wrapped using Matlab anonymous function [77], using following code:

```
responseFunction =
    (b,x)b(1).*interp2(
    1:numberOfScintillators,
    energyList,
    responseMatrix.depositedEnergy,
    x,
    b(2),
    'spline'
)';
```

where b represents parameters (amplitude and beam temperature/energy) and x represents the scintillator number. This function can therefore calculate the energy deposition density at x-th scintillator of the calorimeter, when exposed to $b(1)$ particles with temperature/energy $b(2)$.

5.2 Image acquisition

The camera is controlled by the Vimba Viewer software by Allied Vision [78]. This software allows setting exposition parameters and trigger types that best suit different operation modes - if the trigger is available from the radiation control system, it can be used to trigger the camera. If it is not available, the camera can be triggered manually, using a longer exposition time to ensure that all the scintillation light is collected after the laser shot.

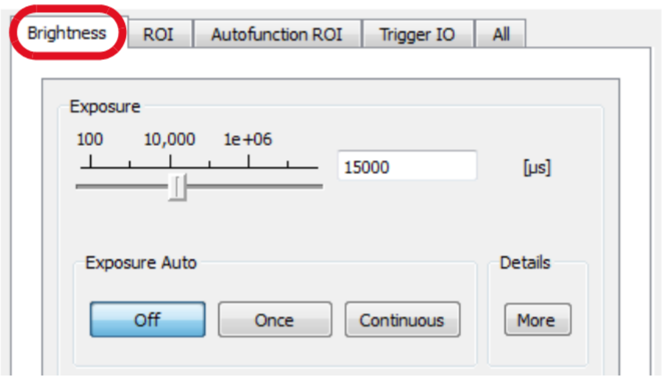

Exposure 15000 [µs]

Exposure Auto: Off

Fig. 5.2: Vimba Viewer interface settings of image acquisition, the tab Brightness where it is possible to set the acquisition time is highlighted. [78]

The image acquisition is then performed using these steps:

1. A reference image is taken without the full optical shielding to ensure that the camera is properly positioned and focused on the scintillators. The reference image can also be used for region of interest (ROI) definition – the area inside the image where the scintillators are.

2. A background image is taken with the optical shielding to ensure that the setup is properly shielded from optical light and to determine the noise level, that will be subtracted from the actual experiment images.

3. Experiment images are taken throughout the experiment, collecting the scintillation light.

5.3 Image processing

The experiment images acquired by Vimba Viewer are processed using Matlab:

1. The reference image is used to define the exact position and rotation of images, all the images are then rotated using the same angle.
2. ROI is selected using the reference image. This can be done either manually or using a dedicated Matlab code, that searches for the scintillators inside the holder.
3. Background is subtracted to compensate for the CMOS chip inhomogeneity, then the average pv of a background region of an image taken during irradiation is subtracted from all pvs to compensate for elevated background level.

The ROI selection was a subject to study as due to a corner effect, some areas of the scintillators are brighter than others. It was concluded that the most useful way is to choose ROIs outside of these bright zones, as this ROI selection leads to a most uniform area in terms of pixel value. Moreover, if the bright areas would be within the ROIs, a small change of ROI definition could have a large effect on the average pixel value.

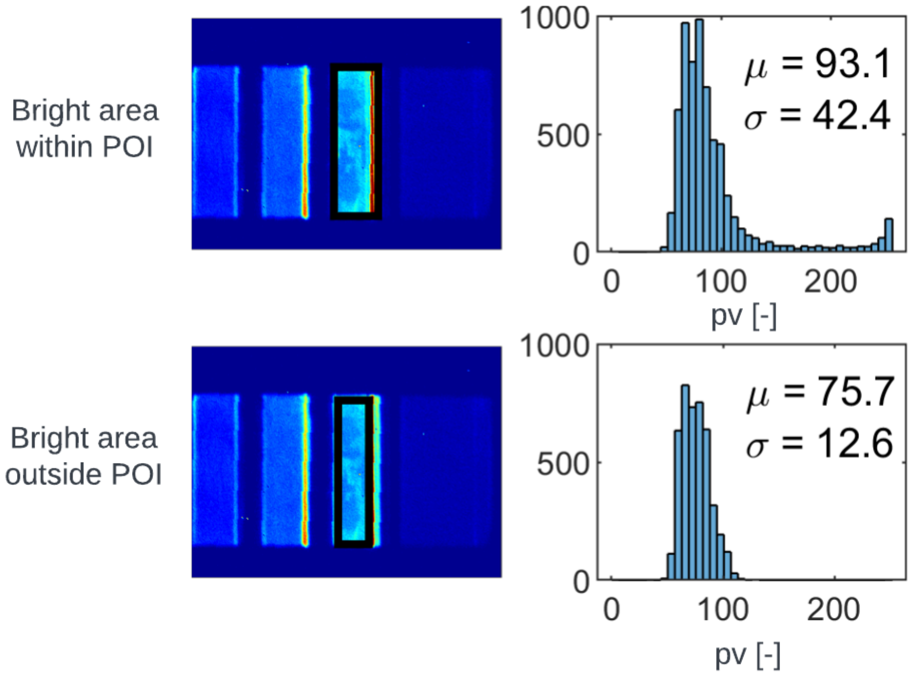

Fig. 5.3: ROI selection is marked by the black rectangle, histograms of the pixel values inside ROI are shown together with the mean of pixel values and the standard deviation estimate.

5.4 Unfolding

Once an experimental image is processed, it is possible to perform the unfolding. The final version of the unfolding was developed using Matlab function for fitting nonlinear regression models `fitnlm` [79]

$$mdl = \text{fitnlm}(X, y, \text{modelfun}, \beta_0), \tag{5.2}$$

where X are the scintillator ordinal numbers, y are mean pixel values with subtracted background in each ROI, `modelfun` is the response function as described in section 5.1.2 (i.e. interpolation of the response matrix). β_0 represents the initial set of response function parameters (amplitude and temperature/energy).

As the choice of β_0 significantly influences the results of the nonlinear model, it is essential to test multiple combinations of these values. This is done prior to the evaluation of the model, using the grid search algorithm enhanced by the Matlab function `parfor` [80] for parallel computation. Once the values of β_0 are found using the grid search, it is possible to evaluate the model, which provides not only the parameter values (amplitude and energy/temperature), but also the statistical errors, p-values, R^2, and R^2_{adj}. These quantities are essential for the spectrometer function as they provide a crucial information on the measurement accuracy.

Moreover, the `modelfun` can be set as a linear combination of multiple response functions, allowing for a search of multiple beam components, each defined by its function. Theoretically, it is possible to estimate as many parameters as the number of scintillators in the calorimeter, however, due to increasing statistical uncertainty, it is only practical to have the `modelfun` set as a combination of up to 3 response functions (and therefore be able to search for up to 3 temperatures/energies).

5.5 Summary of software design

The spectrometer software consists of 3 main components:

1. FLUKA for obtaining the simulation matrix,
2. Vimba Viewer for image acquisition,
3. Matlab for simulation processing, image processing, and unfolding.

FLUKA simulations are completed prior to the experiments, Vimba Viewer is used during the experiment, and Matlab can be used both during the experiment for online measurement or after the experiment for offline processing. The software architecture can be seen in Fig. 5.4.

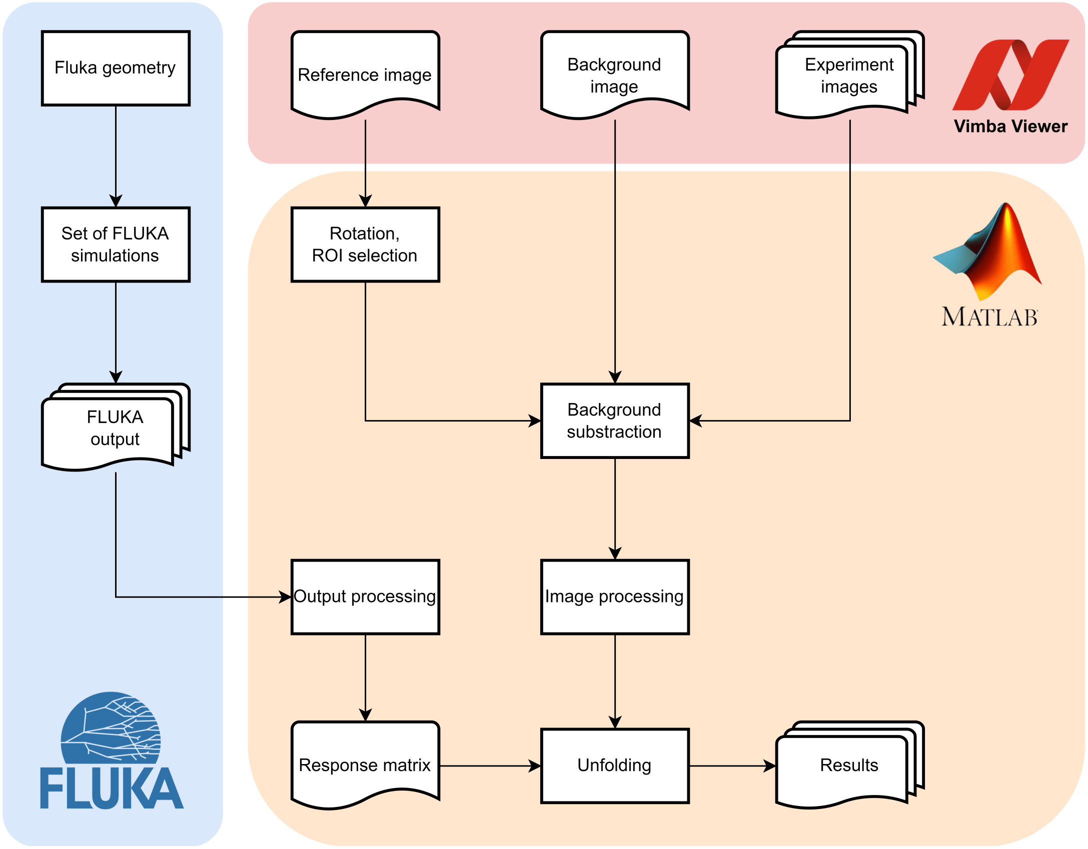

Fig. 5.4: Architecture of the spectrometer software. Simulations for response matrix generation are achieved by FLUKA simulations, image acquisition by Vimba Viewer, and other data processing is performed by Matlab.

Chapter 6

Spectrometer calibration and validation

The next necessary steps of the spectrometer development are its calibration and the validation of its function. The spectrometer requires a calibration to multiple factors that affect the amount of collected light by the camera in order to ensure that the dose-depth curve is measured accurately. Moreover, the spectrometer validation is needed to prove that the spectrometer is able to perform spectrometry and to determine the quality of such spectrometry. Both calibration and validation can be carried out using conventional sources of ionising radiation.

6.1 Calibration

The first step of the calibration process is the calibration of individual scintillators in terms of scintillation light output. The second step is the calibration of the scintillation light collection by the camera, that may be influenced by the angle, by which the camera sees the particular scintillator in its field of view.

6.1.1 Scintillator calibration

Ideally, all scintillators of the same scintillator type and dimensions should emit the same amount of scintillation light when exposed to an identical radiation field. However, the light output of individual scintillators may be influenced by the manufacturing process and the PTFE wrapping, that may differ for individual scintillators. In order to compensate for the differences in the light output, a calibration of individual scintillators was performed using an in-house Cs-137 source.

Scintillators were individually placed at a fixed distance from the camera and the radiation source, exposing them to the same radiation field. The light output was measured as a mean pixel value in the ROI. The results (see Fig. 6.1) show that while the response of the EJ-200 scintillators is uniform with negligible standard deviation and the mean pixel value of $pv = 41 \pm 1$, the standard deviation of mean pixel values for BGO crystals reaches significantly higher values. For the 0.5 cm thick BGO scintillators, the pixel value results in $pv = 120 \pm 10$, for the 1 cm BGO it results in $pv = 128 \pm 8$.

Therefore, in order to ensure an equal response of all scintillators of a scintillator type to the identical radiation field, a set of correction factors for individual scintillators was implemented. These factors are determined as the average pixel values in ROI of all scintillators of a scintillator type to the average pixel value in ROI of a given scintillator.

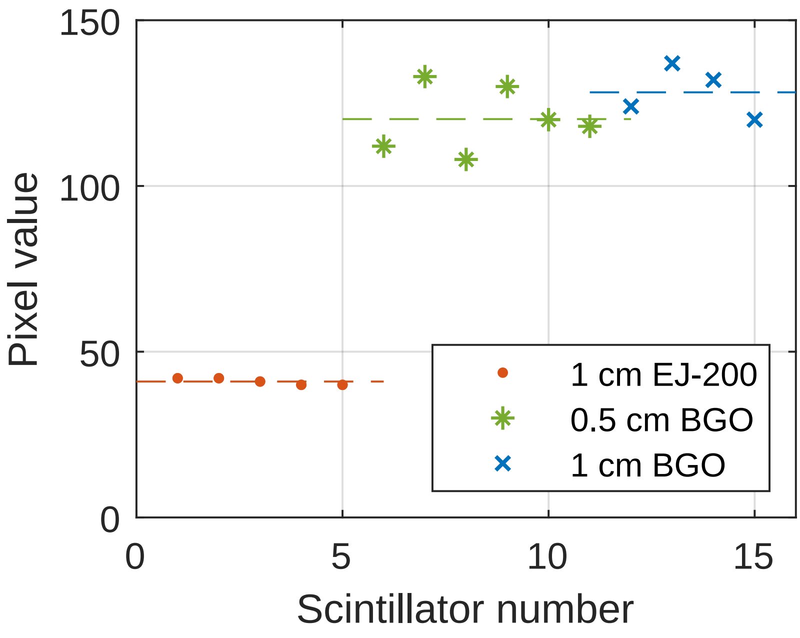

Fig. 6.1: Average pixel value in ROI for individual scintillators when exposed to the same radiation field. The errorbars are not visible due to the large number of pixels in the ROI.

6.1.2 Angle calibration

The amount of scintillation light collected by the camera from a scintillator also depends on the angle by which the scintillator is seen by the camera. This effect was specifically studied in a dedicated experiment, that was realised by keeping the source and the camera fixed and rotating the scintillator with respect to the camera. The study was performed for angles in the range of $0° - 80°$, however, in the prototype setup the maximum angle by which the camera sees a scintillator in the calorimeter is 17°.

Results of this study (shown in Fig. 6.2) show a dependence of the pixel value on the angle, that only becomes significant for angles larger than 20°. Therefore, it was decided that there is no need to apply a correction factor for the angle by which the camera sees individual scintillators for the spectrometer prototype (given the maximum angle in this case is 17°).

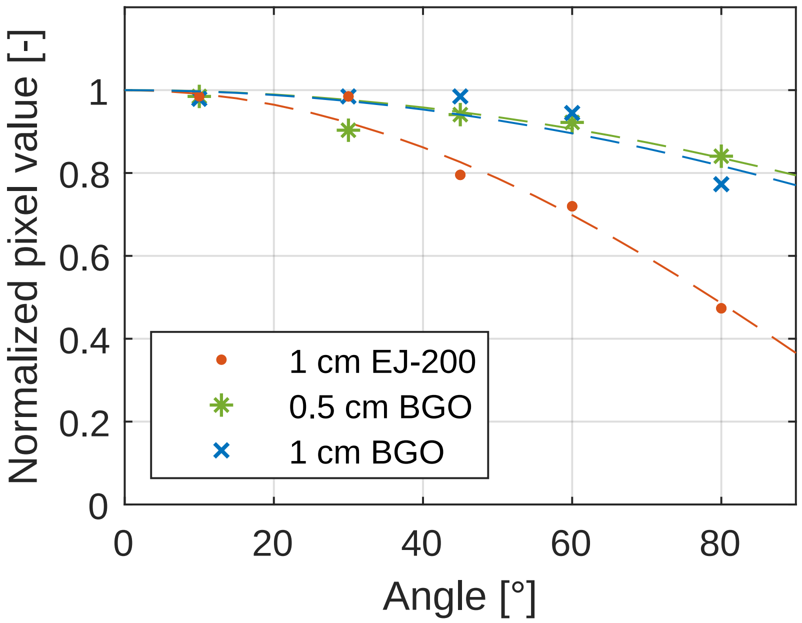

Fig. 6.2: Dependence of the normalised average pixel value in ROI (to the average pixel value in ROI at 0°) on the angle, by which the scintillator is rotated. In the case of large angles (close to 90°), it is impossible to avoid adding the bright line into the ROI, which is why the measurement was not done at this angle. The errorbars are not visible due to the large number of pixels in the ROI.

6.2 Validation

The principal experiment of the spectrometer development is its validation (the proof of concept of the whole spectrometer and its function). Moreover, this experiment was also dedicated to estimating the overall uncertainties and limitations of the spectrometer. The validation was performed at the Czech National Institute for Radiation Protection (SÚRO) [81] using the OG-8 irradiator by VF Nuclear, namely with the Cs-137 and Co-60 radioactive sources. This irradiator provides a high flux of photons so that a sufficient amount of scintillation light can be detected using the camera for the dose-depth curve measurement. The Cs-137 provides a single γ line to be determined by the spectrometer, the Co-60 instead provides two close γ lines and thus represents a greater challenge for the spectrometer.

The calorimeter was aligned with the centre of the beam using a laser cross. The experimental setup can be seen in Fig. 6.3. The image of calorimeter as seen by the camera is shown in Fig. 6.4. In Both these figures the optical shielding is not present, however, during the irradiation the whole setup was insulated from ambient light using a black aluminium foil. Moreover, the lights inside the laboratory were turned off during the irradiation.

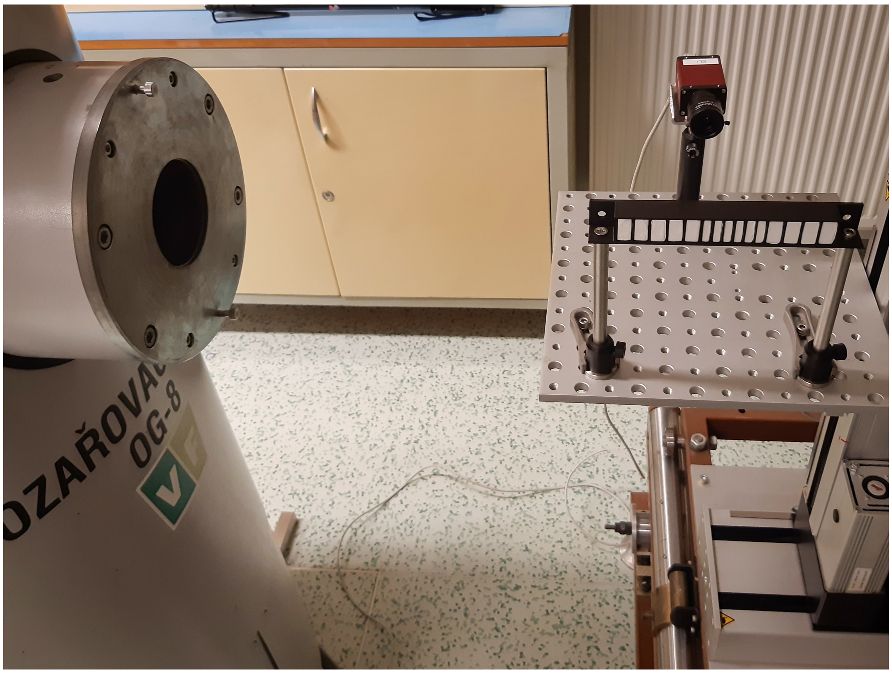

Fig. 6.3: Experimental setup for the energy calibration of the spectrometer. The irradiator is situated in the left. The image was taken prior to installation of the optical shielding.

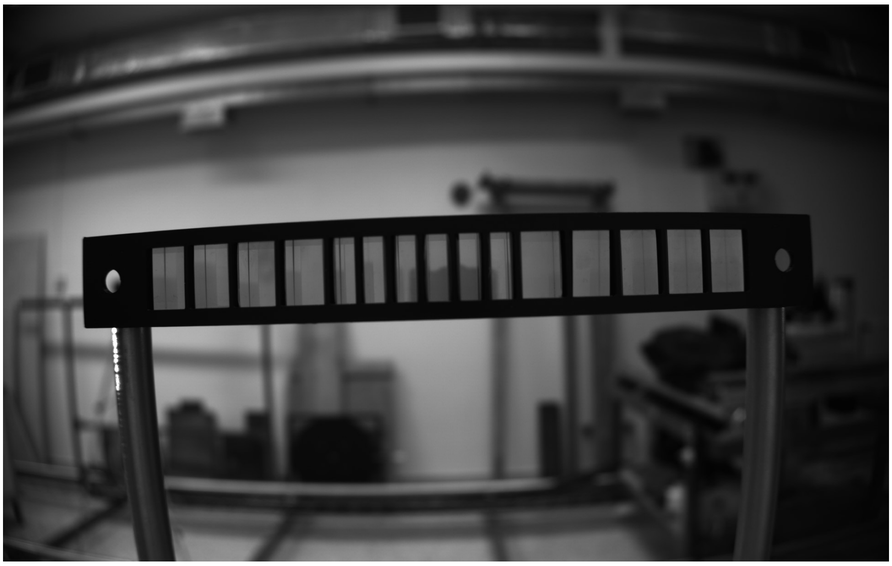

Fig. 6.4: Image of the calorimeter taken prior to irradiation. The image was taken prior to installation of the optical shielding.

6.2.1 Cs-137 irradiation

The raw image taken during irradiation using the Cs-137 source (661.7 keV) is shown in Fig. 6.5, the rotated image (so that the scintillators are aligned with the image axes) with highlighted manually selected ROIs is shown in Fig. 6.6. This image was taken with fine-tuned exposition parameters – the exposition time was set to 1000 ms, and the gain was set to 30 db.

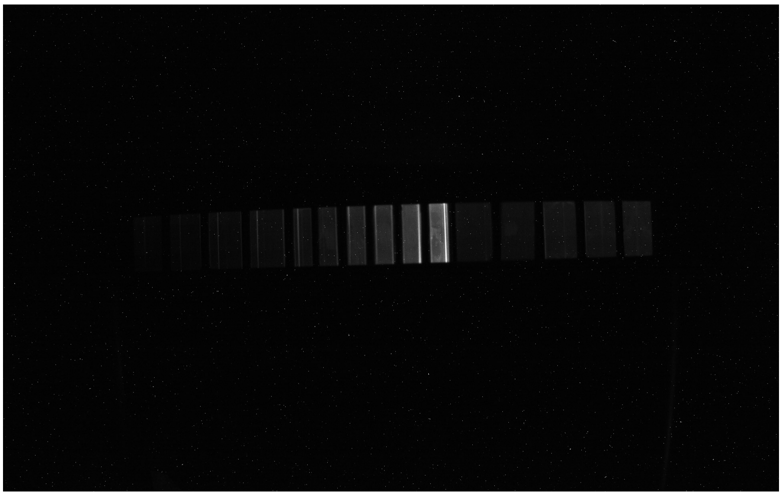

Fig. 6.5: Raw image taken by the camera during the Cs-137 irradiation.

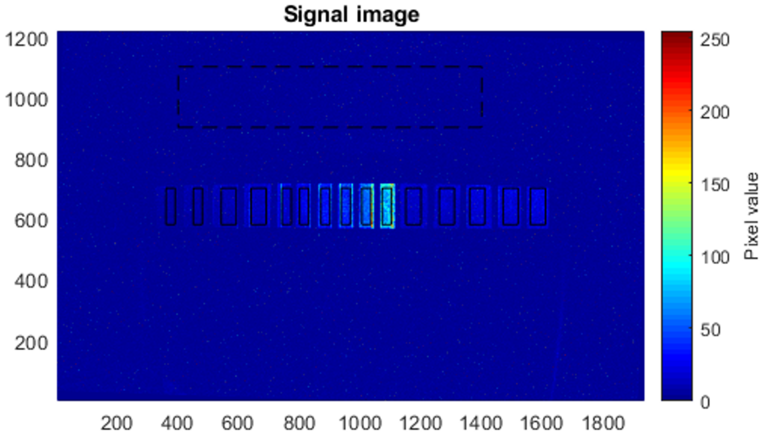

Fig. 6.6: Processed image taken during the Cs-137 irradiation, the ROIs together with background ROI (top of the picture) are shown.

This image was processed using the developed software, correction factors for each individual scintillator (as evaluated from the calibration of individual scintillators) were applied, resulting in corrected mean pixel values as shown in Fig. 6.7. The experimental value errorbars in this plot represent the standard deviation of the pixel values calculated as

$$S = \sqrt{\frac{1}{N-1}\sum_{i=1}^{N}(pv_i - \overline{pv})^2}, \tag{6.1}$$

where N is the number of pixels inside the ROI and pv_i is the pixel value of pixel i. Therefore, the errorbars in this figure do not represent the standard error of the mean pixel value, because this value is very low (because of the large number of pixels within the ROI) and thus the errorbars would not be visible.

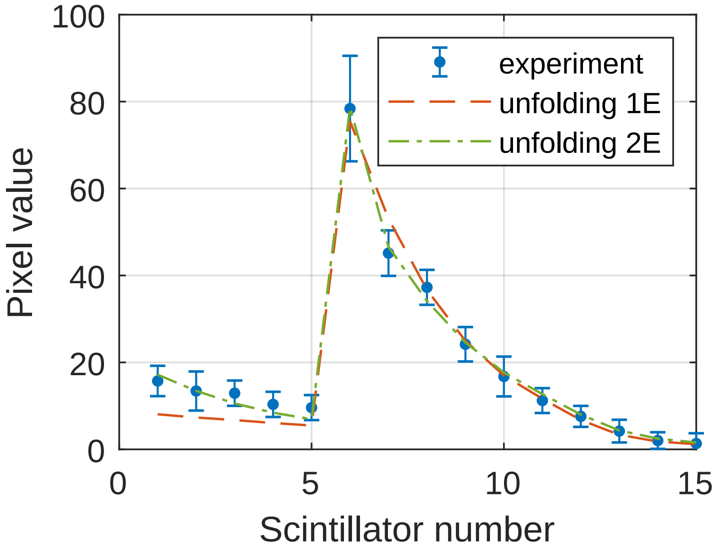

Fig. 6.7: Measured dose-depth curve (in terms of scintillation light) when exposed to the radiation of the Cs-137 irradiatior, corrections discussed in section 6.1.1 are implemented. The red line represents a simulated signal for the 1 energy unfolding, the green line represents a simulated signal composed of 2 energies identified by the unfolding when set to search for 2 energies.

1 energy unfolding

The unfolding algorithm, was firstly set to search for 1 monochromatic energy, providing a result of

$$E = 570 \pm 40\,\mathrm{keV}, \quad R^2_{adj} = 0.955. \tag{6.2}$$

Notice that the value of R^2_{adj}, the adjusted coefficient of determination, is close to 1, indicating a good agreement between simulated and measured values. The standard error of the energy evaluated as given by the non-linear model can be used as an estimate of the detector uncertainty, as it corresponds to 1 σ resolution. Nevertheless, it is clear that the spectrometer was not able to accurately determine the energy of gamma radiation produced by the Cs-137 source, indicating a need to search for more energies.

2 energies unfolding

When set to search for 2 energies, the unfolding reached a higher value of R^2_{adj}, indicating a better agreement with the measured values, the determined radiation energies were

$$E_1 = 24 \pm 1\,\mathrm{keV}, \quad E_2 = 660 \pm 40\,\mathrm{keV}, \quad R^2_{adj} = 0.993, \tag{6.3}$$

Simulated dose-depth curve for unfolded energies is also shown in Fig. 6.7 (green curve).

In this case the spectrometer was able to determine the γ line of Cs-137 more precisely than in the case of search for one energy, while also indicating a presence of a low energy component. The relative uncertainty of the spectrometer can be estimated as 6 %, using the estimation of the standard error of the unfolded energy (uncertainty estimations for similar devices are not available in literature as of writing this thesis).

The low energy component of 24 keV could be caused by multiple factors or even their combination. The Cs-137 beside the main γ line also produces low-energy X-rays (32 keV), stray radiation can also be produced as a result of scattering within the irradiatior shielding. Such background produced by scattering is clearly not monochromatic, moreover it would be difficult to determine its spectrum and describe it using only several parameter. Given that, the result of 24 keV line can be only considered as an indication of presence of low-energy background.

6.2.2 Co-60 irradiation

The change to the Co-60 source was performed using the irradiator system, thus all other parameters (experiment configuration) remained consistent with the Cs-137 irradiation. The raw image when exposed to the radiation from a Co-60 source (1173.2 keV and 1332.5 keV) is shown in shown in Fig. 6.8

1 energy unfolding

The corrected mean pixel values after the image processing are shown in Fig. 6.9. As in the previous case, the errorbars represent the standard deviation of the pixel values, not the standard mean error. The unfolding algorithm, when set to search for 1 energy gives a result of

$$E = 960 \pm 160\,\mathrm{keV}, \quad R^2_{adj} = 0.884. \tag{6.4}$$

As in the Cs-137 experiment, it is evident that a search for more energies is needed, moreover, the value of R^2_{adj} is rather low, indicating insufficient agreement between the model and the measured signal.

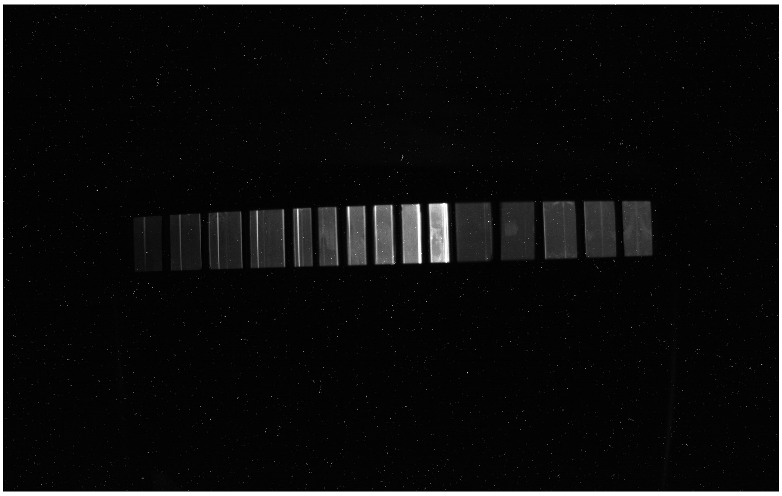

Fig. 6.8: Image taken during the Co-60 irradiation, the exposition time is 1000 ms, the gain is set to 30 db (same as during Cs-137 irradiation).

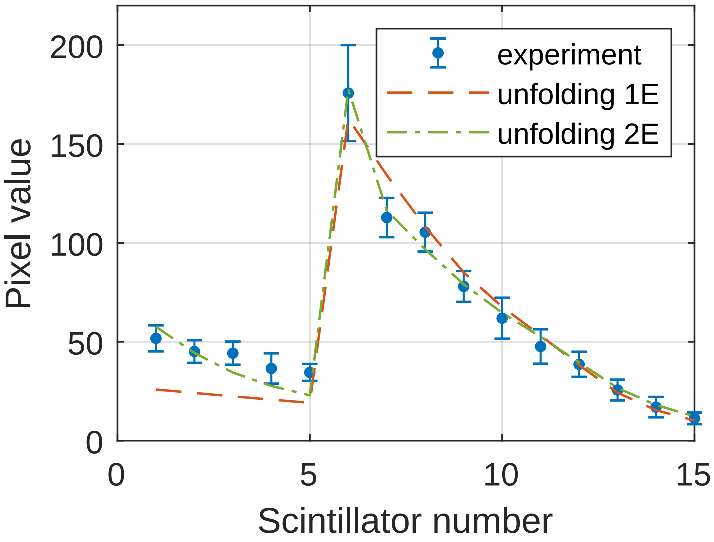

Fig. 6.9: Calorimeter signal when exposed to the radiation of Co-60 irradiator, corrections discussed in section 6.1.1 are implemented. The red line represents a simulated signal for the 1 energy unfolding, the green line represents a simulated signal composed of 2 energies identified by the unfolding when set to search for 2 energies.

2 energies unfolding

When the unfolding algorithm was set to search for 2 energies, it reached a higher R^2_{adj} value, giving

$$E_1 = 23 \pm 1\,\mathrm{keV}, E_2 = 1160 \pm 130\,\mathrm{keV}, \quad R^2_{adj} = 0.977. \tag{6.5}$$

In this case when searching for two γ lines of the source, the unfolding returned a value of 1160 keV with an uncertainty of 10 %. Given this value, it can be concluded that the unfolding is unable to resolve the two γ lines of the Co-60 source and instead treats them as one. As in previous case, there is also a low-energy component, likely caused by the scattered radiation background. As in the previous case, the energy value is only an indication of presence of a background.

A test to search for 3 spectra components using the unfolding algorithm was also performed. however, it did not return any other component then the ones found during the search for 2 components.

6.3 Calibration and validation summary

The calibration of the individual scintillators revealed that while the EJ-200 scintillators had a very similar response, the response of BGO scintillators was different and thus a correction factor was applied. The calibration of the angle revealed that no correction is needed given the angles of view in the spectrometer prototype.

The validation experiment revealed than when set to search for two energies, the spectrometer was able to determine the energy of the γ radiation of the Cs-137 source with a relative uncertainty of 6 %. Instead, for the Co-60 source, the spectrometer provided one value for the two γ lines, being unable to distinguish the two even when set to search for more energies.

This experiment has thus validated that the spectrometer is functional and can determine the energy of impinging radiation. A test of the spectrometer in a laser-generated radiation environment is described in the next chapter.

Chapter 7

Tests at ELIMAIA beamline

Given the successful validation of the spectrometer using conventional sources, the next step was a data-taking using a laser-driven radiation source. This experiment was performed during the commissioning of the ELIMAIA beamline using the L3 HAPLS laser system. The author of this thesis contributed to this experiment as a consultant, mainly in the preparatory stages of the experiment.

7.1 New segmentation

In preparation for this experiment, more studies regarding the segmentation have been carried out by the development team (with the author of this thesis providing consultations in the early stages). The goal of these studies was to further improve the spectrometer design for the data-taking at ELIMAIA beamline, resulting in an updated segmentation.

The updated segmentation comprises 21 scintillators of lower thickness than in the case of validation experiments, while keeping the design of frontal EJ-200 part followed by the BGO part. Detailed configuration can be seen in Tab. 7.1. Also, two 10 mm thick lead absorbers were added to the design to attenuate the high-energy part of the radiation spectrum. Beside the segmentation update, the overall shielding from ambient light was changed using a dedicated light-proof box instead of aluminium foil. Other components of the spectrometer remained as described in the previous chapters. [82]

Scintillator no. [–]	1	2	3	4	5	6	7	8	9	10	11	12	13	14	15	16	17	18	19	20	21
Thickness [mm]	3	3	3	10	10	10	2	2	2	2	2	3	3	3	3	5	5	5	10	10	10

Tab. 7.1: The segmentation of the spectrometers used during the ELIMAIA commissioning. Values in blue show the length of a EJ-200 scintillator (in millimetres), while the values in green show the length of a BGO scintillator. The lead absorbers are placed between scintillators 19 and 20 and between 20 and 21. [82]

7.2 Experimental setup

The experiment was carried out during the commissioning of the ELIMAIA beamline, using the L3 HAPLS laser system at laser intensity approximately $I = 10^{21}$ W/cm^2, the laser pulse power being approximately 0.3 PW. During this experiment, most of the shots were carried out in a single-shot regime. Two identical spectrometers were placed outside the experimental chambers behind the glass viewports in order to minimise the shielding effect of the experimental chamber walls. First spectrometer was placed in the forward direction of the beam (forward stack), the second was placed above the interaction point (top stack). The spectrometer placed in the direction of the beam was shielded from electron radiation using magnetic fields (0.4 T). The experimental setup can be seen in Fig. 7.1. [82]

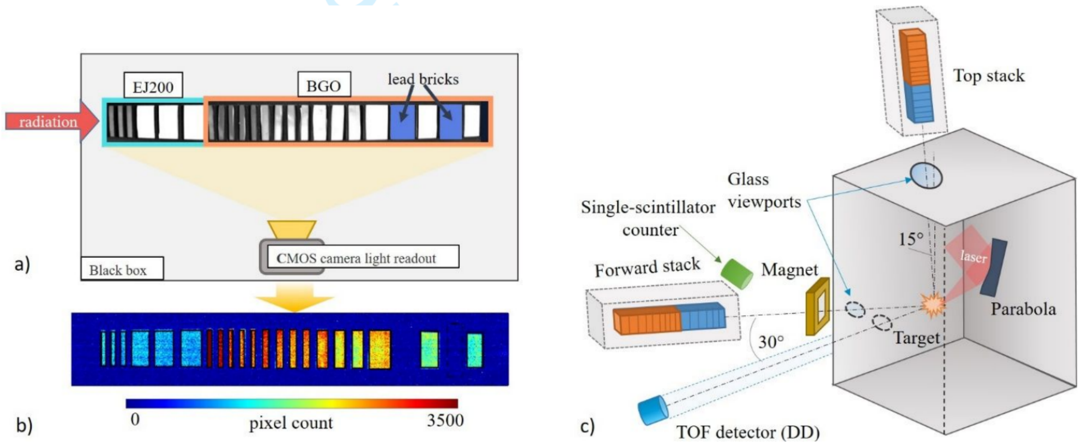

Fig. 7.1: Experimental setup of the spectrometers during commissioning of the ELIMAIA beamline. [82]

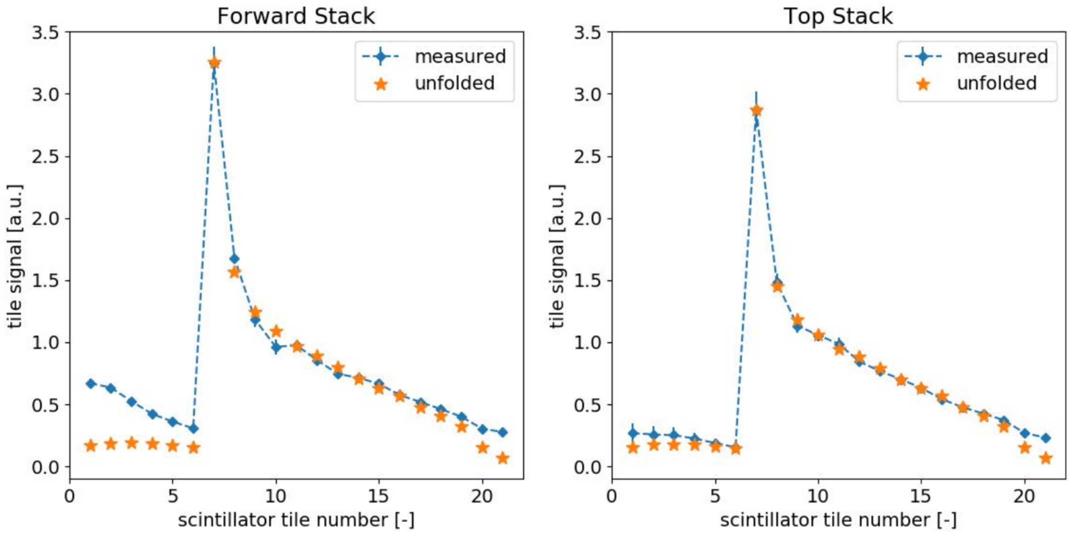

Fig. 7.2: Example of a spectrometer signal compared with the unfolded signal from one shot taken during the ELIMAIA commissioning. [82]

7.3 Results

An example of acquired data compared with the unfolded signal is shown in Fig. 7.2. As can be seen in this figure, more radiation was detected in the forward direction of the beam than in the case of the top one. This is in agreement with the information provided in section 2.2.2. As for the unfolded temperatures, they are almost identical. These results are also in agreement with theoretical expectations, as there should not be a dependence of high energy X-ray temperature on the angle from the beam axis (see Fig. 2.8).

Another phenomenon that can be seen in the forward stack is a difference between the measured and unfolded dose-depth curve in the frontal part of the calorimeter. This is probably caused by electrons accelerated in the direction of the beam, producing secondary radiation when interacting with other beamline components. Therefore, for this spectrometer, the data from the plastic scintillators in the frontal part were not used for the unfolding. Results of the unfolding are shown in Tab. 7.2.

	T_1 [keV]	T_2 [keV]	$N_2/N_1[-]$
Forward stack	80 ± 6	2400 ± 110	0.33 ± 0.10
Top stack	70 ± 3	2450 ± 60	0.19 ± 0.10

Tab. 7.2: Example of unfolding results for the dose-depth curves show in Fig. 7.2. T_1 is the low Maxwellian temperature, T_2 the high Maxwellian temperature, and N_2/N_1 is the ratio of amplitudes of the two radiation components.

Throughout the commissioning, each shot was analysed in the same fashion, the forward stack provided values of the high Maxwellian temperature mostly in the range of 2.1 – 2.4 MeV, the top stack mostly in the range of 1.7 – 2.3 MeV. These values are in good agreement with Beg's scaling laws, that for the given laser configuration predict electron temperature in the range of 1.5 – 3.0 MeV. The typical measured values of low Maxwellian temperature were in the range of 60 keV – 85 keV. [82]

This experiment thus proved that the developed spectrometer can be used for spectrometry of laser-generated X-ray radiation. The relative errors of the unfolded temperatures determined by the unfolding software are typically below 10 %.

Chapter 8

Improvement tests and future outlooks

The effort following the spectrometer validation focused on improving the response matrix, in order to be able to distinguish the two γ lines of the Co-60 source. Multiple techniques were investigated, including a direct simulation of scintillation light. Additionally, more possible future improvements are described in this chapter.

8.1 Response matrix improvement

As described in previous chapters, the response matrix is created using a set of simulation results for a set of beam energies/temperatures, the values of beam energies/temperatures not directly present in the response matrix must be calculated using an interpolation). Therefore, one possible option of improving the spectrometer accuracy is to increase the number of energies/temperatures in the response matrix by means of performing and evaluating a larger set of FLUKA simulations.

Also, the quantity within the response matrix is the energy deposition inside scintillators, which is not exactly the measured quantity (light collected by the camera), The second option of improving the response matrix is therefore to exchange the scored quantity directly to the amount of scintillation light that would reach the camera.

8.1.1 More dense response matrix

In order to determine whether increasing the number of simulations would aid in enhancing the spectrometer resolution, simulations were performed with a step of 5 keV for the full energy range (5 keV to 1500 keV). Moreover, these simulations were executed using a large number of beam particles (primaries), resulting in negligible statistical uncertainties of the simulation results. However, when this response matrix was applied to the evaluation of dose-depth curves acquired during the calibration using the Co-60 source, there was no improvement in determining its two γ lines (the results were identical as presented in the validation experiment), nor any other improvement was observed. Therefore, a more sophisticated method was investigated – a direct simulation of scintillation light using FLUKA.

8.1.2 Optical simulations

As FLUKA allows simulation of both production and transport of scintillation light, the following attempts of improving the response matrix focused on determining, whether it would be possible to approximate the picture taken by camera using FLUKA simulations and whether this would allow constructing a response matrix not in terms of deposited energy, but rather the relative pixel values in ROIs.

For this set of simulations, the production of optical photons within the scintillators was defined using the OPT-PROD [83] cards. The scintillator and scintillation light properties were set according to the information in Tab. 3.1. Similarly, optical properties (absorption coefficient, refraction index, reflectivity) of all materials present within the simulation geometry were defined using the OPT-PROP [84] cards. Using these setting, the scintillation photons are simulated as secondary particles emerging from the dose deposition inside the scintillators.

As the geometry of the lens and the camera is complicated, it was approximated using a pinhole within an perfectly absorbent body. The CMOS chip was simulated using a 2D USRBIN scoring of optical photons. A comparison of a simulated image and a real image taken by the camera is shown in Fig. 8.1, showing a remarkable similarity between the simulation and the image acquired during the experiment.

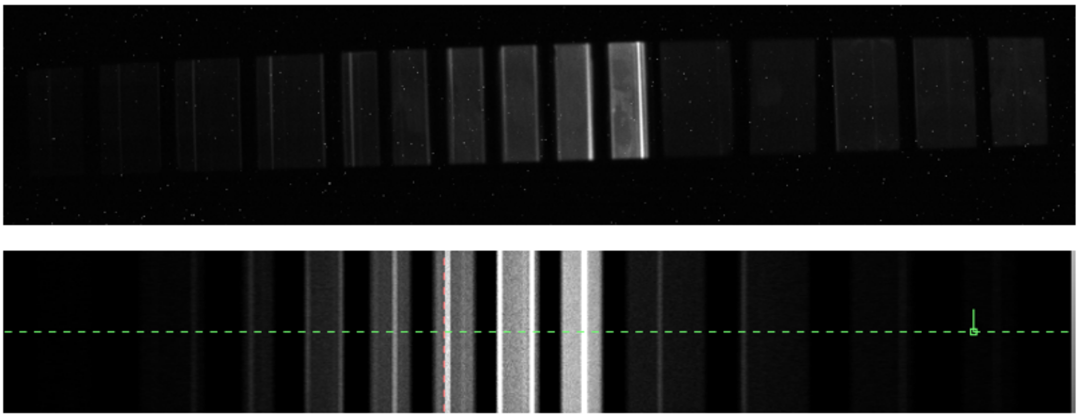

Fig. 8.1: Comparison of image taken by camera during the energy calibration (top) and a simulated image using FLUKA using optical photon simulation (bottom). Notice that the lines produced by the corner effect are visible in both images.

8.1.3 Optical response matrix

As the next step, a set of simulations was performed to obtain simulated camera images for the energy range of 5 keV – 1500 keV with a step of 5 keV. The resulting images were then processed to get the relative pixel values in ROIs – to get average pixel values outside bright areas for each scintillator, forming a response matrix. However, when this response matrix was applied to the unfolding of the calibration data, there was no improvement in determining the energy of radioactive sources on the images acquired during the calibration (almost identical results were obtained as in the validation experiment, $E_1 = 24$ keV, $E_2 = 1150$ keV).

It should also be noted that these simulations require a significant amount of computation resources, due to the low probability of scintillation photons reaching the pinhole representing the camera. Therefore, these simulations have been performed over several weeks using the ELI Beamlines high performance computing cluster ECLIPSE. This issue could be resolved by properly modelling the lens and the chip of the camera, but this task was abandoned due to its complexity.

Nevertheless, the optical simulations allowed to model and explain several phenomenons seen in the experimental data, such as the corner effect and allow to model the picture seen by camera in different conditions (position, distance from the calorimeter), providing insights for possible future spectrometer design.

8.2 Future outlooks

While the developed spectrometer was proven to be capable of performing spectrometry of laser-generated radiation, multiple components of the spectrometer can be further upgraded.

8.2.1 Scintillators

As one of the most important feature of the scintillators used in the developed spectrometer is the light yield, it is envisioned to investigate a possible usage of novel scintillating materials that provide high light yield. Also, it was discovered that it is not beneficial to have all of the scintillator sides polished, but rather have all sides but the front one finely diffused in order to maximise light collection using the optical detector. Moreover, this modification would likely remove the bright areas caused by the corner effect.

8.2.2 Readout

As a large number of uncertainties is caused by the CMOS camera readout (e.g. corner effect, noise) other readout methods (e.g. photodiodes and SiPMs) were considered. It is envisioned that a spectrometer with electronic readout will be built and its performance would be compared to the one with CMOS camera readout.

8.2.3 Software

As of writing this thesis, the spectrometer software is decoupled into the controls of the camera and the image processing and unfolding. In order to simplify the online usage of the spectrometer, it would be beneficial to have a unified software that provides both controls of the readout and the subsequent processing.

However, as the readout is also subject to enhancement, the software upgrade is envisioned only after the readout enhancement is finished. Moreover, the unfolding algorithm itself might be improved by exploiting advanced methods (e.g. machine learning algorithms).

8.2.4 Proton spectrometry adaptation

While the spectrometer designed in the frame of this thesis was designed for X-ray spectrometry, it is easy to adapt its design to perform proton spectrometry. Traditionally, proton spectrometry at laser-plasma beamlines was performed using stacks of radiochromic films, however, as these detectors are passive, it was impossible to use them in high-repetition rate environments.

A modified version of the spectrometer (see 8.2) was developed by the ELI Beamlines team (the author of this thesis being a consultant) and tested at the U-120 M Cyclotron at the Nuclear Physics Institute of the Czech Academy of Sciences at Řež, using a proton beam of 33 MeV. The modified version of the spectrometer was able to determine this energy and showed a very good agreement with the traditional passive stack detector. It is therefore envisioned to use this detector as a monitoring instrument at the ELIMAIA beamline [85].

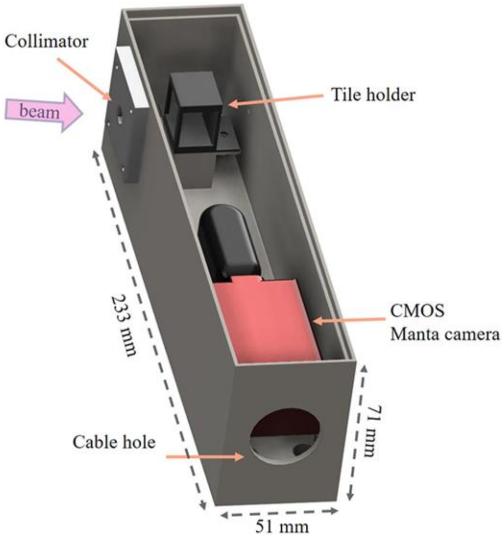

Fig. 8.2: Adaptation of the spectrometer for the proton spectrometer. The scintillators are placed in the small tile holder, the whole setup is enclosed in optical shielding. [85]

Conclusion

Laser-generated X-ray radiation can vary in its energy depending on multiple factors, one of the main ones is the laser intensity. With increasing laser intensity, the X-ray radiation also increases, reaching energies up to 100 MeV with current laser systems. Spectrometry of laser-generated X-ray radiation is difficult due to its pulsed nature and thus standard methods cannot be applied. However, there are several options that can be used, one of them is the analysis of the dose-depth curve.

The spectrometer developed in the scope of this thesis is based on such analysis. It consists of a scintillator stack placed inside a dedicated holder. The optical readout is performed by a CMOS camera. The measured dose-depth curve is then compared with a response matrix generated by FLUKA simulations and parameters of the spectrum are evaluated using an unfolding software. Therefore, this system is able to provide several parameters describing the spectrum.

Hardware of the developed system was fine-tuned using simulations and experiments, regarding the number of scintillators and their thicknesses, however, the configuration can be altered for different experiments. The camera of choice became the Allied Vision Manta G-235B, that proved to be cost-effective, compact, sensitive, and simple to use. A reflector was applied to the scintillators in the form of 0.5 mm PTFE. Scintillators were separated by a 1 mm layer of black PLA.

The software consists of FLUKA for simulating response matrix of a given configuration, simulations were adapted to be run in parallel to cover a wide range of energies. The camera is controlled by Vimba Viewer, which serves to set the camera parameters (e.g. exposition time, trigger type) and to acquire images. Results are then processed using Matlab, where the spectrum parameters are evaluated using non-linear modelling. This method allows to estimate the standard errors of the evaluated parameters.

The whole system was calibrated using radioactive sources, each single scintillator was calibrated in order to evaluate correction factors for different responses caused by the manufacturing process or differences in application of the reflector. Then a validation experiment showed that the system is able to evaluate energy of impinging radiation with an uncertainty of approximately 10%.

The validation of the spectrometer and subsequent experiment at ELIMAIA beamline commissioning demonstrated that the developed system represents a functional spectrometer of photons in pulsed laser-generated radiation fields. There are multiple possible options of improving the spectrometer performance, that are planned to be investigated during further development of the spectrometer.

Bibliography

[1] C. Rulliere, ed., *Femtosecond Laser Pulses.* Advanced Texts in Physics, Springer Science+Business Media, 2 ed., Jan. 2005.

[2] R. Schoenlein, T. Elsaesser, K. Holldack, Z. Huang, H. Kapteyn, M. Murnane, and M. Woerner, "Recent advances in ultrafast x-ray sources," *Philosophical Transactions of the Royal Society A: Mathematical, Physical and Engineering Sciences*, vol. 377, p. 20180384, Apr. 2019.

[3] F. Dausinger, *Femtosecond technology for technical and medical applications.* Berlin: Springer, 2004.

[4] D. e. a. Von Der Linde, "Generation and application of ultrashort x-ray pulses," *Laser and Particle Beams*, vol. 19, no. 1, p. 15–22, 2001.

[5] H. Fiedorowicz, A. Bartnik, P. Wachulak, R. Jarocki, J. Kostecki, M. Szczurek, I. Ahad, T. Fok, A. Szczurek, and L. Wegrzynski, *Application of Laser Plasma Sources of Soft X-rays and Extreme Ultraviolet (EUV) in Imaging, Processing Materials and Photoionization Studies*, vol. 169, pp. 369–377. 01 2016.

[6] T. J. A. Wolf, R. H. Myhre, J. P. Cryan, S. Coriani, R. J. Squibb, A. Battistoni, N. Berrah, C. Bostedt, P. Bucksbaum, G. Coslovich, R. Feifel, K. J. Gaffney, J. Grilj, T. J. Martinez, S. Miyabe, S. P. Moeller, M. Mucke, A. Natan, R. Obaid, T. Osipov, O. Plekan, S. Wang, H. Koch, and M. Gühr, "Probing ultrafast internal conversion in organic chromophores via k-edge resonant absorption," *Nature Communications*, vol. 8, June 2017.

[7] I. Grguraš, A. R. Maier, C. Behrens, T. Mazza, T. J. Kelly, P. Radcliffe, S. Düsterer, A. K. Kazansky, N. M. Kabachnik, T. Tschentscher, J. T. Costello, M. Meyer, M. C. Hoffmann, H. Schlarb, and A. L. Cavalieri, "Ultrafast x-ray pulse characterization at free-electron lasers," *Nature Photonics*, vol. 6, p. 852–857, Nov. 2012.

[8] K. Ta Phuoc, A. Rousse, M. Pittman, J. P. Rousseau, V. Malka, S. Fritzler, D. Umstadter, and D. Hulin, "X-ray radiation from nonlinear thomson scattering of an intense femtosecond laser on relativistic electrons in a helium plasma," *Physical Review Letters*, vol. 91, Nov. 2003.

[9] R. Brown and D. Cockerill, “Electromagnetic calorimetry,” *Nuclear Instruments and Methods in Physics Research Section A: Accelerators, Spectrometers, Detectors and Associated Equipment*, vol. 666, p. 47–79, Feb. 2012.

[10] G. Battistoni, T. Boehlen, F. Cerutti, P. Chin, L. Esposito, A. Fassò, A. Ferrari, A. Lechner, A. Empl, A. Mairani, A. Mereghetti, P. G. Ortega, J. Ranft, S. Roesler, P. Sala, V. Vlachoudis, and G. Smirnov, “Overview of the FLUKA code,” *Annals of Nuclear Energy*, vol. 82, pp. 10–18, 2015.

[11] C. Ahdida, D. Bozzato, D. Calzolari, F. Cerutti, N. Charitonidis, A. Cimmino, A. Coronetti, G. L. D’Alessandro, A. Donadon Servelle, L. S. Esposito, R. Froeschl, R. García Alía, A. Gerbershagen, S. Gilardoni, D. Horváth, G. Hugo, A. Infantino, V. Kouskoura, A. Lechner, B. Lefebvre, G. Lerner, M. Magistris, A. Manousos, G. Moryc, F. Ogallar Ruiz, F. Pozzi, D. Prelipcean, S. Roesler, R. Rossi, M. Sabaté Gilarte, F. Salvat Pujol, P. Schoofs, V. Stránský, C. Theis, A. Tsinganis, R. Versaci, V. Vlachoudis, A. Waets, and M. Widorski, “New capabilities of the fluka multi-purpose code,” *Frontiers in Physics*, vol. 9, Jan. 2022.

[12] M. Aléonard, M. Altarelli, P. Antici, A. Apolonskiy, P. Audebert, A. Bartnik, C. Barty, A. Bernstein, J. Biegert, P. Böni, N. Booth, D. Bote, S. Bulanov, R. Butkus, L. Cardoso, J. Chambaret, D. Charambilidis, G. Cheriaux, R. Clarke, and M. Zepf, *WHITEBOOK ELI – Extreme Light Infrastructure; Science and Technology with Ultra-Intense Lasers.* 01 2011.

[13] “ELI-ERIC.” `https://eli-laser.eu/organisation/eli-eric`. [Accessed 19-04-2024].

[14] V. Istokskaia, V. Stránský, L. Giuffrida, R. Versaci, F. Grepl, M. Tryus, A. Velyhan, R. Dudžák, J. Krása, M. Krupka, S. Singh, D. Neely, V. Olšovcová, and D. Margarone, “Experimental tests and signal unfolding of a scintillator calorimeter for laser-plasma characterization,” *Journal of Instrumentation*, vol. 16, p. T02006–T02006, Feb. 2021.

[15] V. Istokskaia, V. Stránský, L. Giuffrida, R. Versaci, V. Olšovcová, S. Singh, M. Krupka, R. Dudžák, J. Krása, and D. Margarone, “Online measurements of gamma radiation from laser-plasma and signal unfolding using a scintillator calorimeter,” in *Laser Acceleration of Electrons, Protons, and Ions VI* (S. S. Bulanov, C. B. Schroeder, and J. Schreiber, eds.), SPIE, Apr. 2021.

[16] V. Stránský, V. Istokskaia, R. Versaci, L. Giuffrida, A. Cimmino, D. Margarone, and V. Olšovcová, “Development, optimization, and calibration of an active electromagnetic calorimeter for pulsed radiation spectrometry,” *Journal of Instrumentation*, vol. 16, p. P08060, Aug. 2021.

[17] V. Istokskaia, B. Lefebvre, V. Stránský, L. Giuffrida, R. Versaci, V. Olšovcová, and D. Margarone, “Hard x-rays measurements using a scintillator-array calorimeter in high-intensity laser-plasma experiments,” in *Hard X-Ray, Gamma-Ray, and Neutron Detector Physics XXIV* (N. J. Cherepy,

M. Fiederle, and R. B. James, eds.), vol. 12241, p. 122410F, International Society for Optics and Photonics, SPIE, 2022.

[18] I. P. Office, "PUV2020-37719, Segmented Calorimeter." `https://isdv.upv.gov.cz/webapp/resdb.print_detail.det?pspis=PUV/37719&plang=EN`, 2021.

[19] "ELI Beamlines – Dolní Břežany." `https://www.eli-beams.eu/`. (Accessed on 08/08/2021).

[20] B. L. Garrec, S. Sebban, D. Margarone, M. Precek, S. Weber, O. Klimo, G. Korn, and B. Rus, "ELI-beamlines: extreme light infrastructure science and technology with ultra-intense lasers," in *High Energy/Average Power Lasers and Intense Beam Applications VII* (S. J. Davis, M. C. Heaven, and J. T. Schriempf, eds.), vol. 8962, p. 89620I, International Society for Optics and Photonics, SPIE, 2014.

[21] ELI Beamlines, The Czech Academy of Sciences, "ELI Beamllines Strategic Development Plan." `https://www.eli-beams.eu/wp-content/uploads/2018/08/ELI_BL_Strategic-development-plan_2018-2024.pdf`, November 2017.

[22] R. Antipenkov, J. Novák, J. Green, J. Cupal, P. Trojek, B. Plötzeneder, P. Bakule, D. Kramer, D. Margarone, J. Andreasson, *et al.*, "Advanced laser systems at the extreme light infrastructure beamlines facility," *Optics, Photonics and Lasers*, p. 13, 2023.

[23] D. Strickland and G. Mourou, "Compression of amplified chirped optical pulses," *Optics Communications*, vol. 56, pp. 219–221, dec 1985.

[24] P. Bakule, R. Antipenkov, J. Novák, F. Batysta, R. Boge, J. T. Green, Z. Hubka, M. Greco, L. Indra, A. Špaček, J. A. Naylon, K. Majer, P. Mazůrek, E. Erdman, V. Šobr, B. Tykalewicz, T. Mazanec, P. Strkula, and B. Rus, "Readiness of l1 allegra laser system for user operation at eli beamlines," in *OSA High-brightness Sources and Light-driven Interactions Congress 2020 (EUVXRAY, HILAS, MICS)*, p. HF1B.7, Optica Publishing Group, 2020.

[25] R. Antipenkov, J. Novák, E. C. Erdman, R. Boge, W. J. Szuba, B. Tykalewicz, P. Mazurek, C. Lazzarini, G. Grittani, P. Bakule, and B. Rus, "L1 allegra laser at ELI beamlines facility as a driver for electron acceleration at 1 khz repetition rate (conference presentation)," in *High-power, High-energy Lasers and Ultrafast Optical Technologies* (C. L. Haefner, P. Bakule, J. Hein, and T. J. Butcher, eds.), SPIE, June 2023.

[26] J. T. Green, J. Bartoníček, L. Indra, M. Fibrich, J. Eisenschreiber, J. Novák, K. Majer, B. Tykalewicz, and B. Rus, "Development of the l2-duha high repetition rate, 100 tw opcpa system for laser wakefield acceleration," in *Laser Congress 2023 (ASSL, LAC)*, p. AM3A.5, Optica Publishing Group, 2023.

[27] J. T. Green, “LASER L2 DUHA, ELI Beamlines.” `https://www.eli-beams.eu/facility/lasers/laser-2-amos-1-pw-20-j-10-hz/`, 2013. [Accessed 05-08-2024].

[28] E. Sistrunk, T. Spinka, A. Bayramian, S. Betts, R. Bopp, S. Buck, K. Charron, J. Cupal, R. Deri, M. Drouin, A. Erlandson, E. S. Fulkerson, J. Horner, J. Horacek, J. Jarboe, K. Kasl, D. Kim, E. Koh, L. Koubikova, R. Lanning, W. Maranville, C. Marshall, D. Mason, J. Menapace, P. Miller, P. Mazurek, A. Naylon, J. Novak, D. Peceli, P. Rosso, K. Schaffers, D. Smith, J. Stanley, R. Steele, S. Telford, J. Thoma, D. VanBlarcom, J. Weiss, P. Wegner, B. Rus, and C. Haefner, “All diode-pumped, high-repetition-rate advanced petawatt laser system (hapls),” in *Conference on Lasers and Electro-Optics*, CLEO_SI, OSA, 2017.

[29] A. Zymaková, M. Albrecht, R. Antipenkov, A. Špaček, S. Karatodorov, O. Hort, J. Andreasson, and J. Uhlig, “First experiments with a water-jet plasma x-ray source driven by the novel high-power–high-repetition rate l1 allegra laser at eli beamlines,” *Journal of Synchrotron Radiation*, vol. 28, p. 1778–1785, Nov. 2021.

[30] J. Nejdl, D.-D. Mai, U. Chaulagain, O. HOrt, O. Finke, M. Albrecht, M. Jurkovic, R. Lera, S. Karatodorov, M. Lamač, J. Vančura, K. Boháček, S. J. Espinoza, S. Richter, M. Rebarz, E. Klimesova, M. Krikunova, M. Kolzová, R. Antipenkov, F. Batysta, J. Novák, J. T. Green, J. Andreasson, and G. Korn, “Progress on laser-driven x-ray sources at eli beamlines,” in *X-Ray Lasers and Coherent X-Ray Sources: Development and Applications XIII* (A. Klisnick and C. S. Menoni, eds.), SPIE, Sept. 2019.

[31] J. Nejdl, U. Chaulagain, D. Mai, O. Hort, M. Lamač, M. Raclavský, M. Albrecht, M. Jurkovič, O. Finke, J. Vábek, Y. Pulnova, and S. V. Bulanov, “Update on laser-driven x-ray sources at eli beamlines,” in *Optica High-brightness Sources and Light-driven Interactions Congress 2022*, p. ETh5A.6, Optica Publishing Group, 2022.

[32] M. Kozlová, K. Bohaček, V. Horný, K. Ta Phuoc, J. Nejdl, S. Sebban, J. Gautier, M. Krůs, and U. Chaulagain, “Laser-driven plasma-based incoherent x-ray sources at pals and eli beamlines,” in *X-Ray Lasers 2016* (T. Kawachi, S. V. Bulanov, H. Daido, and Y. Kato, eds.), (Cham), pp. 127–134, Springer International Publishing, 2018.

[33] N. Jourdain, U. Chaulagain, M. Havlík, D. Kramer, D. Kumar, I. Majerová, V. T. Tikhonchuk, G. Korn, and S. Weber, “The l4n laser beamline of the p3-installation: Towards high-repetition rate high-energy density physics at eli-beamlines,” *Matter and Radiation at Extremes*, vol. 6, Nov. 2020.

[34] D. Margarone, G. A. P. Cirrone, G. Cuttone, A. Amico, L. Andò, M. Borghesi, S. S. Bulanov, S. V. Bulanov, D. Chatain, A. Fajstavr, L. Giuffrida, F. Grepl, S. Kar, J. Krasa, D. Kramer, G. Larosa, R. Leanza, T. Levato, M. Maggiore,

L. Manti, G. Milluzzo, B. Odlozilik, V. Olsovcova, J.-P. Perin, J. Pipek, J. Psikal, G. Petringa, J. Ridky, F. Romano, B. Rus, A. Russo, F. Schillaci, V. Scuderi, A. Velyhan, R. Versaci, T. Wiste, M. Zakova, and G. Korn, "Elimaia: A laser-driven ion accelerator for multidisciplinary applications," *Quantum Beam Science*, vol. 2, no. 2, 2018.

[35] M. Borghesi, "Ion acceleration: Tnsa and beyond," in *Laser-Driven Sources of High Energy Particles and Radiation* (L. A. Gizzi, R. Assmann, P. Koester, and A. Giulietti, eds.), (Cham), pp. 143–164, Springer International Publishing, 2019.

[36] P. Cirrone, G. Cuttone, L. Pandola, D. Margarone, and G. Petringa, *Particles Simulation Through Matter in Medical Physics Using the Geant4 Toolkit: From Conventional to Laser-Driven Hadrontherapy*, pp. 187–208. 09 2019.

[37] A. Molodozhentsev, J. Green, J. Hawke, M. Kaur, D. Kocon, G. Korn, K. Kruchinin, and A. Maier, "Laser-driven compact free electron laser development at eli-beamlines," *Proceedings of the 39th Free Electron Laser Conference*, vol. FEL2019, p. Germany, 2019.

[38] G. Grittani, C. Lazzarini, S. Lorenz, M. Nevrkla, L. Vilanova, S. V. Bulanov, and G. Korn, "Eli-elba: fundamental science investigations with high power lasers at eli-beamlines," in *OSA High-brightness Sources and Light-driven Interactions Congress 2020 (EUVXRAY, HILAS, MICS)*, p. JM3A.20, Optica Publishing Group, 2020.

[39] T. Levato, S. Bonora, G. M. Grittani, C. M. Lazzarini, M. F. Nawaz, M. Nevrkla, L. Villanova, R. Ziano, S. Bassanese, N. Bobrova, K. Casarin, E. Chacon-Golcher, Y. Gu, D. Khikhlukha, D. Kramer, M. Lonza, D. Margarone, V. Olšovcová, M. Rosinski, B. Rus, P. Sasorov, R. Versaci, A. Zaraś-Szydłowska, S. V. Bulanov, and G. Korn, "Hell: High-energy electrons by laser light, a user-oriented experimental platform at eli beamlines," *Applied Sciences*, vol. 8, no. 9, 2018.

[40] M. Tryus, F. Grepl, T. Chagovets, A. Velyhan, L. Giuffrida, S. Stancek, V. Kantarelou, V. Istokskaia, F. Schillaci, M. Zakova, J. Psikal, M. Nevrkla, C. M. Lazzarini, G. M. Grittani, L. Goncalves, M. F. Nawaz, J. Cupal, L. Koubíkova, S. Buck, J. Weiss, D. Peceli, P. Szotkowski, K. Majer, J. A. Naylon, J. T. Green, D. Kramer, B. Rus, G. Korn, T. Levato, and D. Margarone, "TERESA target area at ELI beamlines," *Quantum Beam Science*, vol. 4, p. 37, oct 2020.

[41] W. Helml, A. R. Maier, W. Schweinberger, I. Grguraš, P. Radcliffe, G. Doumy, C. Roedig, J. Gagnon, M. Messerschmidt, S. Schorb, C. Bostedt, F. Grüner, L. F. DiMauro, D. Cubaynes, J. D. Bozek, T. Tschentscher, J. T. Costello, M. Meyer, R. Coffee, S. Düsterer, A. L. Cavalieri, and R. Kienberger, "Measuring the temporal structure of few-femtosecond free-electron laser X-ray pulses directly in the time domain," *Nature Photonics*, vol. 8, p. 950–957, Nov. 2014.

[42] L. Hudson and J. Seely, “Laser-produced x-ray sources,” *Radiation Physics and Chemistry*, vol. 79, no. 2, pp. 132–138, 2010. Special Issue on Future Directions in Atomic and Condensed Matter Research and Applications.

[43] Z. Zhang, W. Qiu, G. Zhang, D. Liu, and P. Wang, “Progress in applications of shockwave induced by short pulsed laser on surface processing,” *Optics & Laser Technology*, vol. 157, p. 108760, 2023.

[44] L. Gallmann, I. Jordan, H. J. Wörner, L. Castiglioni, M. Hengsberger, J. Osterwalder, C. A. Arrell, M. Chergui, E. Liberatore, U. Rothlisberger, and U. Keller, “Photoemission and photoionization time delays and rates,” *Structural Dynamics*, vol. 4, p. 061502, nov 2017.

[45] N. F. Farrashbandi and M. Eslami-Kalantari, “Inverse bremsstrahlung absorption in laser-fusion plasma,” *Journal of Theoretical and Applied Physics*, vol. 14, no. 3, p. 261–264, 2020.

[46] P. Gibbon, *Short pulse laser interactions with matter : an introduction.* London: Imperial College Press, 2005.

[47] M. G. Haines, M. S. Wei, F. N. Beg, and R. B. Stephens, “Hot-electron temperature and laser-light absorption in fast ignition,” *Physical Review Letters*, vol. 102, Jan. 2009.

[48] X. F. Shen, B. Qiao, A. Pukhov, S. Kar, S. P. Zhu, M. Borghesi, and X. T. He, “Scaling laws for laser-driven ion acceleration from nanometer-scale ultrathin foils,” *Phys. Rev. E*, vol. 104, p. 025210, Aug 2021.

[49] H. Legall, C. Schwanke, S. Pentzien, G. Dittmar, J. Bonse, and J. Krüger, “X-ray emission as a potential hazard during ultrashort pulse laser material processing,” *Applied Physics A*, vol. 124, may 2018.

[50] J. Seibert, “X-ray imaging physics for nuclear medicine technologists. part 1: Basic principles of x-ray production,” *Journal of nuclear medicine technology*, vol. 32, pp. 139–47, 10 2004.

[51] J. Vyskočil, E. Gelfer, and O. Klimo, “Inverse Compton scattering from solid targets irradiated by ultra-short laser pulses in the $10^{22} - 10^{23}$ W/cm^2 regime,” *Plasma Physics and Controlled Fusion*, vol. 62, p. 064002, may 2020.

[52] M. D. Wright, “Microbeam radiosurgery: An industrial perspective,” *Physica Medica*, vol. 31, pp. 601–606, sep 2015.

[53] L. Miaja-Avila, G. C. O'Neil, J. Uhlig, C. L. Cromer, M. L. Dowell, R. Jimenez, A. S. Hoover, K. L. Silverman, and J. N. Ullom, “Laser plasma x-ray source for ultrafast time-resolved x-ray absorption spectroscopy,” *Structural Dynamics*, vol. 2, p. 024301, mar 2015.

[54] M. Li, K. Huang, L. Chen, W. Yan, M. Tao, J. Zhao, Y. Ma, Y. Li, and J. Zhang, “Laser-driven powerful kHz hard x-ray source,” *Radiation Physics and Chemistry*, vol. 137, pp. 78–82, aug 2017.

[55] F. N. Beg, A. R. Bell, A. E. Dangor, C. N. Danson, A. P. Fews, M. E. Glinsky, B. A. Hammel, P. Lee, P. A. Norreys, and M. Tatarakis, "A study of picosecond laser–solid interactions up to 10^{19} Wcm^{-2}," *Physics of Plasmas*, vol. 4, no. 2, pp. 447–457, 1997.

[56] O. N. Rosmej, Z. Samsonova, S. Höfer, D. Kartashov, C. Arda, D. Khaghani, A. Schoenlein, S. Zähter, A. Hoffmann, R. Loetzsch, A. Saevert, I. Uschmann, M. E. Povarnitsyn, N. E. Andreev, L. P. Pugachev, M. C. Kaluza, and C. Spielmann, "Generation of kev hot near-solid density plasma states at high contrast laser-matter interaction," *Physics of Plasmas*, vol. 25, no. 8, p. 083103, 2018.

[57] J. Vyskocil, O. Klimo, and S. Weber, "Simulations of bremsstrahlung emission in ultra-intense laser interactions with foil targets," *Plasma Physics and Controlled Fusion*, vol. 60, p. 054013, mar 2018.

[58] K. Taguchi and J. S. Iwanczyk, "Vision 20/20: Single photon counting x-ray detectors in medical imaging," *Medical Physics*, vol. 40, Sept. 2013.

[59] E. Kleymenov, J. A. van Bokhoven, C. David, P. Glatzel, M. Janousch, R. Alonso-Mori, M. Studer, M. Willimann, A. Bergamaschi, B. Henrich, and M. Nachtegaal, "Five-element johann-type x-ray emission spectrometer with a single-photon-counting pixel detector," *Review of Scientific Instruments*, vol. 82, p. 065107, jun 2011.

[60] S. Singh, R. Versaci, A. Laso Garcia, L. Morejon, A. Ferrari, M. Molodtsova, R. Schwengner, D. Kumar, and T. Cowan, "Compact high energy x-ray spectrometer based on forward compton scattering for high intensity laser plasma experiments," *Review of Scientific Instruments*, vol. 89, no. 8, p. 085118, 2018.

[61] J. Wen, M. Yu, Y. Wu, M. Zeng, J. Cang, Y. Yang, W. Mo, and Z. Zhao, "Diagnostics for ultrashort x-ray pulses using silicon trackers," 05 2021.

[62] C. D. Chen, J. A. King, M. H. Key, K. U. Akli, F. N. Beg, H. Chen, R. R. Freeman, A. Link, A. J. Mackinnon, A. G. MacPhee, P. K. Patel, M. Porkolab, R. B. Stephens, and L. D. V. Woerkom, "A bremsstrahlung spectrometer using k-edge and differential filters with image plate dosimeters," *Review of Scientific Instruments*, vol. 79, p. 10E305, oct 2008.

[63] M. Veltri, O. Adriani, S. Albergo, M. Andreotti, R. Borgheresi, G. Cappello, P. Cardarelli, R. Ciaranfi, E. Consoli, G. Di Domenico, F. Evangelisti, M. Gambaccini, G. Graziani, M. Lenzi, F. Maletta, M. Marziani, G. Passaleva, G. Paternò, A. Serban, S. Squerzanti, O. Starodubtsev, A. Tricomi, and A. Variola, "A gamma calorimeter for the monitoring of the eli-np beam," *Nuclear Instruments and Methods in Physics Research Section A: Accelerators, Spectrometers, Detectors and Associated Equipment*, vol. 936, pp. 82–85, 2019. Frontier Detectors for Frontier Physics: 14th Pisa Meeting on Advanced Detectors.

[64] D. R. Rusby, C. D. Armstrong, C. M. Brenner, R. J. Clarke, P. McKenna, and D. Neely, “Novel scintillator-based X-ray spectrometer for use on high repetition laser plasma interaction experiments,” *Review of Scientific Instruments*, vol. 89, no. 7, p. 073502, 2018.

[65] M. Molodtsova, A. Ferrari, and T. Cowan, “Development of a novel active technique for bremsstrahlung source term determination in laser-plasma experiments,” in *SATIF 13 Proceedings*, (Helmholtz-Zentrum Dresden-Rossendorf, Bautzner Landstrasse, 400, 01328 Dresden, Germany), 2016.

[66] Eljen Technology, “GENERAL PURPOSE PLASTIC SCINTILLATOR EJ-200, EJ-204, EJ-208, EJ-212.” `https://eljentechnology.com/images/products/data_sheets/EJ-200_EJ-204_EJ-208_EJ-212.pdf`. (Accessed on 05/08/2024).

[67] G. F. Knoll, *Radiation Detection and Measurement, 4th Edition*. Wiley: Hoboken, 2010.

[68] P. Hu, Z.-G. Ma, K. Zhao, G.-Q. Zhang, D.-Q. Fang, B.-R. Wei, C.-B. Fu, and Y.-G. Ma, “Development of gated fiber detectors for laser-induced strong electromagnetic pulse environments,” *Nuclear Science and Techniques*, vol. 32, June 2021.

[69] M. Camp, H. Garbe, and D. Nitsch, “Influence of the technology on the destruction effects of semiconductors by impact of emp and uwb pulses,” in *2002 IEEE International Symposium on Electromagnetic Compatibility*, vol. 1, pp. 87–92 vol.1, 2002.

[70] V. Vlachoudis, “FLAIR: A Powerful But User Friendly Graphical Interface For FLUKA,” in *Proc. Int. Conf. on Mathematics, Computational Methods & Reactor Physics (M& C 2009)*, (Saratoga Springs, New York), 2009.

[71] “7.22.12. DEFAULTS; FLUKA Manual — flukafiles.web.cern.ch.” `https://flukafiles.web.cern.ch/manual/chapters/description_input/description_options/defaults.html`. [Accessed 25-08-2024].

[72] “7.22.88. USRBIN; FLUKA Manual — flukafiles.web.cern.ch.” `https://flukafiles.web.cern.ch/manual/chapters/description_input/description_options/usrbin.html`. [Accessed 25-08-2024].

[73] Ústav jaderné fyziky AV ČR, “Mikrotron MT-25.” `https://www.ujf.cas.cz/cs/oddeleni/oddeleni-urychlovacu/microtron/`. (Accessed on 22/06/2024).

[74] “Detail — alliedvision.com.” `https://www.alliedvision.com/en/camera-selector/detail/manta/g-235/`. [Accessed 21-03-2024].

[75] G. . www.greendot.cz (c) 2016, “Zyla - sCMOS kamery — OptiXs — optixs.cz.” `https://www.optixs.cz/vedecke-kamery-30k/scmos-kamery-62k/zyla-60p`. [Accessed 21-03-2024].

[76] "Interpolation for 2-D gridded data in meshgrid format - MATLAB interp2 — mathworks.com." `https://www.mathworks.com/help/matlab/ref/interp2.html`. [Accessed 31-03-2024].

[77] "Anonymous Functions - MATLAB & Simulink — mathworks.com." `https://www.mathworks.com/help/matlab/matlab_prog/anonymous-functions.html`. [Accessed 31-03-2024].

[78] "Vimba Viewer Configuration Guide v2.4.0 68." `https://cdn.alliedvision.com/fileadmin/content/documents/products/software/software/Vimba/docu/manuals/Vimba_Viewer_Guide.pdf`, 2020. [Accessed 31-03-2024].

[79] "Fit nonlinear regression model - MATLAB fitnlm — mathworks.com." `https://www.mathworks.com/help/stats/fitnlm.html`. [Accessed 31-03-2024].

[80] "Execute for-loop iterations in parallel on workers - MATLAB parfor — mathworks.com." `https://www.mathworks.com/help/parallel-computing/parfor.html`. [Accessed 31-03-2024].

[81] "National Radiation Protection Institute." `https://www.suro.cz/en`. (Accessed on 12/16/2020).

[82] V. Istokskaia, B. Lefebvre, R. Versaci, D. Dreghici, D. Doria, F. Grepl, V. Olšovcová, F. Schillaci, S. Stancek, M. Tryus, A. Velyhan, D. Margarone, and L. Giuffrida, "Real-time bremsstrahlung detector as a monitoring tool for laser-plasma proton acceleration (accepted for publication)," *High Power Laser Science and Engineering*, 2024.

[83] "7.22.53. OPT-PROD; FLUKA Manual — flukafiles.web.cern.ch." `https://flukafiles.web.cern.ch/manual/chapters/description_input/description_options/opt-prod.html`. [Accessed 25-08-2024].

[84] "7.22.54. OPT-PROP; FLUKA Manual — flukafiles.web.cern.ch." `https://flukafiles.web.cern.ch/manual/chapters/description_input/description_options/opt-prop.html`. [Accessed 25-08-2024].

[85] V. Istokskaia, B. Lefebvre, G. Petringa, P. Cirrone, M. Guarrera, L. Giuffrida, R. Versaci, V. Olšovcová, and D. Margarone, "Proton Bragg curve and energy reconstruction using an online scintillator stack detector," *Review of Scientific Instruments*, vol. 94, p. 073305, 07 2023.